Dissertation

submitted to the

Combined Faculty of Natural Sciences
and Mathematics

of the

Ruperto-Carola-University of Heidelberg, Germany

for the degree of

Doctor of Natural Sciences

Put forward by

Sebastian Markus Stammler
born in: Bad Friedrichshall, Germany

Oral examination: 17 May 2017

The Role of Ices in the Process of Planet Formation

Referees:

Prof. Dr. Cornelis P. Dullemond

Prof. Dr. Mario Trieloff

Abstract

When molecular clouds collapse to form stars, protoplanetary disks consisting of gas and dust are often formed as byproducts of star formation. It is assumed that planets are built from this leftover gas and dust in these disks by collisional growth of dust particles and subsequent accretion of gas. The exact mechanism, however, is not well understood.

Protoplanetary disks, in general, have temperature profiles with decreasing temperatures with increasing distances from the star. At the location, where the temperature drops below the condensation temperature of a volatile molecular species – the ice line –, the volatile freezes out as ice. This changes the chemical composition of the dust particles depending on their location in the disk. The composition of planets and planetesimals, that are formed from the dust in these disk, is therefore depending on their formation locations relative to the ice lines.

We developed a model to investigate the transport of volatile molecular species in protoplanetary disks including dust coagulation and transport, gas advection and diffusion, and evaporation and condensation of volatiles. We found that particles shortly outside of ice lines are enriched in the respective volatile species due to backward diffusion and recondensation of vapor. This recondensation has also a direct effect on the coagulation physics of the dust particles and can create ring-like, axis-symmetric dust features in protoplanetary disks.

Zusammenfassung

Wenn Molekülwolken kollabieren und Sterne bilden, entstehen oftmals protoplanetare Scheiben aus Gas und Staub als Nebenprodukt der Sternernststehung. Es wird angenommen, dass Planeten aus diesem übrig gebliebenen Gas und Staub gebildet werden, indem Staubteilchen durch Kollisionen miteinander wachsen und anschließend Gas akkretieren. Der genaue Mechanismus ist jedoch nicht gänzlich verstanden.

Protoplanetare Scheiben haben im Allgemeinen ein Temperaturprofil, bei dem die Temperatur mit zunehmendem Abstand zum Stern abnimmt. Ab dem Punkt, an welchem die Temperatur unter die Kondensationstemperatur eines flüchtigen molekularen Stoffes fällt – der Eislinie –, gefriert dieser aus zu Eis. Dies verändert die chemische Zusammensetzung der Staubteilchen abhängig davon, wo sie sich in der Scheibe befinden. Die Zusammensetzung von Planetesimalen und Planeten, die aus dem Staub gebildet werden, hängt dadurch von dem Ort ihrer Entstehung relativ zu den Eislinien ab.

Wir haben ein Modell entwickelt, welches den Transport von flüchtigen molekularen Stoffen in protoplanetaren Scheiben untersucht, einschließlich Staub Koagulation und Transport, Gas Advektion und Diffusion, sowie Verdampfung und Kondensation der flüchtigen Stoffe. Wir haben herausgefunden, dass Teilchen kurz außerhalb von Eislinien angereichert sind an dem jeweiligen Stoff, was auf rückwärts gerichtete Diffusion und anschließender Rekondensatierung zurückzuführen ist. Diese Rekondensierung hat auch einen direkten Effekt auf die Koagulationsphysik der Staubteilchen und kann zu ringartigen, achsensymmetrischen Strukturen in protoplanetaren Scheiben führen.

Resumen

Cuando las nubes moleculares colapsan durante los episodios de formación estelar los discos protoplanetarios, constituidos principalmente por gas y polvo, se forman como productos secundarios de la formación estelar. Comúnmente se asume que los planetas están formados por el gas y polvo que quedan en estos discos como consecuencia del crecimiento por colisión de las partículas de polvo y la posterior acreción del gas. Sin embargo, el mecanismo concreto por el que este proceso tiene lugar no se conoce con exactitud.

En general, los discos protoplanetarios muestran perfiles de temperatura donde ésta aumenta con la distancia a la estrella. En el punto en el que la temperatura disminuye por debajo de la temperatura de condensacin de una determinada especie molecular volátil – la línea de hielo –, la molécula se congela. Estos cambios en la composición química de las partículas de polvo dependerán, pues, de su localización en el disco. La composición de planetas y planetesimales que se forman a partir del polvo en los discos dependerá, por tanto, de la región donde se formen en relación con las líneas de hielo.

Nuestro estudio presenta un modelo para estudiar el transporte de moléculas volátiles en discos protoplanetarios, que incluye la coagulación y el transporte de las partículas de polvo, advección y difusión del gas y evaporación y condensación de las especies moleculares volátiles. En concreto, mostramos que las partículas que se encuentran justo detrás de las líneas de hielo, están enriquecidas en sus respectivas especies volátiles debido a la retro-difusión y posterior condensación del vapor. Esta condensación tiene a su vez un efecto directo sobre la coagulación de las partículas de polvo y puede llegar a crear estructuras axisimétricas de polvo, en forma de anillos, en los discos protoplanetarios.

Contents

Publications and Authorship

The work presented in this dissertation has appeared or will appear in the following publications:

Stammler, S. M., Birnstiel, T., Panić, O., Dullemond, C. P., & Dominik, C. (2017). Redistribution of CO at the location of the CO ice line in evolving gas and dust disks. Accepted for publication in A&A.

Dullemond, C. P., Harsono, D., **Stammler, S. M.**, & Johansen, A. (2016). Forming Chondrules in Impact Splashes. II. Volatile Retention. ApJ, 832:91

Stammler, S. M., & Dullemond, C. P. (2014). A critical analysis of shock models for chondrule formation. Icarus, 242:1

Dullemond, C. P., **Stammler, S. M.**, & Johansen, A. (2014). Forming Chondrules in Impact Splashes. I. Radiative Cooling Model. ApJ, 794:91

Stammler, S. M., Birnstiel, T., Panić, O., Dullemond, C. P., & Dominik, C. (2017). The influence of ice lines on dust growth in protoplanetary disks. *In preparation.*

Cuello, N., Montesinos, M., **Stammler, S. M.**, Louvet, F., & Cuadra, J. (2017). Dusty spirals triggered by shadows in transition disks. *In preparation.*

Stammler, S. M., Cuello, N., Montesinos, M., & Cuadra, J. (2017). Shadows cast by dust trapped in vortices at the outer edge of planetary gaps. *In preparation.*

Everything in this dissertation was written by me and I produced all the figures. Further details of authorship are listed here individually for each chapter:

Chapter 1: Figures 1.1 and 1.2 utilize data from the NASA Exoplanet Archive. The data shown in figure 1.3 is taken from Andrews et al. (2016) and utilizes ALMA Science Verification Data. Figure 1.9 is reproduced with data taken from Espinoza et al. (2016).

Chapter 2: The software used in this chapter was originally written by Tilman Birnstiel and has been extended by me as part of this thesis work to dynamically include the volatile species into the coagulation model. The equations of section 2.2.5 for evaporation and condensation are based upon unpublished work by

Cornelis Dullemond and Carsten Dominik. The work presented in this chapter has been published in Stammler et al. (2017).

Chapter 3: As in chapter 2. Figures 3.1, 3.12, and 3.13 show data taken from Andrews et al. (2016).

Chapter 4: The foundations of this project have been laid during my master studies. During my PhD, I extended the model to investigate ice evaporation and crystallization, performed a parameter study, and analyzed the data. The software used in this chapter was written by me. The work presented in this chapter has been published in Stammler and Dullemond (2014).

Chapter 5: Figure 5.6 shows data taken from Pérez et al. (2016). The dust software used in this chapter was written by me with inputs from Sareh Ataiee and Andras Zsom. The hydrodynamic simulations have been performed in close collaboration with Matías Montesinos.

1

Introduction

As of the beginning of 2017, more than 3 000[1] exoplanets have been officially confirmed. Exoplanets are planets, that orbit stars other than our Sun. More than 500 of those planets are in multi-planet systems. Cassan et al. (2012) estimated, that on average every star in the Milky Way hosts at least one planet. The detection of these planets, however, is very difficult. Due to the large brightness of stars compared to planets, it is often compared to finding a firefly next to a lighthouse with a binocular. It is therefore no surprise that the first exoplanet was detected indirectly.

Mayor and Queloz (1995) detected a periodic radial motion of the star 51 Pegasi by looking at spectral red- and blue shifts. They concluded that this radial motion is caused by a giant planet, that is orbiting the star, forcing it to revolve around their common center of mass. This method of detection is therefore sensitive to high mass planets in close-in orbits. Since the inclination of the planet's orbit with respect to the line of sight is not known a priori, only a lower limit of its mass can be given.

Another indirect method of detection is the continuous monitoring of light curves of stars. When a planet is passing in front of the star, it blocks some of the stellar light, which can be seen as dips in these light curves. To ensure continuous measurements, it is most convenient to observe from outer space. In 2009, the Kepler telescope started its mission to monitor the light curves of many stars simultaneously and detected more than 2 000 planets up to now. Since the lifetime of a space observatory is limited to only a few years, and since several transits per planet are needed to confirm a detection, the Kepler space craft mostly confirmed planets with small orbital periods. Transit detections are more sensitive to giant planets, since they block more light, but it is also possible detect low mass planets. Planets can only be detected, if they actually block the light of their star allowing for only a narrow window of orbital inclinations with respect to the line of sight. But due to the low inclinations, follow-up observations with the radial velocity method can help to constrain the masses of the planets, while the depth of the transit signal can be used to determine their sizes. Combining both

[1] NASA Exoplanet Archive, March 2017: http://exoplanetarchive.ipac.caltech.edu/

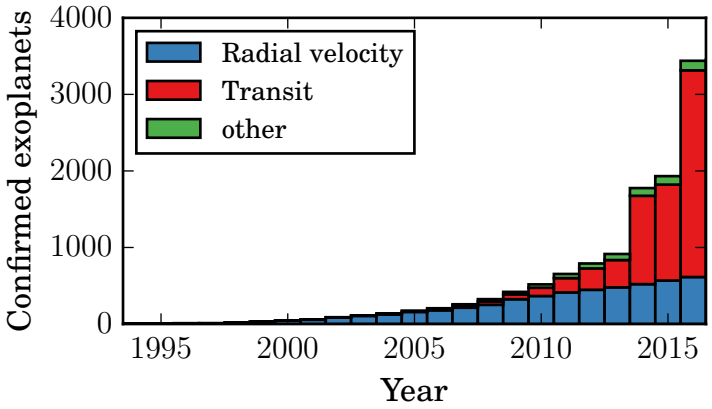

Figure 1.1: Total number of confirmed exoplanets[2] by detection method.

observations of the size and the mass yields for an average planetary mass density, which can help to classify the planets. During a transit, some of the stellar light passes the planet's atmosphere, allowing also to constrain the chemical composition of the atmosphere with spectroscopic observations.

Sometimes consecutive transits do not take place at the predicted times, but have slight variations. This hints to the presence of additional planets with inclinations that do not allow for the transit to be detectable. Analyzing the transit timing variations (TTV) can help to constrain the masses and periods of the unseen planets. Due to improved observation techniques it is now also possible to directly image planets with large separations from their host star. Another method of detection is gravitational microlensing. A star that is passing a background star can amplify its light due to gravitational lensing. A planet orbiting the lens star has also a tiny effect that can be detected. This is, of course, a very unlikely and singular event, which is why not many planets have been detected with this method so far.

Figure 1.2 shows the periods and masses of all confirmed exoplanets, where both parameters are known, color-coded with their detection method. The letters in the plot represent the eight planets of our own solar system. With the current technology and observational techniques it is very hard to detect Earth analogs orbiting other stars, since most of the detection methods are sensitive to high mass planets with small orbital periods.

The formation of planets in not yet understood well but seems to be ubiquitous in our galaxy. This chapter provides therefore an overview of current planet formation scenarios, especially planet formation by dust coagulation in protoplanetary disks.

[2]NASA Exoplanet Archive, March 2017: http://exoplanetarchive.ipac.caltech.edu/

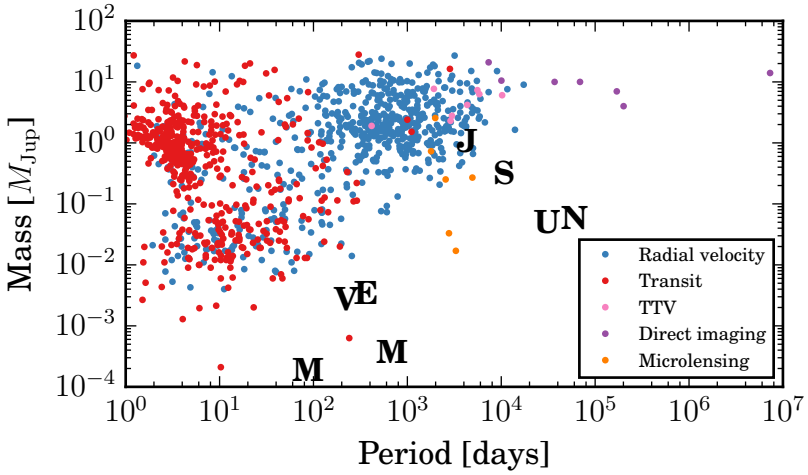

Figure 1.2: Confirmed exoplanets[3] with known masses and orbital periods sorted by the method of detection. The letters stand for the eight planets in the solar system: **M**ercury, **V**enus, **E**arth, **M**ars, **J**upiter, **S**aturn, **N**eptune, and **U**ranus.

Section 1.1 gives a brief overview of our solar system followed by a general introduction of protoplanetary disks in section 1.2. Section 1.3 explains how dust in circumstellar disks might (or might not) be transformed into planets and presents a simple toy model for dust evolution in protoplanetary disks. Finally, section 1.4 introduces the concept of ice lines and how they can affect dust growth and the distribution of volatile molecular species in protoplanetary disks.

1.1 The Solar System

Our solar system consists of eight planets: the four inner, rocky planets Mercury, Venus, Earth, and Mars, and the four gas giants Jupiter, Saturn, Uranus, and Neptune. All planets are orbiting the Sun, which is a G-type main sequence star, in the same rotational direction in more or less in the same orbital plane with only minor inclinations. The Sun contains more than 99 % of the mass of all objects in the solar system, but only 1 % of the total angular momentum.

The structure and properties of the solar system can help to understand the formation mechanism of planets. Since the planets are orbiting the sun in the same plane it is assumed that they are formed out of the dust and gas in a so-called protoplanetary disk. It is possible to estimate the minimum mass this primordial disk needed to have

[3] NASA Exoplanet Archive, March 2017: http://exoplanetarchive.ipac.caltech.edu/

to form all the solar system objects. This estimation is called minimum mass solar nebula (MMSN) and was introduced by Weidenschilling (1977b) and Hayashi (1981). It is done by taking the masses of the objects in the solar system and adding hydrogen and helium until they have the same composition as the Sun. This enhanced mass is then distributed in annuli centered on the current location of the solar system objects. The resulting surface density Σ_{MMSN} can be described by a simple power law

$$\Sigma_{\mathrm{MMSN}}(R) = 1700 \frac{\mathrm{g}}{\mathrm{cm}^2} \cdot \left(\frac{R}{1\,\mathrm{AU}}\right)^{-\frac{3}{2}}. \tag{1.1}$$

It should be noted that observations showed that many giant planets exist on orbits very close to their star. It is very unlikely that these planets were formed in situ, since the available mass close to the star is not enough to form giant planets. It is therefore assumed that these planets were formed in the outer part of their system and then migrated in the disk until they reached their final position. The planets in the solar system could also have been formed at different locations than the ones they are observed today. Tsiganis et al. (2005), for example, proposed a model where the planets formed in a different configuration and evolved over time into their current positions, the Nice model. In this case the minimum required surface density distribution was estimated by Desch (2007) as

$$\Sigma_{\mathrm{Desch}}(R) = 50\,500 \frac{\mathrm{g}}{\mathrm{cm}^2} \cdot \left(\frac{R}{1\,\mathrm{AU}}\right)^{-2.2}. \tag{1.2}$$

Kuchner (2004) did the same exercise for extrasolar systems, by looking at stellar systems with two or more planets, and derived the minimum mass extrasolar nebula (MMEN) with a surface density distribution of

$$\Sigma_{\mathrm{MMEN}}(R) = 2\,200 \frac{\mathrm{g}}{\mathrm{cm}^2} \cdot \left(\frac{R}{1\,\mathrm{AU}}\right)^{-2}. \tag{1.3}$$

These three estimations show that the primordial structure of protoplanetary disks is not well constrained and has large uncertainties. Direct observations of protoplanetary disks that could calculate their masses are also difficult and can only yield rough estimations.

It is also noticeable that there are four small rocky planets, the terrestrial planets, in the inner and four huge gas giants in the outer solar system. This hints to a change in conditions within the protoplanetary disk somewhere between Mars and Jupiter. Chiang and Goldreich (1997) estimated the temperature profile of typical protoplanetary disk to be about

$$T(R) = 150\,\mathrm{K} \cdot \left(\frac{R}{1\,\mathrm{AU}}\right)^{-\frac{1}{2}}. \tag{1.4}$$

In this case, the water ice line, the point where water can condense as ice, could have been somewhere between Mars and Jupiter. This leads to an increase in surface density by a factor of four in the outer solar system, providing more mass in the solids to form giant planets.

The asteroid belt is located between Mars and Jupiter and is considered to be the relics of failed planet formation. The asteroids have typical sizes of about 100 km, but the asteroid belt also harbors the slightly larger dwarf planet Ceres and numerous smaller objects, that are assumed to be formed in collisions between asteroids. Since the dynamical and collisional timescales are very long, the asteroid belt objects are considered to be primordial and to represent the earliest objects in the protoplanetary disk. Smaller fragments of the asteroid belt are sometimes kicked into the inner solar system by collisions or by secular interactions with Jupiter, where they can fall down on Earth as meteorites. Radiometric dating of these meteorites found ages of about 4.5 billion years (Connelly et al., 2012), which is considered to be the age of the solar system.

The oldest objects found within meteorites are calcium-aluminum-rich inclusions (CAI) and chondrules. They are considered to be the first objects that have been formed in the protoplanetary disks after the formation of the sun. Chondrules are very interesting objects, since they show some puzzling features. They are spherical droplets of silicate material, that show evidence of being once molten. The temperature, however, that is required to melt the chondrule material is about 2 000 K, which exceed the typical temperatures that are expected in the asteroid belt by a large margin. In addition to that, their spherical shape suggests that they have been molten while floating freely in space. The most prominent models of chondrules formation are therefore the creation of high temperature regions in shock waves propagating through the disk or by the collision of large objects, such as planetesimals.

Similar to the asteroid belt, there is also the Kuiper belt in the outer solar system starting at the orbit of Neptune at 30 AU up to about 50 AU, that harbors the dwarf planets Pluto, Haumea, and Makemake. Futher out is the Oort cloud that extends to distances larger than 5 000 AU. The Kuiper belt consists of two populations of objects (Tegler and Romanishin, 1998). The dynamically hot Kuiper belt consists of objects with larger eccentricities and inclinations, that are thought to be formed in the inner solar system and might have been scattered into there current locations by Jupiter. The dynamically cold populations has low inclinations and high albedos (Brucker et al., 2009). They are thought to consist of ice and to be formed in situ in the Kuiper belt.

1.2 Protoplanetary Disks

Planets are assumed to be formed from gas and dust in protoplanetary disks surrounding young stars. Protoplanetary disks themselves are byproducts of star formation. Stars are formed from collapsing giant molecular clouds, which are relatively dense

and cool regions in the galaxy compared to the interstellar medium (ISM). They are stable when the outwards gas pressure can counteract their gravity. If the giant molecular clouds exceed their critical Jeans mass, they start to collapse and fragment to form protostellar cores, from which protostars are formed subsequently. These cores have typical masses of a few solar masses. Compared to the several million solar masses of the giant molecular cloud this suggests, that star are rarely formed isolated, but in clusters.

The protostellar cores have typically an angular momentum larger than zero. Therefore, the gas and dust can not freely accrete onto the protostar. Just like a figure skater, who increases his rotational speed by putting his arms and legs closer to his axis of rotation, protostellar cores rotate with increasing velocities, when they collapse and accrete matter. At some point, this rotation counteracts the accretion and the matter accumulates in a protoplanetary disk, whose plane is perpendicular to the angular momentum.

It is very hard to directly observe these young stellar objects (YSO), since even the closest YSOs cannot be spatially resolved. It is therefore useful to classify them by their spectral index α_{IR} in the mid- to near-infrared, which is defined as the slope of the spectral energy distribution (SED) F_λ, that describes the received energy flux at a given wavelength λ

$$\alpha_{\mathrm{IR}} = \frac{\mathrm{d}\log \lambda F_\lambda}{\mathrm{d}\log \lambda}. \tag{1.5}$$

The spectral index of a star's blackbody radiation at a wavelength of $\lambda = 20\,\mu$m is typically smaller than -1.6. YSOs, on the other hand, show spectral indices that are typically larger than -1.6. This is caused by warm dust, that is absorbing the stellar light and reemitting it at longer wavelengths causing an excess over the blackbody radiation of the star in the infrared. The YSOs are grouped into four classes introduced by Lada (1987) depending on their spectral index and therefore their evolutionary state.

Class 0 objects are undetectable at wavelengths below $\lambda = 20\,\mu$m. The YSO is in the early phase of gravitational collapse. The emission originates from a central source embedded in an optically thick envelope. The light received from the YSO was therefore absorbed and re-emitted at longer wavelengths by the envelope. The peak of the SED is typically at millimeter wavelengths suggesting an envelope temperature smaller than 70 K.
Class I objects have a spectral index larger than 0.3. The infalling material cannot directly fall onto the stellar core due to conservation of angular momentum. Instead it accumulates in circumstellar accretion disks. During the collapse, gravitational energy is released that heats up the envelope to temperatures larger than 70 K making the YSO visible in the mid-infrared.
Class II objects show spectral indices between -1.6 and 0.3. Matter in the disk can be accreted by losing angular momentum. The main driver of this is viscosity, which

transports angular momentum outwards in the disk. In this phase the dust grains grow due to coagulation, which decreases the spectral index. The YSO object can now be identified as a composite of a disk and a protostar. The protostar itself, in this phase, is called a T Tauri star, named after the archetypal prototype T Tauri, if its mass is below two solar masses. More massive protostars are called Herbig Ae/Be stars.
Class III objects have spectral indices smaller than -1.6. In this phase the disk is finally dispersed. This happens after about one to ten million years after the formation of the protostar.

It is difficult to estimate the lifetime of a protoplanetary disk, since we only see snapshots of disks in different evolutionary stages of their life. Stars are usually formed in large clusters, whose ages can be inferred by looking at their color-magnitude diagrams. At the end of their lifetimes, stars leave the main sequence, with more massive stars showing a more rapid stellar evolution, where the mass of a star is directly related to its lifetime. By looking at which stars already left the main sequence and which have not, the age of the clusters can be derived. Haisch et al. (2001) and Mamajek (2009) estimated the fraction of star in clusters of different ages that still show evidence of a circumstellar disk. These disk frequencies suggest typical lifetimes of protoplanetary disks of about three million years. This sets a limit on the time in which planet formation can take place. Giant planets need to form a solid core of about ten Earth masses to be able to accrete gas. This must have happened while there is still gas in the disk. This indicates that giant planets are formed in timescales of about one million years. The formation of small rocky planets, on the other hand, can take several tens of million years, since they do not need to accrete large amounts of gas.

However, Pfalzner et al. (2014) noted that the short timescales of disk dissipation might be a selection effect. Clusters dynamically expel the majority of their outer stars (Baumgardt and Kroupa, 2007) and expand by a factor of about ten in the first ten million years (Pfalzner and Kaczmarek, 2013). Stars that are identified as cluster members after three million years are therefore stars that originate from the dense cluster core. Pfalzner and Kaczmarek (2013) showed in simulations that these stars suffered an enhanced disk dissipation due to tidal interactions in close encounters between stars. They estimate that about 30 % of field stars can still have disks after ten millions years. This significantly increases the time giant planet formation can take place.

The exact mechanisms of disk dissipation are still debated. Possible candidates are disk dissipation by tidal interactions in close encounters (Pfalzner, 2003), the formation of giant planets stirring up the gas (Rosotti et al., 2013), photoevaporation of the gas by ionizing photons emitted from the star (Alexander et al., 2006), or combinations thereof.

Mathematically, the accretion of gas in protoplanetary disks can be described by the continuity equation

$$\frac{\partial}{\partial t}\Sigma_{\mathrm{gas}} + \frac{1}{R}\frac{\partial}{\partial R}\left(R\Sigma_{\mathrm{gas}} v_{\mathrm{gas},R}\right) = 0, \tag{1.6}$$

which ensures mass conservation. R is the radial distance from the star. The right hand side of equation (1.6) is zero if we do not consider any infall of matter from the envelope onto the disk. $v_{\mathrm{gas},R}$ is the radial accretion velocity of the gas, which would be zero if the gas could not lose angular momentum. Lynden-Bell and Pringle (1974) give the accretion velocity as

$$v_{\mathrm{gas},R} = -\frac{3}{\Sigma_{\mathrm{gas}}\sqrt{R}}\frac{\partial}{\partial R}\left(\Sigma_{\mathrm{gas}}\nu\sqrt{R}\right), \tag{1.7}$$

where the angular momentum transport from the inner disk to the outside is driven by the viscosity ν. The exact source of the viscosity is still unknown, since the molecular viscosity is too low to explain the observed accretion rates. Shakura and Sunyaev (1973) therefore parametrized the viscosity to account for an unknown source that could be related to magnetic fields or to turbulence

$$\nu = \alpha c_{\mathrm{s}} H_{\mathrm{P}}, \tag{1.8}$$

where α is the viscosity parameter, typically in the order of 10^{-4} to 10^{-2}, and H_{P} the pressure scale height of the disk. The sound speed c_{s} is given by

$$c_{\mathrm{s}} = \sqrt{\frac{k_{\mathrm{B}}T}{\mu m_{\mathrm{p}}}}, \tag{1.9}$$

with the Boltzmann constant k_{B}, the midplane disk temperature T, and the proton mass m_{p}. The molecular weight of the gas is about $\mu = 2.3$, assuming that it consists of 75 % molecular hydrogen and 25 % helium.

The vertical structure can be explained by assuming vertical hydrostatic equilibrium and equating the vertical gravitational acceleration to the counteracting pressure force. The calculation of the vertical gravitational force can be simplified by only taking into account the contribution of the star and neglecting the self-gravity of the disk, since typical disks have only masses of a few percent of the stellar mass. In cylindrical coordinates with a radial coordinate R and the a vertical coordinate z, the gravitational potential of the star is given by

$$\Phi\left(R,z\right) = \frac{GM_{\star}}{\sqrt{z^2+R^2}}\ , \tag{1.10}$$

with the gravitational constant G and the stellar mass $M_{\star}$. The gravitational acceleration in vertical direction is then given by the z-derivative of the gravitational potential

$$\frac{\partial\Phi}{\partial z} = -\frac{GM_{\star}}{\left(z^2+R^2\right)^{\frac{3}{2}}}z \simeq -\frac{GM_{\star}}{R^3}z = -\Omega_{\mathrm{K}}^2 z, \tag{1.11}$$

where we assumed that disk are usually thin with $z \ll R$. Ω_K is the Keplerian frequency. The pressure acceleration that counteracts gravity is given by

$$-\frac{1}{\rho_{gas}}\frac{\partial P}{\partial z} = -\frac{c_s^2}{\rho_{gas}}\frac{\partial \rho_{gas}}{\partial z}, \tag{1.12}$$

where the pressure is given by $P = \rho_{gas} c_s^2$ and we assumed that the temperature and therefore the sound speed is independent of z. Equating equation (1.11) with equation (1.12) yields

$$\frac{\partial \rho_{gas}}{\rho_{gas}} = \left(\frac{\Omega_K}{c_s}\right)^2 z \partial z \ . \tag{1.13}$$

The vertical density profile can therefore be expressed by a Gaussian with

$$\rho_{gas}(z) = \rho_{gas}(z=0) \cdot \exp\left[\frac{z^2}{2H_P^2}\right] \ , \tag{1.14}$$

where the pressure scale height is given by

$$H_P = \frac{c_s}{\Omega_K}. \tag{1.15}$$

By demanding that the vertical integral of the mass density ρ_{gas} has to be equal to the surface density Σ_{gas}, the midplane gas density is given by

$$\rho_{gas}(R, z=0) = \frac{\Sigma_{gas}(R)}{\sqrt{2\pi} H_P} \ . \tag{1.16}$$

Interestingly, the gas does not orbit the star with the Keplerian velocity. Since disks are typically more dense closer to the star, the outwards pressure gradient does stabilize the gas against gravity. The velocity necessary for stable orbits is therefore smaller than the Keplerian velocity. The azimuthal velocity is given by

$$v_{gas,\varphi}^2 = \frac{GM_\star}{R} + \frac{R}{\rho_{gas}}\frac{dP}{dR} = (1-2\eta)\, v_K^2 \ , \tag{1.17}$$

where the degree of sub-Keplerianity 2η is given by

$$2\eta = -\frac{R}{v_K^2 \rho_{gas}}\frac{dP}{dR}. \tag{1.18}$$

The pressure gradient is typically negative, having decreasing gas pressure with increasing distance from the star. The factor 2 in the definition of the sub-Keplerianity will become clear in the next section.

1.3 Dust Evolution

To understand planet formation it is important to understand the dynamics of dust particles in protoplanetary disks. The dust particles interact aerodynamically with the gas, which is important for two reasons.

The gas is orbiting the star with sub-Keplerian velocities due to the pressure gradient as shown in the previous section. Without gas, the particles would orbit with Keplerian velocities, since they do not have any internal pressure force. Therefore, the particles feel a constant headwind from the slower gas, lose angular momentum, and drift towards the star. This removes the dust very quickly from protoplanetary disks reducing the ability to form planets.

And second, it is assumed that planets are formed from colliding dust particles that form ever larger dust aggregates. The collisions are driven by relative velocities between the dust particles. Furthermore, the collision velocity determines the outcome of a collision. If it exceeds the fragmentation velocities, the particles rather fragment instead of growing further. The relative collision velocities depend on interactions with the turbulent gas. It is therefore important to understand the aerodynamics of dust particles in protoplanetary disks.

This section explains how dust particles interact with gas in general and how this behavior affects their movement in protoplanetary disks. Furthermore, we introduce the coagulation method and introduce the collisional physics that determine the outcome of dust collisions. To get a better understanding of dust evolution, we introduce a toy model, that explains in a simplified way, how dust particles grow and evolve in protoplanetary disks.

1.3.1 Dust Transport

Dust particles in protoplanetary disks are subject to gravity and orbit the star on Keplerian orbits, if they have a non-zero angular momentum. In addition to that they are affected by gas drag. To describe the interaction of dust particles with the gas it is convenient to introduce the stopping time t_{stop}, which is the typical timescale it takes for a dust particle to adapt to changes in the gas flow. It is defined as the ratio of momentum to momentum change

$$t_{\text{stop}} = \frac{m\,|\vec{v}|}{\left|\vec{F}_{\text{drag}}\right|}, \tag{1.19}$$

where m and v are the particle's mass and velocity, and F_{drag} the drag force acting on a spherical particle by the gas, which is given by

$$F_{\text{drag}} = \frac{1}{2} C_{\text{drag}} \pi a^2 \rho_{\text{gas}} \Delta v^2 \tag{1.20}$$

with the particle radius a, the gas density ρ_{gas}, and the relative velocity Δv between gas and dust. The factor C_{drag} is the drag coefficient, that depends on the kind of interaction of the gas with the dust. If the particle size is smaller than $9/4$ of the mean free path λ_{mfp} of the gas molecules, the resulting drag can be considered as individual collisions of gas molecules with the dust particle. The mean free path is given by

$$\lambda_{\text{mfp}} = \frac{1}{n\sigma_{\text{H}_2}} = \frac{\mu m_{\text{p}}}{\rho_{\text{gas}}\sigma_{\text{H}_2}}, \tag{1.21}$$

with $\mu = 2.3$ being the molecular weight of the gas in units of proton masses m_{p} and $\sigma_{\text{H}_2} = 2 \cdot 10^{-15}\,\text{cm}^2$ the cross section of molecular hydrogen. In this so-called Epstein drag the drag coefficient is given by Whipple (1972) as

$$C_{\text{drag}} = \frac{8}{3}\frac{v_{\text{th}}}{\Delta v} \tag{1.22}$$

with $v_{\text{th}} = \sqrt{8/\pi}\; c_{\text{s}}$ being the thermal velocity of the gas molecules. If the particles are larger, the gas has to be treated as fluid. In this so-called Stokes regime, the drag force depends on the Reynolds number Re of the gas, which is the ratio of inertial to viscous forces

$$\text{Re} = \frac{2a\Delta v}{\nu}, \tag{1.23}$$

with the kinematic viscosity $\nu = \frac{1}{2}v_{\text{th}}\lambda_{\text{mfp}}$ of the gas. The drag coefficient is here given by Whipple (1972) and Weidenschilling (1977a) as

$$C_{\text{drag}} = \begin{cases} 24\,\text{Re}^{-1} & \text{if } \text{Re} < 1 \\ 24\,\text{Re}^{-0.6} & \text{if } 1 < \text{Re} < 800 \\ 0.44 & \text{if } \text{Re} > 800. \end{cases} \tag{1.24}$$

This can now be plugged in into equation (1.19) to calculate the stopping time as

$$t_{\text{stop}} = \begin{cases} \frac{a\xi}{v_{\text{th}}\rho_{\text{gas}}} & \text{if } a < \frac{9}{4}\lambda_{\text{mfp}} \\ \frac{2}{9}\frac{a^2\xi}{\nu\rho_{\text{gas}}} & \text{if } \text{Re} < 1 \\ \frac{2^{0.6}}{9}\frac{a^{1.6}\xi}{\nu^{0.6}\rho_{\text{gas}}\Delta v^{0.4}} & \text{if } 1 < \text{Re} < 800 \\ \frac{6a\xi}{\rho_{\text{gas}}\Delta v} & \text{if } \text{Re} > 800. \end{cases} \tag{1.25}$$

The first case is the Epstein regime, the other three cases are the Stokes I, II, and III regimes. ξ is the bulk density of the dust particles and $m = 4/3\pi\xi a^3$ was used for the

particle mass. For typical particle sizes and conditions in protoplanetary disks only the Epstein and the Stokes I regime are relevant.

It turned out to be useful for aerodynamic calculations to define the dimensionless Stokes number, which is the ratio of the stopping time to the turnover time of the largest eddies

$$\mathrm{St} = \frac{t_{\mathrm{stop}}}{\tau_{\mathrm{ed}}} = t_{\mathrm{stop}}\Omega_{\mathrm{K}} \ , \tag{1.26}$$

where Schräpler and Henning (2004) estimated the turnover time to be $\tau_{\mathrm{ed}} \simeq 1/\Omega_{\mathrm{K}}$. The Stokes number in the Epstein and Stokes I regimes is then given by

$$\mathrm{St} = \begin{cases} \frac{\pi}{2}\frac{a\xi}{\Sigma_{\mathrm{gas}}} & \text{if } \ a < \frac{9}{4}\lambda_{\mathrm{mfp}} \\ \\ \frac{2\pi}{9}\frac{a^2\xi}{\lambda_{\mathrm{mfp}}\Sigma_{\mathrm{gas}}} & \text{if } \ a > \frac{9}{4}\lambda_{\mathrm{mfp}}. \end{cases} \tag{1.27}$$

We have seen previously that the gas gets accreted with the radial velocity $v_{\mathrm{gas},R}$. Dust particles on Keplerian orbits will therefore be dragged inwards together with the gas depending on their sizes. In addition to that, the pressure gradient of the gas introduces another source of relative velocity between the gas and dust. In contrast to the dust particles, the gas feels its own pressure. Since typical disks are more dense in the inner parts, the pressure gradient is pointing inwards. Therefore, the gas is experiencing an outwards directing pressure force that supports the gas against gravity. Thus, the gas orbits the star with velocities smaller than the Keplerian velocity as shown in equation (1.17).

The dust particles, on the other hand, are not pressure supported and are on Keplerian orbits. Therefore, they feel a constant headwind by the gas, which causes the particles to lose angular momentum, and drift towards the star. The gas pressure is given by

$$P = \rho_{\mathrm{gas}} c_{\mathrm{s}}^2 = \frac{\Sigma_{\mathrm{gas}}}{\sqrt{2\pi}H_{\mathrm{P}}} c_{\mathrm{s}}^2 = \frac{\Sigma_{\mathrm{gas}}}{\sqrt{2\pi}} c_{\mathrm{s}}\Omega_{\mathrm{K}}. \tag{1.28}$$

If we parametrize the disk's surface density as $\Sigma_{\mathrm{gas}} \propto R^{-p}$ and the midplane temperature as $T \propto R^{-q}$, then the pressure is proportional to $P \propto R^{-k}$, with $k = p + q/2 + 3/2$. The pressure gradient is now given by

$$\frac{1}{\rho_{\mathrm{gas}}}\frac{\mathrm{d}P}{\mathrm{d}R} = -k\frac{c_{\mathrm{s}}^2}{R}. \tag{1.29}$$

The factor η in equation (1.18) is then given by

$$2\eta = k\frac{c_{\mathrm{s}}^2}{v_{\mathrm{K}}^2}. \tag{1.30}$$

In a typical MMSN disk with $p = 3/2$ and $q = 1/2$ and an aspect ratio of $c_s/v_K = 0.03$, we have $k = 13/4$ and a factor of sub-Keplerianity of $2\eta \sim 3 \cdot 10^{-3}$. The azimuthal gas velocity is with $v_{gas,\varphi} = 0.997\, v_K$ therefore only slightly smaller than the Keplerian velocity. But this headwind is enough that particles, that are not fully coupled to the gas, lose angular momentum and drift towards the star. Adachi et al. (1976) and Weidenschilling (1977a) give the equation of motion of the dust particles as

$$v_{dust,R} = \frac{v_{gas,R}}{1 + St^2} + \frac{2\eta v_K}{St + St^{-1}}. \tag{1.31}$$

This formula consists of two terms. The first term is called drag. It accounts for the dust particles that are dragged radially along with the accreting gas. It is therefore most effective for small particles that are fully coupled to the gas. Large particles with large Stokes numbers are decoupled from the gas and are not affected by the drag. The second term in equation (1.31) is called drift. It accounts for dust particles that drift in directions of pressure gradients due to the headwind of the gas. It is most effective for intermediate sized particles with Stokes numbers of unity. For particles with $St = 1$ the maximum drift velocity is $v_P = \eta v_K$. This explains why the sub-Keplerianity 2η is defined with a factor of two. Small particles with small Stokes numbers are not affected by particle drift. They are fully coupled to the gas and therefore do not experience any headwind. Large particles with large Stokes numbers, such as planets and planetesimals, are also not affected by drift, since they are fully decoupled from the gas.

As seen in equation (1.31), the dust particles are accreted faster than the gas, if the pressure gradient is negative. This is the reason why the dust is usually more compact compared to the gas in protoplanetary disks. This can be seen for example in figure 1.3, that compares the dust emission in red of the disk around TW Hydrae to the CO gas emission in blue. The dust disk is significantly more compact than the gas disk, which is due to dust particles drifting inwards towards the pressure maximum.

1.3.2 Dust Coagulation

Dust particles in protoplanetary disks are growing by collisions and subsequent sticking with other dust particles. It is a non-trivial task to simulate the growth of micrometer sized particles up to planetesimals. A typical protoplanetary disk has dust masses equivalent to about 10^{45} micrometer sized dust particles. It is therefore not feasible to simulate the evolution of every individual particle. One approach of solving this problem is to combine several thousands of physical particles into a swarm of particles with identical properties and then solve the evolution of these fewer representative particles. This method was developed amongst others by Ormel et al. (2007), Zsom and Dullemond (2008), and Drążkowska et al. (2013).

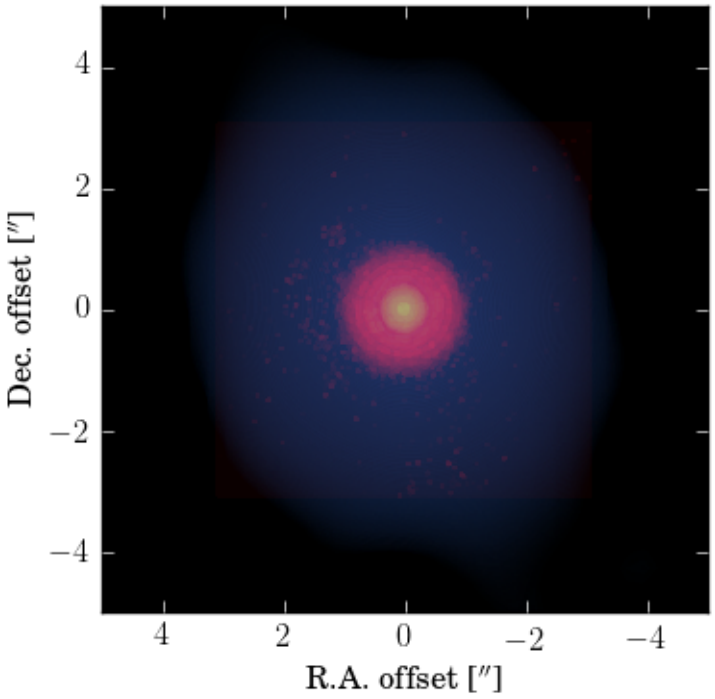

Figure 1.3: Superposition of dust emission at $\lambda = 870\,\mu$m (red) (Andrews et al., 2016) and the CO(3-2) gas line[4] (blue) in the disk around TW Hydrae.

Another possibility of simulating the dust evolution in protoplanetary disks is to look at particle distributions instead of individual particles. The collisional evolution of a particle mass distribution $n(m)$ was described by Smoluchowski (1916)

$$\frac{\partial}{\partial t} n(m) = \int_0^\infty \int_0^\infty n(m')\, n(m')\, M(m, m', m'')\, \mathrm{d}m' \mathrm{d}m''. \tag{1.32}$$

The so-called Smoluchowski equation counts all collisions between particles m' and m''. The collisional physics and the results of individual collisions are hidden in the collision Kernel $M(m, m', m'')$, that is defined in the case of coagulation and fragmentation as

$$\begin{aligned} M(m, m', m'') = &\frac{1}{2} K(m', m'')\, \delta(m' + m'' - m) \\ &- K(m', m'')\, \delta(m'' - m) \\ &+ \frac{1}{2} L(m', m'')\, S(m, m', m'') \\ &- L(m', m'')\, \delta(m'' - m). \end{aligned} \tag{1.33}$$

[4] Science verification data ADS/JAO.ALMA#2011.0.00001.SV.

The collisional Kernel consists of four terms. The first two terms accounts for hit-and-stick collisions. The first term adds particles into mass bin m that resulted from a collision of two particles of masses m' and m''. The negative term removes the colliding particles from the distribution. The factor of $1/2$ accounts for the fact that two colliding particles only create one particle. The third and fourth terms in equation 1.33 represent fragmentation, where the collision of two particles of masses m' and m'' produce a distribution of fragments $S\left(m, m', m''\right)$. The coagulation and fragmentation kernels $K\left(m', m''\right)$ and $L\left(m', m''\right)$ give the rate of individual hit-and-stick or fragmenting collisions and are defined as

$$K\left(m', m''\right) = \sigma_{\text{geo}}\, \Delta v\, p_{\text{c}} \tag{1.34}$$

$$L\left(m', m''\right) = \sigma_{\text{geo}}\, \Delta v\, p_{\text{f}}. \tag{1.35}$$

$\sigma_{\text{geo}} = \pi\left(a' + a''\right)^2$ is the geometrical cross section, Δv the relative velocity of the colliding dust particles, and p_{c} and p_{f} the coagulation and fragmentation probabilities. In a hit-and- stick collision we have $p_{\text{c}} = 1$ and $p_{\text{f}} = 0$, while it is the opposite in a fragmenting collision. If particles bounce off each other with neither sticking nor fragmentation, we have $p_{\text{c}} = p_{\text{f}} = 0$. In this case, the particle mass distribution does not change.

1.3.3 Relative Collision Velocities

The outcome of individual particle collisions highly depend on the collision velocity. In hit-and-stick collisions the colliding particles are held together after collisions just by the week van der Waals force, which is a short-range contact force that arises from induced electrical dipoles in the adjacent surfaces of the particles. Since the van der Waals force is very week, this only works for small velocity collisions. Dust aggregates consist of many small building blocks, the monomers. These monomers can roll on each other. The energy E_{roll} required to roll two monomers over each other on the contact surface and the energy E_{break} required to break the connection between two monomers is proportional to the material's surface energy γ and the monomer size a_0 within an aggregate as given by Dominik and Tielens (1997)

$$E_{\text{roll}} \propto \quad a_0 \quad \gamma \tag{1.36}$$

$$E_{\text{break}} \propto \quad a_0^{4/3} \gamma^{5/3}. \tag{1.37}$$

Typical values for the monomer sizes are $(0.1 - 1.0)\ \mu$m. The surface energy is a material constant and has to be determined experimentally. For silicates it is in the order of about $20\,\text{erg}/\text{cm}^2$ (Heim et al., 1999). If the impact energy is smaller than about five times the rolling energy, then no restructuring takes place in a collision (Güttler et al., 2010). If the impact energy becomes larger than that, then restructuring, such as rolling, twisting, sliding, and breaking of monomer connections happen within a dust aggregate (Dominik and Tielens, 1997).

In principle, dust coagulation is a problem of energy dissipation. Since the van der Waals force is very weak, the impact energy has to be dissipated by restructuring the dust aggregates for the particles to be able to stick to each other. Fractal aggregates have therefore a higher ability to dissipate energy by restructuring due to higher degrees of freedom. However, in collisions these fractal aggregates are getting compressed. If the aggregate is compact enough, such that the impact energy cannot be dissipated any further, but the impact energy is yet too small for breaking the bonds between the monomers, bouncing can occur, where the particles rebound off each other with very little mass transfer. Kothe et al. (2013) experimentally found that for silicate particles the transition between sticking and bouncing happens at collision velocities between $(1 - 10)$ cm/s.

At even higher collision velocities, the particles start to fragment. The collision velocity at which this occurs has been experimentally determined for millimeter sized particles to be in the order of 1 m/s (Blum and Münch, 1993) and for centimeter sized particles to be about 40 cm/s (Schräpler et al., 2012).

It is therefore crucial to know the typical relative velocities that occur in collisions of certain particle sizes in protoplanetary disks. There are basically five different sources of relative velocities: Brownian motion, radial and azimuthal drift, vertical settling, and turbulence.

Brownian Motion

Brownian motion describes the random walk the particles experience due to collisions with gas molecules. The relative velocity between two dust particles of mass m_1 and m_2 is here given by

$$\Delta v_{\mathrm{bm}} = \sqrt{\frac{8 k_{\mathrm{B}} T \left(m_1 + m_2\right)}{\pi m_1 m_2}}. \tag{1.38}$$

It is most effective for tiny particle masses and an important driver for the early growth of small dust particles.

Radial Drift

As seen in equation (1.31), particles are drifting radially in protoplanetary disks. The drift velocity is size dependent. Thus, particles of different sizes experience relative velocities to each other, that are given by

$$\Delta v_{\mathrm{rd}} = \left| v_{\mathrm{dust},R}\left(m_1\right) - v_{\mathrm{dust},R}\left(m_2\right) \right|. \tag{1.39}$$

Azimuthal Drift

Dust particles are affected by azimuthal gas drag due to the headwind of the gas. This changes the orbital velocity due to this gas drag depending on the particle size. Similar to the radial drift velocity, the relative velocity caused by azimuthal drift is given by

$$\Delta v_{\mathrm{ad}} = \left| v_{\mathrm{dust},\varphi}\left(m_1\right) - v_{\mathrm{dust},\varphi}\left(m_2\right) \right| , \tag{1.40}$$

with the azimuthal particle velocity

$$v_{\mathrm{dust},\varphi} = \left(1 - \frac{\eta}{1+\mathrm{St}^2}\right) v_{\mathrm{K}} \ . \tag{1.41}$$

Vertical Settling

Particles in disks settle vertically towards the midplane. The settling velocity depends on the particle size and the vertical height in the disk. But since we are not resolving the vertical dimension of the protoplanetary disks in this work, we use the approach of Dullemond and Dominik (2004) and Birnstiel et al. (2010) be taking the relative velocity of of particles at one scale height

$$\Delta v_{\mathrm{vs}} = \left| h_1 \min\left(\mathrm{St}_1, \frac{1}{2}\right) - h_2 \min\left(\mathrm{St}_2, \frac{1}{2}\right) \right| \Omega_{\mathrm{K}} \ , \tag{1.42}$$

with the dust scale height given by Birnstiel et al. (2010) as

$$h = H \cdot \min\left(1, \sqrt{\frac{\alpha}{\min\left(\mathrm{St}, 1/2\right)\left(1+\mathrm{St}^2\right)}}\right) . \tag{1.43}$$

Turbulence

The turbulent gas disk induces relative velocities Δv_{turb} between dust particles. The description of turbulence is very complex. We use is this work the closed form expressions for the relative velocities derived by Ormel and Cuzzi (2007).

Combined Relative Velocity

The combined relative velocity is then given by the root mean square of all individual sources

$$\Delta v = \sqrt{\Delta v_{\mathrm{bm}}^2 + \Delta v_{\mathrm{rd}}^2 + \Delta v_{\mathrm{ad}}^2 + \Delta v_{\mathrm{vs}}^2 + \Delta v_{\mathrm{turb}}^2}. \tag{1.44}$$

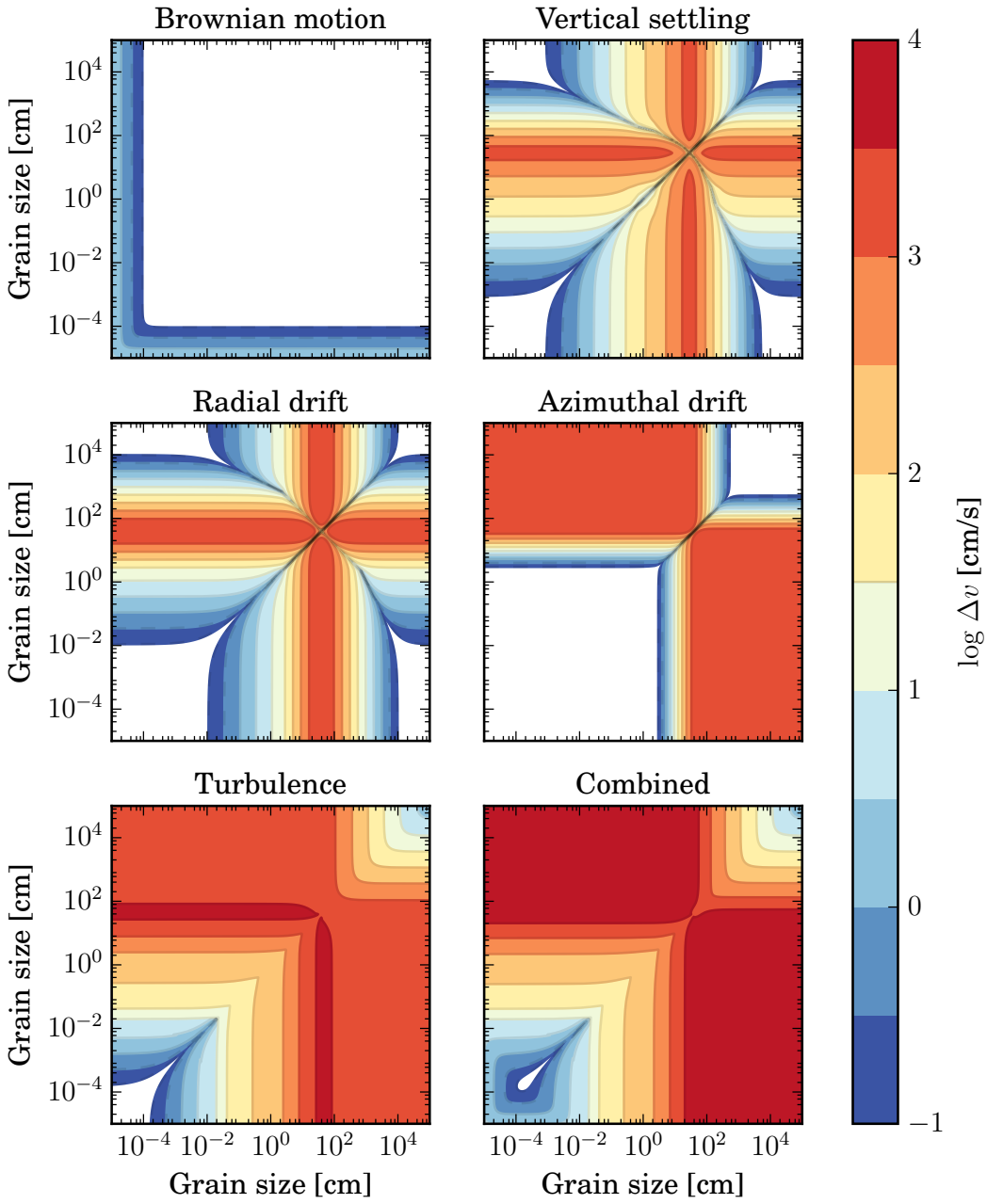

Figure 1.4: The five sources of relative velocity: Brownian motion, vertical settling, radial and azimuthal drift, and turbulence at 1 AU in the MMSN. The plot on the bottom right shows the root mean square of all relative velocities.

Figure 1.4 shows the five sources of relative velocity and the resulting root mean square

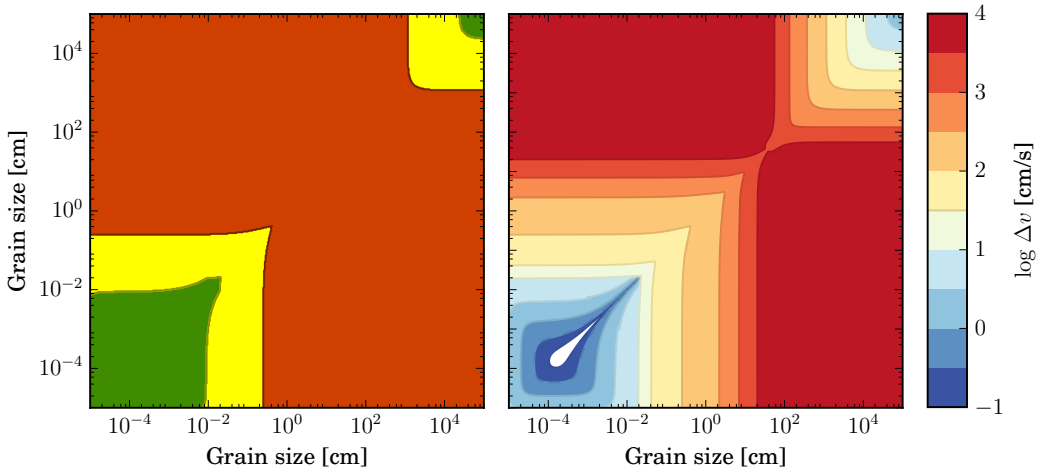

Figure 1.5: Outcomes of particle collisions at 1 AU in the MMSN in a simple collision model with a bouncing velocity of $v_{\text{bounce}} = 5\,\text{cm/s}$ and a fragmentation velocity of $v_{\text{frag}} = 1\,\text{m/s}$: Sticking (green), bouncing (yellow), and fragmentation (red).

velocity at 1 AU in a typical MMSN. It can be seen that the driver of small particle collisions is Brownian motion, while turbulence is important for equal size collisions, since the aerodynamically induced relative velocities are zero for equal sized particles. If we now assume a typical bouncing velocity of 5 cm/s and a fragmentation velocity of 1 m/s, we can color code the velocities with the expected collision outcome. This is done in figure 1.5, where the green area represents hit-and-stick collisions, the yellow area bouncing collisions, and the red area fragmenting collisions. It is therefore very difficult for micrometer sized particles in this specific case at 1 AU to grow beyond 1 mm to 1 cm. This is called bouncing barrier or fragmentation barrier, depending on which process hinders the growth.

1.3.4 A Simple Toy Model

To get a better understanding of dust evolution in protoplanetary disks without solving the full Smoluchowski equation (1.33) a simple toy model can be utilized. If we assume monodisperse growth, particles are only colliding with particles of the same size. Therefore, in every collision the particle mass doubles

$$\frac{\mathrm{d}m}{\mathrm{d}t} = \frac{m}{\tau_{\text{coll}}}, \tag{1.45}$$

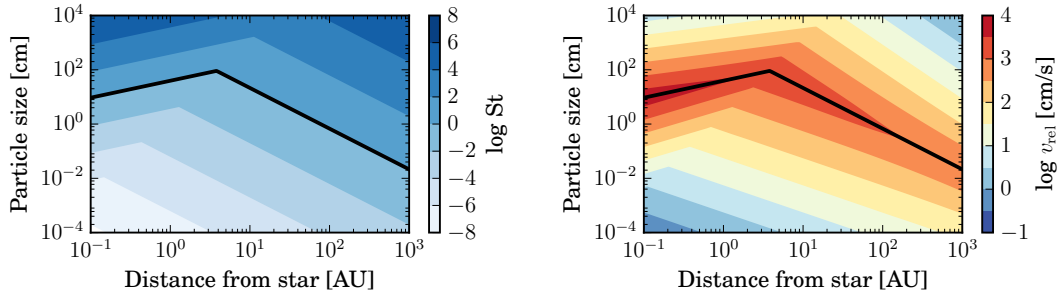

Figure 1.6: The typical Stokes numbers and collision velocities in a typical MMSN in the toy model. The bold black lines represent particles of Stokes number unity. The change in slope is due to the transition from the Epstein drag regime in the outer disk to the Stokes I regime in the inner disk.

where $\tau_{\rm coll} = 1/\left(\rho_{\rm dust}\sigma_{\rm geo}\Delta v\right)$ is the time between two collisions. Using $\mathrm{d}m = 4\pi\xi a^2\mathrm{d}a$ this can be transformed to a differential equation for the particle size

$$\frac{\mathrm{d}a}{\mathrm{d}t} = \frac{\rho_{\rm dust}}{\xi}\Delta v. \tag{1.46}$$

Since the relative velocity of equal size particles is reduced due to the lack of the aerodynamical components, we assume for the collisions velocities, that the particles collide with particles of half their size.

The Stokes numbers and the collisional velocities for at each radial distance for every particle size in a typical MMSN are shown in figure 1.6. The bold black lines represent particles with Stokes number unity, the fastest drifting particles. The change in the slope is due to the transition from the Epstein drag regime in the outer disk to the Stokes I regime in the inner disk. It can be seen that particles of the same size have higher Stokes numbers, the farther out in the disk they are. Meaning, particles of the same size drift faster in the outer disk. The radial evolution of the dust is solved by integrating

$$\frac{\mathrm{d}R}{\mathrm{d}t} = v_{\mathrm{dust},R}\ , \tag{1.47}$$

where $v_{\mathrm{dust},R}$ is the radial dust velocity given by equation (1.31).

We start with particles of 1 μm at different locations in the disk and solve equations (1.46) and (1.47) simultaneously, as long as the collision velocity is smaller than the fragmentation velocity for silicates. This is shown in figure 1.7. In the blue area the drift timescale $R/\Delta R$ is shorter that the growth timescale $a/\Delta a$. Particles in the outer disk grow until they approach the blue area where they start to drift inwards rapidly. This is called drift barrier. In the inner disk, the densities are high enough, such that the growth timescales are always shorter than the drift timescales. Here, the particles

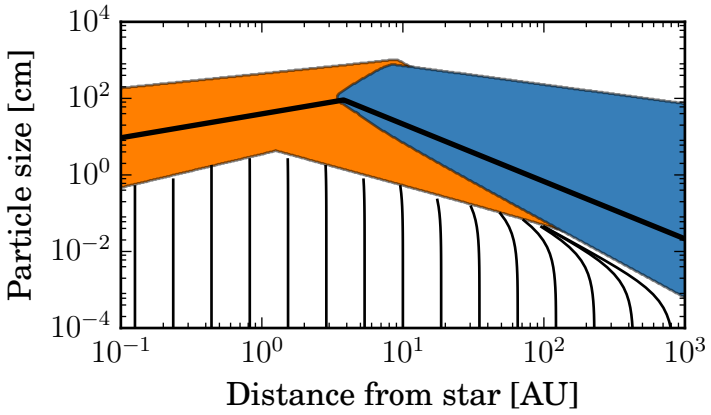

Figure 1.7: Evolutionary tracks of particles in a toy model (black lines). The blue area is the drift barrier, where the drift timescale is shorter than the growth time scale. The orange area is the fragmentation barrier, where the relative velocity of particles in a collision is larger than the fragmentation velocity. The bold black line represents particle sizes with St=1. In the outer disk particle growth is drift limited, while in the inner disk it is fragmentation limited.

grow until they reach the fragmentation barrier, where we terminate the toy model. The maximum particle size is about 1 cm at 1 AU and the maximum Stokes numbers are between 10^{-2} and 10^{-1}.

The structure of the fragmentation and the drift barrier is quite universal to several different disk profiles. In general, particle growth is hindered by radial drift in the outer disk, and by fragmentation in the inner disk. This has an influence on the particle size distributions at different locations in the disk. When particle growth is drift limited, the particle size distribution is quite narrow with sizes close to the drift barrier. But when growth is limited by fragmentation, small particles get replenished due to fragmentation. Here, the particle size distribution is very broad, with particles from monomer sizes up to the fragmentation barrier.

1.3.5 Alternative Models of Planet Formation

The presented toy model is of course only an approximation. But calculations solving the full Smoluchowski equation (Birnstiel et al., 2010) or by using the representative particles approach (Zsom and Dullemond, 2008, Drążkowska et al., 2013) show in general the same behavior. The growth of dust particles in the outer disk is drift limited, while it is fragmentation limited in the inner disk. So far, several mechanisms were proposed to overcome these barrier and to form planetesimals and planets

The collision model with sticking, bouncing, and fragmentation as seen in figure 1.5 is very simple. More sophisticated experiments performed by Güttler et al. (2010) identified additional collision outcomes, such as erosion and mass transfer for collisions of unequal size particles, where a small projectile hits a large target. Both, collisions with erosion and with mass transfer, are collisions where the projectile fragments completely. Erosion means that the projectile, in addition, chips off mass of the large target. In fragmenting collisions with mass transfer a fraction of the mass of the projectile keeps sticking to the target. The difference between the two collision outcomes is, that in erosion the target particle loses mass, while it gains mass in collisions with mass transfer. Windmark et al. (2012a) showed, that large particles could grow to planetesimals in mass transfer collisions by sweeping up small particles. However, the creation of these large particles is still hindered by the bouncing barrier.

Equation (1.44) assumes that the relative collision velocities are distinct for every combination of particle sizes. In reality, however, the particles will collide with a distribution of relative velocities. Windmark et al. (2012b) implemented a velocity distribution in their model. In that way, a few lucky particles only experienced collisions in the low velocity tail of the distribution and could break through the bouncing barrier. These few lucky particles can then sweep up the small particles that are still trapped below the bouncing barrier in mass transfer collisions and can grow to planetesimals.

Dust particles are trapped in pressure maxima, since they are drifting in the direction of pressure gradients as seen in equation (1.31). Several mechanisms have been proposed for creating such pressure bumps in the gas density, such as ice lines (Kretke and Lin, 2007) or due to an accumulation of material at the outer edge of magnetically inactive zones, the so-called dead zones (Pinilla et al., 2016). Simulations of pressure bumps showed that they can indeed trap particles (Pinilla et al., 2012) and can form planetesimals by creating large particles that can eventually sweep up smaller particles (Drążkowska et al., 2013).

Another prominent idea is that the so-called streaming instability can concentrate particles until the mass of the concentration is large enough for gravity to collapse the particles into planetesimals (Youdin and Goodman, 2005, Johansen et al., 2007). The gas does not only have a reaction on the dust dynamics, but vice versa, the dust has also a back reaction on the gas. With typical dust-to-gas ratios of 0.01, this back reaction can usually be neglected. However, due to statistical fluctuations particles can be concentrated by chance. These particles then act together as if they were a larger particle and can shield themselves from the headwind. This decreases or even stalls their radial drift, leading to the accumulation of more particles that drift from the outer disk into this region. At some point, when the particle concentration is massive enough, gravity can take over and can collapse the dust accumulation into planetesimals with typical sizes of a few hundreds of kilometers. Simulations including back reactions from the dust onto the gas are computationally very expensive. Therefore, it is unclear, what particle size distributions are necessary to trigger the streaming instability. Simulations by Bai and Stone (2010) suggest that particles with Stokes numbers of at

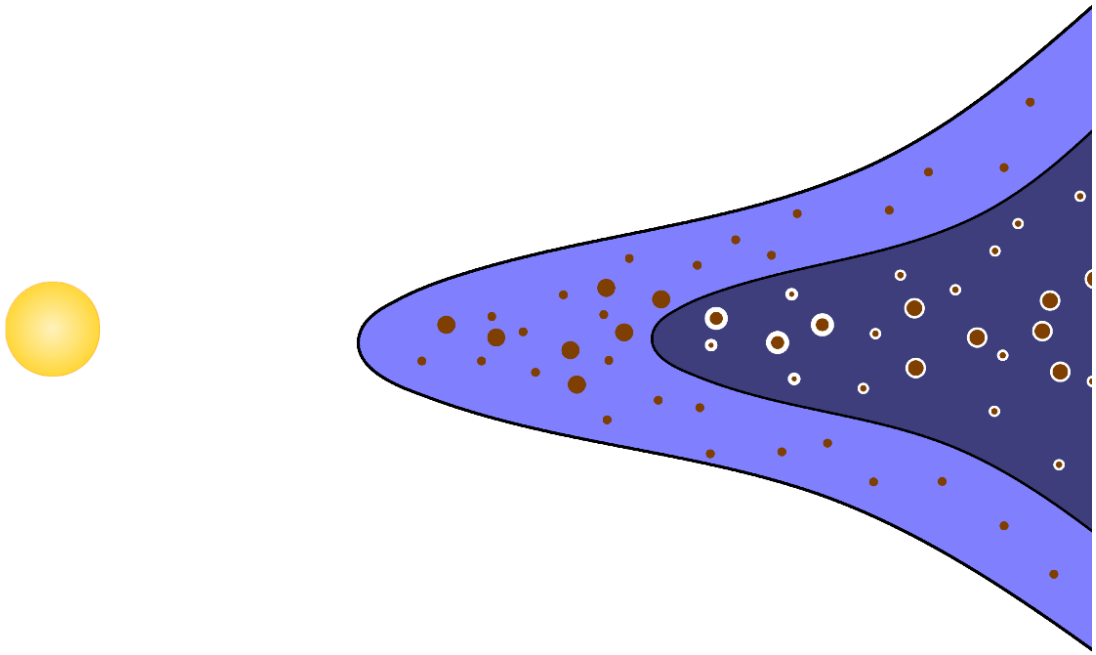

Figure 1.8: Sketch of an ice line in a protoplanetary disk. Inside the ice line (light blue), the temperature is high enough for the volatile ice to evaporate. Only bare dust grains exist. Outside the ice line (dark blue), the volatile gas freezes out on the dust particles as ice. The ice mantles of the particles are typically larger close to the ice line due to evaporation of drifting particles and subsequent recondensation of vapor outside of the ice line.

least 0.01 to 1 are needed, which is already quite large for typical protoplanetary disks. Furthermore, the streaming instability requires local dust-to-gas that are significantly enhanced above the typical value of 0.01. Drążkowska and Dullemond (2014) combined their dust coagulation models with streaming instability to investigate, whether it is possible to produce particles large enough to trigger the instability. They found, that this is not possible for silicate particles that are hindered by bouncing, but it might be possible for more sticky water ice particles, that can grow to larger sizes. Morbidelli et al. (2009) argue that the predicted sizes of planetesimals produced by streaming instability is consistent with the current size distribution of objects in the asteroid belt, peaking at about 100 km.

1.4 Ice Lines

Ice lines are special locations in protoplanetary disks, where the transition of the solid phase to the gaseous phase of a volatile species occurs. Outside the ice line, the

temperature is cold enough for the volatile to freeze out as ice. Inside the ice line, the temperature is high enough for the volatile species to evaporate. This means that the chemical compositions of the gas and the dust are complementary to another, since any volatile species is either in the gas or frozen out on the dust. Ice lines are therefore of special interest in planetary sciences, since they directly affect the composition of planets and planetesimals depending on their location of formation in the protoplanetary disk.

Since gas giants have had the opportunity to accrete a significant amount of hydrogen and helium gas, they must have been formed in the first few million years of during the lifetime of the disk, when there was still gas available. To be able to accrete a gaseous atmosphere gas giant cores need to have masses of at least ten Earth masses. Calculations by, e.g., Pollack et al. (1996) and Levison et al. (2010) have shown that this is hard to achieve within the typical gas disk lifetimes by pure accretion of planetary embryos onto, unless the amount of solids is increase by a factor of five to ten. However, the accretion of small pebbles can significantly reduce the growth timescale of giant planet cores (Johansen and Lacerda, 2010, Lambrechts and Johansen, 2012). Pebbles are small chondrule-sized dust particles with Stokes numbers of typically 0.01 to 0.1. Due to interactions with the gas disk, these pebbles have an increased accretion cross section onto giant planet cores. This gas drag-assisted accretion can reduce the growth timescale of giant planet cores significantly to allow for gas accretion during the first ten million years of the protoplanetary disk.

Interestingly, Espinoza et al. (2016) predicted the C/O ratios of a sample of warm gas giants. As seen in figure 1.9, the C/O ratio of the atmospheres of these giants (solid red line) is consistent with the expected C/O ratio of the solids (dashed blue line) in protoplanetary disks and not with that of the gas (solid blue line). That leads to the conclusion that the major accretion path of carbon and oxygen onto giant planets is on solids, possibly by pebble accretion, and not via gas accretion. By looking at the C/O ratio of giant planet atmospheres it is therefore possible to deduce the original formation location of the planet, should they have been migrated in the disk. By similar reasoning Ali-Dib et al. (2014) argue that Uranus and Neptune may have been formed at the carbon monoxide ice line in our solar system.

Ice lines are also very interesting with respect to dust coagulation. The rolling and breaking energies of particles are proportional to the surface energy (see equations (1.36) and (1.37)), which is a material constant. Gundlach and Blum (2015) experimentally determined the surface energy of water ice to be with $\gamma = 200\,\mathrm{erg/cm^2}$ about one order of magnitude larger than the surface energy of silicates. Therefore, water ice aggregates are able to dissipate more energy by restructuring and are harder to break compared to silicate dust. Dust aggregates that contain water ice outside the water ice line are therefore thought to be more sticky than ice free particles. Wada et al. (2009) estimated the fragmentation velocity of water ice particles to be with about $50\,\mathrm{m/s}$ significantly larger that the maximum expected collision velocities in protoplanetary disks. Dust particles outside the water ice line could therefore grow to planetesimals

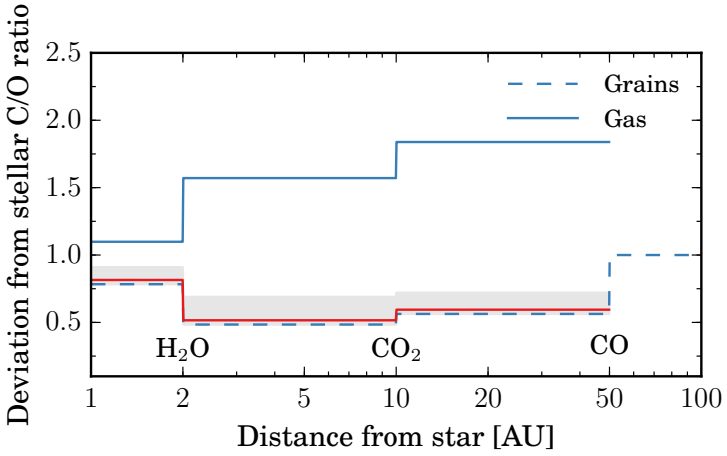

Figure 1.9: Deviations from the stellar C/O ratios of the gas (solid blue) and the dust grains (dashed blue). The C/O ratios change at the ice lines due to evaporation of volatiles. The red line is the deviation from the stellar C/O ratio estimated by Espinoza et al. (2016) from a sample of 47 warm gas giants. The gray area show the uncertainties in their calculations. The steps represent the ice lines of water, carbon dioxide, and carbon monoxide. Plot reproduced from Espinoza et al. (2016).

without fragmentation. However, Gundlach and Blum (2015) experimentally found that water ice particles start to erode at collision velocities above 10 m/s. In this case, water ice particles could grow to larger sizes but will still fragment eventually.

Figure 1.10 shows the toy model presented previously, but this time with a fragmentation velocity outside the water ice line of 50 m/s (left) and 10 m/s (right). Inside the water ice line, the fragmentation velocity remains unchanged compared to the previous toy model. In the first case, the fragmentation barrier (orange region) does not exist outside the ice line and the particles can grow to planetesimals. Further out in the disk the drift barrier still exists, since it does not depend on the fragmentation velocity. Here the particle sizes are still drift limited. Planetesimals can only be formed in a narrow region between the ice line at 1.6 AU and about 3 AU, where the dust densities and therefore the collision rates are high enough that the growth timescale is always shorter than the drift timescale.

However, due to the high surface energy of water ice, icy dust particles, in principle, could grow with very few collisional compactification, which results in very porous dust aggregates. Kataoka et al. (2013) showed that these "fluffy" aggregates can grow to sizes of several hundreds of meters while having densities comparable to air. These particles have therefore a large collisional cross section, that reduces the growth timescale. Kataoka et al. (2013) argued that such fluffy and porous aggregates can therefore overcome the drift barrier, are eventually compressed by their own grav-

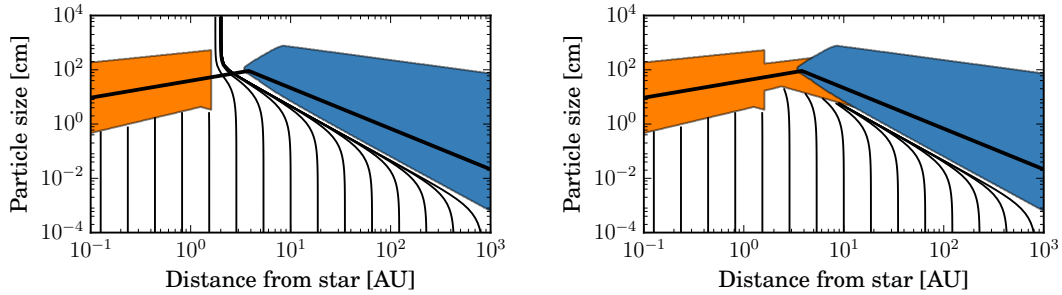

Figure 1.10: Toy model for dust growth as in figure 1.7, but with a higher fragmentation velocity outside the water ice line at 1.6 AU. In the left model the fragmentation velocity outside the ice line is set to 50 m/s, higher than the maximum expected collision velocity. The particles can grow to planetesimals. In the right model the fragmentations velocity is set to 10 m/s. This increases the maximum particle size outside the ice line by a factor 10, but does not overcome the fragmentation barrier.

itational pressure and end up with sizes and densities compared to objects observed in the asteroid belt today.

The right plot of figure 1.10 shows a toy model where the fragmentation velocity is with 10 m/s closer to the experimentally observed value for water ice particles. Here, the drift fragmentation cannot be overcome. The particles still fragment outside the ice line but can grow to larger sizes. This can be important in the context of triggering the streaming instability, which requires particles with minimum Stokes numbers of about 0.1.

Musiolik et al. (2016a) showed in experiments that particles consisting of CO_2 ice have a similar behavior to silicate particles with a surface energy of about 17 erg/cm^2. They fragment therefore at similar collision velocities in the order of 1 m/s. Furthermore, Musiolik et al. (2016b) experimentally determined the fragmentation velocities of dust aggregates consisting of mixtures of H_2O and CO_2 ice. They found that the fragmentation velocity decreases with increasing amount of CO_2, suggesting that particles outside the CO_2 ice line lose the beneficial collisional properties of water ice. Dust particles might only have high fragmentation velocities of water ice in a narrow region between the H_2O and the CO_2 ice line.

Ros and Johansen (2013) implemented evaporation and condensation in a Monte Carlo method for transporting representative ice and vapor particles in protoplanetary disks. In their model, the vapor that was created at the ice line by evaporating particles, could diffuse backwards in the disk and could recondense on the ice particles there. This created very rapidly large ice particles with sizes of a few decimeters without having collisional particle growth. Zhang et al. (2015) attributed the gaps seen in the dust emission in the disk of HL Tauri to ice lines. When particles grow by condensation

as described by Ros and Johansen (2013), the optical depth decreases and gaps in the millimeter emission appear.

Okuzumi et al. (2016) argued that these gaps are caused by sintering in regions close to ice lines. Evaporation and condensation rates depend, in general, on the curvature of the evaporating surface, with convex surfaces having higher evaporation rates than concave surfaces. Close to ice lines it can therefore happen that convex particle surfaces already evaporate, while vapor can still recondense on the concave connection points between the monomers withing an aggregate. This stiffens the contact points and prevents rolling of the monomers. Impact energy can therefore not be dissipated via rolling, but only via breaking of the connections, and thus, decreasing the fragmentation velocity. Due to increased fragmentation, the particles have on average smaller sizes and therefore smaller Stokes numbers. As seen in equation (1.31), these particles have smaller drift velocities, if they have typical Stokes number smaller than unity. This creates traffic jams in sintering regions close to ice lines, that pile up material, which can be observed as ring-like emission features in observations.

1.5 The Aim of this Thesis

This thesis consists of several different projects. The main goal of this dissertation is to connect dust coagulation models with the transport of volatile species in protoplanetary disks. As seen in figure 1.9, the chemical composition of giant planet atmospheres is determined by the chemical composition of the dust particles that are accreted onto the planet. It is therefore crucial to understand how ice lines affect the composition of dust particles and the distribution of volatile molecular species in protoplanetary disks.

In chapter 2 we implement volatile species in current models of dust coagulation and disk evolution. Outside of ice lines volatile species are frozen out as ice on dust particles. The transport of the volatile species is therefore determined by the transport of dust particles. Inside the ice line, on the other hand, the volatile is transported in the gas phase. To understand the distribution of volatiles in protoplanetary disks it is therefore important to combine dust coagulation and transport models with viscous accretion and diffusion of gas vapor. We show that inwards drifting particles deposit large amount of vapor at the ice line depending on the assumed disk conditions. This vapor can diffuse backwards in the disk and can recondense on the particles outside the ice line. This enriches the dust in a region just outside the ice line in volatiles. The C/O ratios shown in figure 1.9 are therefore not strict step functions, which should be considered in models for the chemical composition of gas giant atmospheres.

In chapter 3 we introduce fragmentation into the dust coagulation model described in chapter 2. We show that the vapor, that gets deposited at the ice line, diffuses backwards through the ice line and recondenses on the particles there. This increases the

monomer size in recondensation regions just outside of ice lines. Since the fragmentation velocity is inversely proportional to the monomer size, these regions experience enhanced fragmentation. This decreases the average particle size and therefore the drift velocity, which generates a traffic jam in the dust in these recondensation regions. This can be observed as ring-like, axis-symmetric emission features in observations of protoplanetary disks.

Chapter 4 reviews a prominent chondrule formation model. That is, the formation of chondrules in high temperature shocks propagating through protoplanetary disks. Previous one-dimensional models introduced downstream boundary conditions, that are not necessary in one-dimensional models, where all downstream parameters are automatically set by the upstreams conditions. We show, that by not imposing downstream boundary conditions, the resulting thermal histories of dust particles overrun by large scale shocks are inconsistent with the requirements imposed on chondrule formation. More realistic shocks, that are closer to actual conditions found in protoplanetary disks, are still inconsistent with chondrule formation. Finally, we show that low velocity shocks, that are not able to produce temperatures able to melt silicate material, can have an effect on water ice particles by evaporating them, which in turn, has a major effect on dust coagulation and the distribution of volatiles in protoplanetary disks. We also show that low velocity shocks can crystallize water ice particles, which could explain water ice crystals that are observed in the other parts of protoplanetary disks, where the temperature should not be high enough to produce crystals.

In chapter 5 we investigate the influence of shadows cast on protoplanetary disks on the dust dynamics in these disks. Previous observations showed shadows in protoplanetary disks that are consistent with an inner inclined disk that blocks the stellar light at two points. We performed hydrodynamical simulations of gravitationally unstable gas disks with two shadows being cast in opposite directions. The shadows trigger the gravitational collapse of the disk and produce a ring and spiral arms. Subsequent dust simulations show that the ring and the spirals trap dust particles, which are drifting in directions of pressure gradients. Radiative transfer simulations of the dust emission show that these disks look similar to a recently observed disk showing a dust ring and spirals as well.

Chapter 6 summarizes the projects described in this thesis and discusses open questions and future prospects.

2

Redistribution of CO in Evolving Gas and Dust Disks

2.1 Motivation

Ice lines are locations in protoplanetary disks at which a transition between the gaseous and the solid phase of an element or a molecular species occurs. Inwards of the ice line, the volatile species is condensed in the form of ice. Outside the ice line, the material exists in its solid form. Ice lines are of special interest in planetary sciences since they are suggested to affect the formation and composition of planetesimals (Öberg et al., 2011). Ali-Dib et al. (2014) argue from the chemical composition of Uranus and Neptune that they may have been formed at the carbon monoxide ice line.

Planetesimals are formed from dust and ice surrounding young stars in protoplanetary disks. The dust particles collide and are held together by contact forces forming ever larger bodies (see, e.g., Brauer et al., 2008, Birnstiel et al., 2010). However, experiments and simulations show that the growth is limited by at least two processes. One is the inward drift of particles on Keplerian orbits losing angular momentum to the pressure-supported gas orbiting the star with sub-Keplerian velocities (Weidenschilling, 1977a). The drift velocity is size-dependent. Therefore, particles affected by drift quickly fall onto the central star. Another mechanism that prevents grain growth is fragmentation. If the collision velocity is high enough, silicate particles tend to bounce or fragment rather than sticking together (Blum and Wurm, 2008). If particles grow to certain sizes (centimeter to decimeter), the streaming instability can take over and form planetesimals by clumping and subsequent gravitational collapse (see, e.g., Johansen et al., 2007, Youdin and Goodman, 2005, Bai and Stone, 2010, Drążkowska and Dullemond, 2014).

How particles can grow to sizes for which the streaming instability is efficient is unknown. Besides the fact that icy materials have higher fragmentation velocities than pure silicate particles (Wada et al., 2009, Gundlach and Blum, 2015), and can therefore

grow to larger sizes, several authors argue that ice lines play an important role in the growth process (e.g., Kretke et al., 2008, Brauer et al., 2008). Also, Kataoka et al. (2013) proposed that fluffy ice aggregates may overcome the drift barrier. Stevenson and Lunine (1988) found, in their model, a significant solid material enhancement at the ice line due to diffusive redistribution of vapor from the inner disk and subsequent condensation on particles outside the ice line. Closely related, Ros and Johansen (2013) proposed grain growth by evaporation of inward-drifting particles and subsequent recondensation of backwards-diffusing vapor. Cuzzi and Zahnle (2004) proposed a significant vapor enhancement inside the ice line due to rapidly inward-drifting particles.

The goal of our work is to include the transport of volatile materials into the grain growth and disk model of Birnstiel et al. (2010) and to use this model to investigate the influence of possible particle density enhancements at ice lines on dust coagulation and on the distribution of CO gas. We therefore developed a model to track the volatile content of particles and the gas including the processes of coagulation, radial drift, and viscous accretion, as well as CO evaporation and condensation at the ice line.

We focus, here, on CO ice near the CO ice line for several reasons. First, we assume that the collisional physics of the particles is mostly determined by the presence of water ice. If we further assume that the water ice content is always well mixed within the particle, there will always be enough water ice at the particle's surface such that the collisional physics does not change by crossing the CO ice line and evaporating the CO (but see also Okuzumi et al., 2016). Wada et al. (2009) estimated the fragmentation velocity of water ice particles to be ~ 50 m/s. Such high collision velocities are not reached in our model. We can therefore neglect fragmentation, since, even by total evaporation of the CO, there is still enough water ice in the particles such that we can use the higher fragmentation velocity of water ice. The growth of the particles is therefore solely limited by the inward drift. But see also Gundlach and Blum (2015), who found fragmentation velocities for water ice in the order of 10 m/s. It might also be the case that the water ice is not well mixed within the particle or that the particle is covered by a layer of CO. In that case, the fragmentation velocity is that of CO ice, which might also be lower than the fragmentation velocity of water ice.The influence of fragmentation is investigated in chapter 3.

Another reason for looking at CO is that it has observable features (Qi et al., 2015). The CO ice line at temperatures of approximately 20 K is in the outer parts of protoplanetary disks compared to other volatile species such as water ice. Furthermore, the CO abundance is generally large enough to be well observed.

We investigate the radial distribution of dust particles and molecular species in the gas and ice phases around the region of the ice line in a time dependent manner by solving the Smoluchowski equation and the redistribution of the CO vapor originating from the evaporating particles.

In section 2.2, we describe our model of advection, diffusion, grain growth, and evaporation/condensation. In section 2.3, we show the influence of the ice line on the grain growth and the influence of the advection and diffusion of the gas on the CO vapor distribution at the ice line. In section 2.4, we discuss our results and the assumptions made in the model.

2.2 Numerical Method

We constructed a model for simulating the evolution of a viscously evolving protoplanetary disk including dust coagulation, particle drift, condensation, and evaporation of CO at the CO ice line. The model is one-dimensional and the densities are vertically integrated, assuming that gas and dust are constantly in thermal equilibrium, throughout the model. We model the surface densities of approximately 150 different dust sizes $\Sigma_{\mathrm{dust},i}$ and of two gas species, $\Sigma_{\mathrm{H_2}}$ and Σ_{CO}. Our model of CO transport is built upon the gas and dust model of Birnstiel et al. (2010).

The gas disk is viscously evolving according the α-disk model of Shakura and Sunyaev (1973) while we study the diffusive behavior of CO by choosing different values for the Schmidt number Sc, which is the ratio of viscosity over diffusivity of the gas.

We model dust growth by solving the Smoluchowski equation. The dust species themselves are subject to radial drift and gas drag. In contrast to previous works, we use a two-dimensional scalar field for the particle distribution, where one dimension is the silicate mass and the second dimension the CO ice content of the particle. We therefore model the migration of CO both via drifting particles and via diffusing gas and simulate the evaporation of CO at the CO ice line by solving the Hertz-Knudsen equation.

2.2.1 Evolution of the Gas Surface Density

We consider two molecular gas species in our model, H_2 , which is the main gas density constituent, and CO, which is generally the second most abundant molecular species in the interstellar medium (ISM). The surface density of the two species, $\Sigma_{\mathrm{H_2}}$ and Σ_{CO}, and therefore the total gas density, Σ_{gas}, are directly related through the continuity equation:

$$\frac{\partial}{\partial t}\Sigma_{\mathrm{gas}} + \frac{1}{R}\frac{\partial}{\partial R}\left(R\Sigma_{\mathrm{gas}} v_{\mathrm{gas}}\right) = 0, \tag{2.1}$$

where v_{gas} is the radial gas velocity given by Lynden-Bell and Pringle (1974);

$$v_{\mathrm{gas}} = -\frac{3}{\Sigma_{\mathrm{gas}}\sqrt{R}}\frac{\partial}{\partial R}\left(\Sigma_{\mathrm{gas}}\nu\sqrt{R}\right), \tag{2.2}$$

where ν is the viscosity of the gas. Shakura and Sunyaev (1973) parameterized the viscosity in their α-disk model to account for an unknown source of viscosity with

$$\nu = \alpha c_s H_P, \tag{2.3}$$

where c_s is the sound speed, $H_P = c_s/\Omega_K$ the pressure scale height of the disk, and Ω_K the Keplerian frequency. The viscosity parameter α is typically of the order of 10^{-2} to 10^{-4} (e.g., Johansen and Klahr, 2005). Equation (2.1) has no source terms on the right hand side, because we do not consider any infall of matter from the common envelope onto the disk. Evaporation and condensation, which would also be a source or sink term for Σ_{CO}, are treated separately.

We assume that both gas species evolve separately without interacting with one another. We then obtain a separate continuity equation for each of the species j

$$\frac{\partial}{\partial t}\Sigma_j = -\frac{3}{R}\frac{\partial}{\partial R}\left[\sqrt{R}\frac{\partial}{\partial R}\left(\Sigma_j \nu \sqrt{R}\right)\right]. \tag{2.4}$$

Following the calculations of Pavlyuchenkov and Dullemond (2007), this equation can be further manipulated to

$$\begin{aligned}\frac{\partial}{\partial t}\Sigma_j &= -\frac{3}{R}\frac{\partial}{\partial R}\left[\sqrt{R}\frac{\partial}{\partial R}\left(\Sigma_{gas}\frac{\Sigma_j}{\Sigma_{gas}}\nu\sqrt{R}\right)\right] \\ &= -\frac{3}{R}\frac{\partial}{\partial R}\left[\sqrt{R}\frac{\Sigma_j}{\Sigma_{gas}}\frac{\partial}{\partial R}\left(\Sigma_j\nu\sqrt{R}\right) + R\Sigma_{gas}\nu\frac{\partial}{\partial R}\left(\frac{\Sigma_j}{\Sigma_{gas}}\right)\right],\end{aligned} \tag{2.5}$$

where $\Sigma_{gas} = \sum_j \Sigma_j$ is the total gas surface density. By substituting the gas velocity of equation (2.2) in this equation, we obtain

$$\frac{\partial}{\partial t}\Sigma_j + \frac{1}{R}\frac{\partial}{\partial R}\left(R\Sigma_j v_{gas}\right) - \frac{3}{R}\frac{\partial}{\partial R}\left[R\Sigma_{gas}\nu\frac{\partial}{\partial R}\left(\frac{\Sigma_j}{\Sigma_{gas}}\right)\right] = 0. \tag{2.6}$$

This equation implies that each gas species is radially advected with the gas velocity v_{gas} and has a diffusive term, which smears out concentrations.

By introducing the Schmidt number $Sc = \nu/D$, which is the ratio of viscosity ν to diffusivity D of a gas, one can disentangle advection and diffusion

$$\frac{\partial}{\partial t}\Sigma_j + \frac{1}{R}\frac{\partial}{\partial R}\left(R\Sigma_j v_{gas}\right) - \frac{1}{R}\frac{\partial}{\partial R}\left[R\Sigma_{gas}D\frac{\partial}{\partial R}\left(\frac{\Sigma_j}{\Sigma_{gas}}\right)\right] = 0. \tag{2.7}$$

A Schmidt number of $Sc = 1/3$ reproduces equation (2.6). Physically, the Schmidt number is the ratio of momentum transport to pure-mass transport. By changing Sc and keeping α constant, we investigate the influence of the diffusivity D on the CO distribution in the disk.

Vertical and Radial Structure of the Gas Disk

We assume that the gas is always in thermal equilibrium and that the temperature profile does not change over time. The vertical structure of the gas density is then given by

$$\rho_{\text{gas}}(z) = \rho_{\text{gas}}(z=0)\ \exp\left[-\frac{1}{2}\frac{z^2}{H_{\text{P}}^2}\right], \tag{2.8}$$

where z is the height above the midplane. Since Σ_{gas} is the z-integral of ρ_{gas} , it follows directly for the midplane gas density that

$$\rho_{\text{gas}}(z=0) = \frac{\Sigma_{\text{gas}}}{\sqrt{2\pi}\ H_{\text{P}}}. \tag{2.9}$$

Even though the model is one-dimensional, we still need the vertical structure of the disk to calculate the densities at the midplane that are needed for the coagulation as well as for the evaporation method.

In our fiducial model, we used the following power law as initial surface density distribution:

$$\Sigma_{\text{gas}}(R) = 250\frac{\text{g}}{\text{cm}^2} \times \left(\frac{R}{1\ \text{AU}}\right)^{-1}. \tag{2.10}$$

Temperature Structure of the Disk

For the midplane temperature of the disk, we assume a simple power law;

$$T(R) = 150\ \text{K}\ \times\ \left(\frac{R}{1\ \text{AU}}\right)^{-\frac{1}{2}}, \tag{2.11}$$

that remains constant in time. The viscous heating rate, which is the energy that is created by the viscous accreting of the gas, is proportional to the gas density Σ_{gas} (Nakamoto and Nakagawa, 1994) and therefore mainly important in the inner part of the disk. Since we are interested in the region of the CO ice line at 40 AU to 50 AU where the densities are low, this effect is negligible.

2.2.2 Radial Evolution of the Dust Surface Density

The spatial evolution of the dust particles is strongly influenced by interactions with the gas. Although it is possible, in real disks, that particles become locally concentrated to gas-to-dust ratios of unity or less, especially at the disk's midplane, and therefore trigger streaming instabilities, we neglect this here, and assume that accumulations of

dust happen only at smaller radii (Youdin and Shu, 2002) or on smaller scales (Youdin and Goodman, 2005). In other words: the gas has an effect on the dust particles, but the dust particles have no back-reaction on the gas in our model.

To describe the coupling of the particles to the gas, it is useful to characterize the particles not by size but by their dimensionless Stokes number St. The Stokes number is defined as the ratio of the stopping time τ_s of the particles to the largest eddy's turn-over time τ_{ed};

$$\mathrm{St} = \frac{\tau_s}{\tau_{ed}}. \tag{2.12}$$

The Stokes number can be used as a measure to describe the coupling between the gas and the dust. Since this coupling depends not solely on the particle size but, amongst other parameters, also on the gas density, it is convenient to use the Stokes number to describe the equations of motion of the particles.

The stopping time τ_s in equation (2.12) is the ratio between a particle's momentum and the rate of its momentum change by the drag force. It yields the time scale on which a particle adapts to the gas velocity. Weidenschilling (1977a) identified four different regimes of the drag force. The important regime in our work is the Epstein regime, where the stopping time is given by

$$\tau_s = \frac{\rho_s \, a}{\rho_{gas} \, \bar{v}}, \tag{2.13}$$

with the bulk density of the solids ρ_s and the particle size a. $\bar{v} = c_s\sqrt{8/\pi}$ is the mean thermal velocity of the gas molecules. In protoplanetary disks, the Stokes I drag regime is important only in the inner part of the disk ($\lesssim 1\,\mathrm{AU}$). We therefore only include the Epstein regime in this work.

As a first order approximation for the eddy turnover time, one can use $\tau_{ed} = 1/\Omega_K$ (Schräpler and Henning, 2004), and obtain the Stokes number:

$$\mathrm{St} = \frac{\rho_s \, a}{\Sigma_{gas}} \frac{\pi}{2}. \tag{2.14}$$

The advection of the dust surface densities of the different species can now be described with a continuity equation as equation (2.7)

$$\frac{\partial}{\partial t}\Sigma_{dust,i} + \frac{1}{R}\frac{\partial}{\partial R}\left(R\left[\Sigma_{dust,i} v_{dust,i} - D_{dust,i}\Sigma_{gas}\frac{\partial}{\partial R}\frac{\Sigma_{dust,i}}{\Sigma_{gas}}\right]\right) = 0, \tag{2.15}$$

where $D_{dust,i} = \alpha c_s H_P/(1+\mathrm{St}^2)$ is the dust diffusivity and $v_{dust,i}$ the radial velocity of dust species i given by

$$v_{dust,i} = \frac{v_{gas}}{1+\mathrm{St}_i^2} - \frac{2v_P}{\mathrm{St}_i + \mathrm{St}_i^{-1}}. \tag{2.16}$$

This velocity consists of two terms. The first term describes the dust particles that are dragged along with the inwards accreting gas; it is most effective for small particles ($\mathrm{St} \ll 1$) that are well-coupled to the gas and insignificant for large particles ($\mathrm{St} \gg 1$). The second term describes radial drift due to a pressure gradient in the gas. The gas feels an additional force due to its own pressure gradient. If the pressure gradient is pointing inwards, then the gas is on a sub-Keplerian orbit. The acceleration of the dust particles due to the pressure force, on the other hand, is negligible because of their high bulk density compared to the gas. Therefore, the particles try to orbit with a Keplerian velocity. Due to this velocity difference with the gas, they feel a constant headwind, lose angular momentum, and drift in the direction of the pressure gradient. The maximal drift velocity (for particles with $\mathrm{St} = 1$) is given by Weidenschilling (1977a) as

$$v_\mathrm{P} = -\frac{\frac{\partial}{\partial R} P_\mathrm{gas}}{2\rho_\mathrm{gas}\Omega_\mathrm{K}}. \tag{2.17}$$

2.2.3 Vertical Structure of the Dust Disk

Since the dust particles do not feel any pressure amongst themselves, we cannot give a simple pressure-equilibrium expression for the particle scale heights as for the gas scale height H_P. The particle scale heights are given by the equilibrium of vertical settling by gravity and turbulent stirring and therefore depend on the particle's Stokes number. Therefore, every particle size has its own scale height. We follow, here, Brauer et al. (2008) for the description of the scale height of species i as

$$h_i = H_\mathrm{P} \cdot \min\left(1, \sqrt{\frac{\alpha}{\min\left(\mathrm{St}_i, \frac{1}{2}\right) \cdot \left(1 + \mathrm{St}_i^2\right)}}\right), \tag{2.18}$$

which limits the dust scale height to be, at maximum, equal to the gas scale height H_P. From this equation, it can be seen that larger particles ($\mathrm{St} \gg 1$) are settled to the midplane, while small particles ($\mathrm{St} \ll 1$) follow the gas scale height. A stronger turbulence (i.e., larger turbulent viscosity parameter α), in general, increases the scale height up to a maximum of H_P.

We assume that the particles are distributed with Gaussian distributions just as the gas in equation (2.8), but with the dust particle's specific scale height h_i instead, which allows us to analytically integrate the Smoluchowski equation vertically.

2.2.4 Dust Coagulation

We include dust growth in our model to study the CO redistribution in protoplanetary disks. The dust carries the CO ice inwards through the CO ice line. As seen in equation

(2.16), the Stokes number, and therefore the particle size, is important for the drift velocity of the dust particles.

We therefore include hit-and-stick collisions of particles in our model. We neglect fragmentation because the CO ice line is well outside of the water ice line, meaning that, everywhere in our model, the particles have a significant amount of water ice, which is also mixed within the particle in such a way that the particle collision properties are always determined by the water ice. As explained above, we therefore neglect fragmentation.

Smoluchowski Equation

The growth of the dust particles with mass m by hit-and-stick collisions without fragmentation can be described by the Smoluchowski equation

$$\begin{aligned}\frac{\partial}{\partial t} f(m) =& \frac{1}{2} \int_0^\infty \mathrm{d}m' \int_0^\infty \mathrm{d}m'' f(m') f(m'') K(m'; m'') \times \\ & \times \delta(m' + m'' - m) \\ & - f(m) \int_0^\infty \mathrm{d}m' f(m') K(m; m'),\end{aligned} \tag{2.19}$$

where the collision kernel $K(m; m') = \sigma_{\mathrm{geo}}(m; m') \Delta v(m; m')$ is the product of the geometrical cross section and the relative velocity of the colliding particles. Equation (2.19) is a partial differential equation for the time evolution of a mass distribution of particles. The positive term on the right-hand side counts collisions that lead to particles of mass m. The negative term removes particles of mass m that collided with other particles to create larger particles.

To keep track of not only the mass of the particles, but also of another property that represents the CO ice content of them, we add another parameter Q to our distribution. The following equations are general for an arbitrary Q that could represent anything from the volume of the particle as in Okuzumi et al. (2009) to the electrical charge of

the particle. In the following sections we identify Q with the particle's ice fraction. The two-dimensional Smoluchowski equation then reads as follows

$$\begin{aligned}\frac{\partial}{\partial t} f(m,Q) = & \frac{1}{2}\int_0^\infty \mathrm{d}m' \int_0^\infty \mathrm{d}m'' \int_0^\infty \mathrm{d}Q' \int_0^\infty \mathrm{d}Q'' \times \\ & \times f(m',Q')\, f(m'',Q'') \times \\ & \times K(m',Q';m'',Q'') \times \\ & \times \delta(m'+m''-m) \\ & \times \delta\left(Q^{\mathrm{new}}(m',Q';m'',Q'')-Q\right) \\ & - f(m,Q)\int_0^\infty \mathrm{d}m' \int_0^\infty \mathrm{d}Q' f(m',Q') \times \\ & \times K(m,Q;m'Q'),\end{aligned} \tag{2.20}$$

where $Q^{\mathrm{new}}(m',Q';m'',Q'')$ is the new Q-value of the particle that was created in the collision. In principle, this equation could be solved as for equation (2.19), but adding another parameter and therefore two additional integrals would be computationally very expensive.

We therefore follow the moment method introduced by Okuzumi et al. (2009) to rewrite one two-dimensional Smoluchowski equation into two one-dimensional equations. The idea is that instead of evolving the full Q- distribution, we only evolve its first moment, its mean $\bar{Q}$ for a given mass m. By introducing the distribution function of particles of mass m

$$n(m) = \int_0^\infty f(m,Q)\,\mathrm{d}Q, \tag{2.21}$$

and the mean Q-value of particles with mass m

$$\bar{Q}(m) = \frac{1}{n(m)}\int_0^\infty Q f(m,Q)\,\mathrm{d}Q, \tag{2.22}$$

and by assuming that the particle distribution is very sharp in Q

$$f(m,Q) = n(m)\,\delta\left(\bar{Q}(m)-Q\right), \tag{2.23}$$

where δ is the Dirac delta function, equation (2.20) can be rewritten and simplified. We end up with one partial differential equation for $n(m)$

$$\begin{aligned}\frac{\partial}{\partial t}n(m) =& \frac{1}{2}\int_0^\infty \mathrm{d}m' n(m')\, n(m-m') \times \\ & \times K\left(m', \bar{Q}(m'); m-m', \bar{Q}(m-m')\right) \\ & - n(m)\int_0^\infty \mathrm{d}m' n(m')\, K\left(m, \bar{Q}(m); m', \bar{Q}(m')\right),\end{aligned} \tag{2.24}$$

and one equation for $n\bar{Q}(m) \equiv n(m)\,\bar{Q}(m)$

$$\begin{aligned}\frac{\partial}{\partial t}\left(n\bar{Q}(m)\right) =& \frac{1}{2}\int_0^\infty \mathrm{d}m' n(m')\, n(m-m') \times \\ & \times K\left(m', \bar{Q}(m'); m-m', \bar{Q}(m-m')\right) \times \\ & \times Q^{\mathrm{new}}\left(m', \bar{Q}(m'); m-m', \bar{Q}(m-m')\right) \\ & - n\bar{Q}(m)\int_0^\infty \mathrm{d}m' n(m')\, K\left(m, \bar{Q}(m); m', \bar{Q}(m')\right),\end{aligned} \tag{2.25}$$

as derived by Okuzumi et al. (2009). Both one-dimensional equations can be simultaneously solved, which is significantly more efficient than solving one two-dimensional equation. The coagulation equations (2.24) and (2.25) and the dust advection equation (2.7) are simultaneously solved as in Birnstiel et al. (2010).

The Q-parameter

We have now the freedom of choice on what exactly the physical meaning of our Q-parameter should be. One way to include ices in our coagulation code is to take $m = m^{\mathrm{tot}}$ as the total mass and $Q = m^{\mathrm{ice}}/m$ as the ice fraction of a particle. However, this approach has the disadvantage that as a result of evaporation and condensation, both parameters m and Q change. In this case, evaporation/condensation would be advection of the function $Q(m,t)$ in the m-coordinate with an additional source term.

We therefore chose $m = m^{\mathrm{sil}}$ as the silicate mass and $Q = m^{\mathrm{ice}}/\left(m^{\mathrm{sil}} + m^{\mathrm{ice}}\right)$ as the ice fraction of a particle. Here, evaporation and condensation only change Q and not m.

By using this approach, the ice mass of a particle is $m^{\mathrm{ice}} = \frac{Q}{1-Q}m^{\mathrm{sil}}$, whereas the total mass is $m^{\mathrm{tot}} = \frac{1}{1-Q}m^{\mathrm{sil}}$. Therefore, we cannot model particles fully consisting of ice $(Q = 1)$. Q^{new} , which is the new Q-value of a particle resulting from a collision

followed by sticking between a particle with mass m and another particle with mass m' (and ice fractions Q and Q', respectively), is then determined by

$$\begin{aligned} Q^{\text{new}}\left(m, Q; m', Q'\right) &= \frac{m^{\text{ice}} + m^{\text{ice}'}}{m^{\text{tot}} + m^{\text{tot}'}} \\ &= \frac{\frac{Q}{1-Q} m + \frac{Q'}{1-Q'} m'}{\frac{1}{1-Q} m + \frac{1}{1-Q'} m'} \\ &= \frac{\left(1-Q'\right) Q m + \left(1-Q\right) Q' m'}{\left(1-Q'\right) m + \left(1-Q\right) m'}. \end{aligned} \tag{2.26}$$

Relative Velocities

The coagulation is driven by the relative velocities of the particles that determine the collision rates and the possible collision outcome. We consider, here, five different sources of relative velocities as described in chapter 1: Brownian motion Δv_{bm}, azimuthal particle drift Δv_{ad}, radial particle drift Δv_{rd}, vertical settling Δv_{vs} , and turbulence Δv_{turb}.

The total relative velocity is then given by the root mean square of all sources of relative velocity

$$\Delta v = \sqrt{\Delta v_{\text{bm}}^2 + \Delta v_{\text{rd}}^2 + \Delta v_{\text{ad}}^2 + \Delta v_{\text{vs}}^2 + \Delta v_{\text{turb}}^2}. \tag{2.27}$$

We assume that all particles of a certain size collide with this distinct mean velocity. It has been shown that the use of a velocity distribution can have a significant influence on dust growth by breaking through growth barriers as the bouncing barrier or the fragmentation barrier (Windmark et al., 2012b, Garaud et al., 2013). Since we are not dealing with bouncing and/or fragmentation in this model, we do not consider any velocity distribution.

2.2.5 Evaporation and Condensation

When particles drift inwards they move from colder regions in the disk to warmer regions. At some point at the ice line the temperature is high enough for the ice in the particles to be evaporated. The vapor that is created by evaporation can then be diffused backwards through the ice line and can recondense on the colder particles there. We therefore consider both evaporation and condensation along with diffusion and viscous evolution of the gas in our model.

We assume that the particles always adapt instantaneously to the new temperature. This might not be the case for very large particles with high heat capacities. But as seen later in Section 2.3, we do not have such large particles. The temperature change

our particles experience is solely caused by their drift from colder regions to warmer regions in the disk. With typical drift speeds, the particles experience a change in temperature of less than 1 K in 1 000 yrs. The assumption of instantaneous adaption to the ambient temperature is therefore well justified.

Evaporation/condensation can be described by the Hertz-Knudsen equation which gives the number of CO molecules N per unit surface area that leave the particle,

$$\frac{\mathrm{d}}{\mathrm{d}t}N = v_{\mathrm{therm}} \left(\frac{P^{\mathrm{eq}}}{k_{\mathrm{B}}T} - n_{\mathrm{vap}} \right), \tag{2.28}$$

where n_{vap} is the number density of vapor molecules, P^{eq} the saturation pressure of the volatile species and $v_{\mathrm{therm}} = \sqrt{8k_{\mathrm{B}}T/\left(\pi m_{\mathrm{CO}}\right)}$ is the mean thermal velocity of gas molecules of mass m_{CO}. If the ambient pressure of the volatile species equals the saturation pressure then there is no net evaporation.

P^{eq} has to be determined experimentally. We use the values from Leger et al. (1985) as

$$P^{\mathrm{eq}}_{\mathrm{CO}}\left(T\right) = 1\frac{\mathrm{dyn}}{\mathrm{cm}^2} \times \exp\left[-\frac{1030\ \mathrm{K}}{T} + 27.37 \right]. \tag{2.29}$$

Evaporation/condensation is, in general, dependent on the surface curvature of the particle, where convex surfaces have slightly higher evaporation rates than concave surfaces (Sirono, 2011b). We do not consider those surface curvature effects in our model. This means if equation (2.28) is negative, we have condensation on all particles independent of their size. If equation (2.28) is positive, all particles evaporate as long as they still carry some ice.

The Hertz-Knudsen equation needs to be solved for every particle size at every radial and vertical position of the disk separately and simultaneously. But since we are not dealing with the vertical structure of the disk in our model, we need to transfer this expression into an expression for surface densities. If we look at the midplane of the disk, the Hertz-Knudsen equation for the midplane vapor mass density reads as

$$\frac{\mathrm{d}}{\mathrm{d}t}\rho_{\mathrm{vap}} = \sum_i \pi a_i^2 \; n_{\mathrm{dust,i}} \; v_{\mathrm{therm}} \left(\frac{m_{\mathrm{CO}} P^{\mathrm{eq}}}{k_{\mathrm{B}}T} - \rho_{\mathrm{vap}} \right), \tag{2.30}$$

where a_i is the particle radius and $n_{\mathrm{dust,i}}$ the midplane number density of dust particles species i. This system is in equilibrium if

$$\rho_{\mathrm{vap}} = \frac{m_{\mathrm{CO}}\ P^{\mathrm{eq}}}{k_{\mathrm{B}}T} \equiv \rho^{\mathrm{eq}}_{\mathrm{vap}}, \tag{2.31}$$

where $\rho^{\mathrm{eq}}_{\mathrm{vap}}$ is defined as the equilibrium vapor mass density. If we assume that the vapor is always in pressure equilibrium, we get for the equilibrium vapor surface density

$$\Sigma^{\mathrm{eq}}_{\mathrm{vap}} = \sqrt{2\pi}\ H_{\mathrm{P}}\ \rho^{\mathrm{eq}}_{\mathrm{vap}} = \sqrt{2\pi}\ H_{\mathrm{P}}\ \frac{m_{\mathrm{CO}}\ P^{\mathrm{eq}}}{k_{\mathrm{B}}T}. \tag{2.32}$$

Assuming this, we can transform equation (2.30) into an expression for the vapor surface density

$$\begin{aligned}\frac{\mathrm{d}}{\mathrm{d}t}\Sigma_{\mathrm{vap}} &= \sum_i \pi a_i^2 \, n_{\mathrm{dust,i}} \, v_{\mathrm{therm}} \, \left(\Sigma_{\mathrm{vap}}^{\mathrm{eq}} - \Sigma_{\mathrm{vap}}\right) \\ &= \sum_i \left(E_i - C_i \Sigma_{\mathrm{vap}}\right) \\ &= E - C\Sigma_{\mathrm{vap}} \equiv -S,\end{aligned} \tag{2.33}$$

with

$$C_i = \pi a_i^2 v_{\mathrm{therm}} n_{\mathrm{dust},i} \tag{2.34}$$

$$E_i = C_i \Sigma_{\mathrm{vap}}^{\mathrm{eq}}. \tag{2.35}$$

Therefore, the change in the ice surface density of particle species i is given by

$$\frac{\partial}{\partial t}\Sigma_{\mathrm{ice},i} = C_i \Sigma_{\mathrm{vap}} - E_i, \tag{2.36}$$

which is the difference between a condensation term $C_i\Sigma_{\mathrm{vap}}$ and an evaporation term E_i. The deeper meaning behind this formalism is that we treat the evaporation and condensation rates as if the particles were in the midplane, while we assume that gas and particles are always in thermal equilibrium and distributed according to their pressure scale heights H_{P} and h_i.

For C_i and E_i , the following relation holds:

$$\frac{E_i}{C_i} = \frac{E}{C}. \tag{2.37}$$

Condensation Mode

If $S > 0$, then we are in the *condensation regime* and condensation will take place on all particles. In that case, we can directly integrate equations (2.36) and (2.33) until the end of the time step. If we assume that the particle radius a_i is constant and does not change over the time step, then both equations have analytic solutions. This assumption is justified if we use a canonical abundance of CO of 10^{-4}. By using a dust to gas ratio of 10^{-2} , this leads to an initial mass ratio of CO (gas and ice phase) to dust of $\sim$ 14 %, and therefore a maximal change in radius of $\sim$ 5 %. The analytic solution of equation (2.33) is then

$$\Sigma_{\mathrm{vap}}\left(t\right) = \Sigma_{\mathrm{vap}}\left(t_0\right) e^{-C(t-t_0)} + \frac{E}{C}\left(1 - e^{-C(t-t_0)}\right). \tag{2.38}$$

Using equation (2.38) in equation (2.36) leads to

$$\begin{aligned}\frac{\partial}{\partial t}\Sigma_{\mathrm{ice},i} &= -E_i + C_i\Sigma_{\mathrm{vap}} \\ &= -E_i + C_i\left(\Sigma_{\mathrm{vap}}\left(t_0\right)e^{-C(t-t_0)} + \frac{E}{C}\left(1-e^{-C(t-t_0)}\right)\right) \\ &= \left(C_i\Sigma_{\mathrm{vap}}\left(t_0\right) - E_i\right)e^{-C(t-t_0)},\end{aligned} \tag{2.39}$$

where in the last step, equation (2.37) was used. This equation has the analytical solution

$$\Sigma_{\mathrm{ice},i}\left(t\right) = \Sigma_{\mathrm{ice},i}\left(t_0\right) + \frac{C_i\Sigma_{\mathrm{vap}}\left(t_0\right) - E_i}{C}\left(1-e^{-C(t-t_0)}\right). \tag{2.40}$$

Equations (2.38) and (2.40) can be used to calculate the surface densities at any time step directly.

Evaporation Mode

If at the start of the time step $S < 0$, we are in an *evaporation regime*. Also in this regime, the time evolution is governed by equations (2.38) and (2.40). However, we need to take into account that bare grains will not contribute to the flux of molecules, and that during the time step, grains may become bare. Therefore, we split the integration into a number of sub-steps. During each sub-step, the same set of grain sizes contributes to the evaporation flux, and we completely ignore bare grains. For each step, we define restricted versions of C and E. These restricted versions only sum over non-bare grains;

$$C_{\mathrm{rest}} = \sum_{i,\ \text{not bare}} C_i \qquad \text{and} \qquad E_{\mathrm{rest}} = \sum_{i,\ \text{not bare}} E_i. \tag{2.41}$$

We define bare grains as particles that have less than one mono-layer of ice molecules on their surface.

With these definitions, we use equation (2.40) to check if any ice component becomes depleted during the time step, that is, we check for the first root in any of the equations;

$$\Sigma_{\mathrm{ice},i}\left(t_0\right) + \frac{C_i\Sigma_{\mathrm{vap}}\left(t_0\right) - E_i}{C}\left(1-e^{-C(t-t_0)}\right) = 0. \tag{2.42}$$

If that first root is before the end of the time step, we evolve the system to this time, remove the newly bare grain size from the participating set of grain sizes, and continue in the same way. Eventually, either all grains will be bare, or the first root in the set of equations (2.42) will be beyond the end of the time step. Then we use equation (2.40) with C replaced by C_{rest} to move the system to the end of the time step.

Caveats

We do not consider grain curvature effects on evaporation and condensation. This means either all particles are in evaporation mode or all particles are in condensation mode. In general, this effect is mostly effective for very small particles ($< 0.1\,\mu$m). As seen in section 2.3, we get rid of the small particles very quickly due to coagulation and do not replenish them since we do not have fragmentation.

The surface of a real disk is directly illuminated by the star and therefore hotter than the midplane. This means that in addition to a radial ice line in the midplane, disks also have a two-dimensional surface called atmospheric ice line towards their surface, where the temperatures are high enough for ices to evaporate. Since we are only looking at midplane quantities to decide between evaporation or condensation, we neglect the atmospheric ice line. This leads to an overestimation of the ice content of the particles. But since most of the dust mass is basically below the vertical ice line, especially the larger grains, the effect is only expected to be important near the radial ice line where the vertical ice line reaches the midplane. However, this is a radially narrow region, so it shouldn't affect the global transport, but possibly modifies the shape of the snow line.

Our particles have a relatively simple structure in the model. They are treated as particles with a core and a mantle of CO. If two particles with mantles collide in our model, they form a new particle with a single core and a mantle instead of a particle with two cores connected at their contact point, or even more complex fragmented structures. This may lead to an artificial growth of silicate particles. If we consider the case where outside the ice line, many particles with CO mantles collide; in our model they form a large particle with a large single core and a large CO mantle. By crossing the ice line and evaporating the CO, we are then left with this large core instead of many small cores. Aumatell and Wurm (2011) showed, experimentally, that by evaporating fractal ice particles, one would expect to be left with many small particles instead of one large particle. In favor of simplicity, we neglect this effect.

Furthermore, the evaporation of CO ice can be decreased if some of the CO ice is trapped inside a porous and spatially complex structure of the dust particle. Or it can be increased if the dust particle is very fluffy because its surface area is then much larger than in the case of a spherical particle of the same size. These effects are also ignored in this work.

Table 2.1: Fiducial model parameters.

Parameter	Symbol	Value	Unit
Viscosity parameter	α	10^{-3}	–
Schmidt number	Sc	1/3	–
Stellar mass	M_{star}	1.0	$M_\odot$
Gas-to-dust ratio	f_{g2d}	100	–
Gas-to-CO ratio	f_{g2CO}	700	–
Silicate bulk density	ρ_{sil}	1.6	g/cm^3
CO bulk density	ρ_{CO}	1.6	g/cm^3

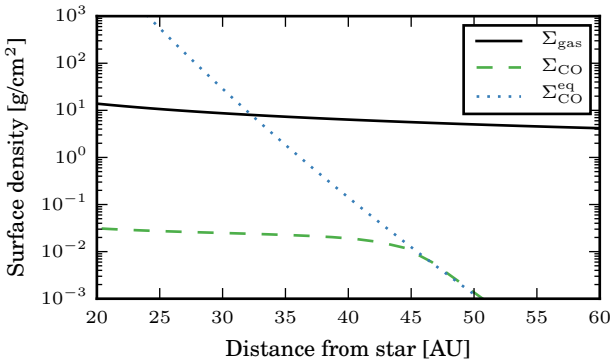

Figure 2.1: Gas surface densities of the fiducial model after 1 Myr. Shown are the total gas surface density solid black line) and the surface density of gaseous CO (dashed green line). The dotted blue line is the equilibrium surface density of CO given by equation (2.32). The location where the CO surface density detaches from the equilibrium CO surface density is called the ice line.

2.3 Results

The Fiducial Model

The input quantities of our fiducial model are given in table 2.1. The grain sizes are initially distributed with the MRN distribution (Mathis et al., 1977) with an upper cutoff at 1 ¯m. We integrate the equations (2.7), (2.15), (2.24), and (2.25) and use the method for evaporation/condensation as described in section 2.2.5 to calculate the time evolution of the gas surface densities $\Sigma_{\text{H}_2}$and Σ_{CO}, and the dust surface densities of the different grain sizes $\Sigma_{\text{dust},j}$.

Figure 2.1 shows the gas surface densities after 1 Myr of the simulation. We have chosen this value, because it is the typical age of some of the best studied star-forming regions and thus also of the disks therein. Also, it is the typical timescale for disk

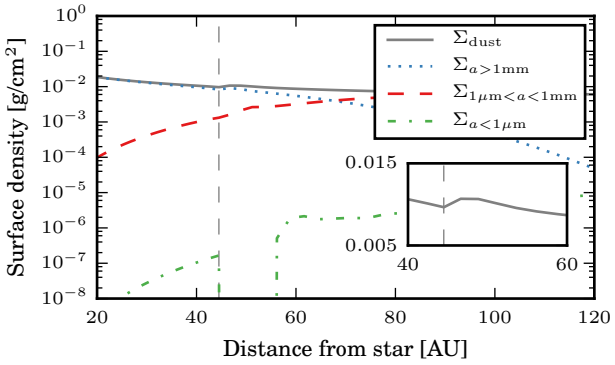

Figure 2.2: Dust surface densities of different dust sizes at the CO ice line after 1 Myr. Shown are the total surface density (solid gray line), millimeter-sized (dotted blue line), sub-millimeter-sized (dashed red line), and sub-micrometer-sized (dash-dotted green line) particles. The vertical dashed line marks the location of the CO ice line.

dispersion (e.g., Haisch et al., 2001). Shown is the total gas surface density $\Sigma_{\rm gas} = \Sigma_{\rm H_2} + \Sigma_{\rm CO}$ and the CO gas surface density $\Sigma_{\rm CO}$. Overplotted is the equilibrium CO gas surface density $\Sigma^{\rm eq}_{\rm CO}$ given by equation (2.32), which the system would have if there was no net evaporation/condensation and if there was enough CO available. If there is not enough CO in the system, then the CO in the particles evaporates until the grains are bare. The radial distance, where $\Sigma_{\rm CO}$ detaches from $\Sigma^{\rm eq}_{\rm CO}$, is then our definition of the CO ice line because it is the point where there is just enough CO in our model to provide the vapor pressure necessary to counterbalance the evaporation. In our fiducial model, this happens at ~ 47 AU. Outside the ice line, the CO is frozen out onto the grains until $\Sigma_{\rm CO} = \Sigma^{\rm eq}_{\rm CO}$. Inside the ice line, all CO is in the gas phase. Although it is not a power law, the equilibrium density at the position of the ice line can be approximated by $\Sigma^{\rm eq}_{\rm CO} \propto R^{-p}$ with $p \approx 20$. Since this is very steep, the region around the ice line, where the CO is partially condensed, is very small and therefore the ice line is well defined.

Figure 2.2 shows the total dust surface density $\Sigma_{\rm dust}$ and the surface densities $\Sigma_{a>1\,\rm mm}$ of grains larger than one millimeter, $\Sigma_{1\,\mu\rm m<a<1\,mm}$ of grain sizes between 1 mm and 1 μm, and $\Sigma_{a<1\,\mu\rm m}$ of sub-micrometer-sized grains after 1 Myr. The total dust surface density outside of 70 AU is dominated by sub-millimeter-sized grains. The amount of millimeter-sized grains becomes important inside of 70 AU. The reason for that is that the maximum size of the particles is limited by radial drift. As particles grow to larger sizes, their Stokes number increases. In the Epstein regime of drag, which is relevant in this work, particles of the same size have a larger Stokes number in regions of smaller gas density. This means that particles of a given size drift faster in the outer

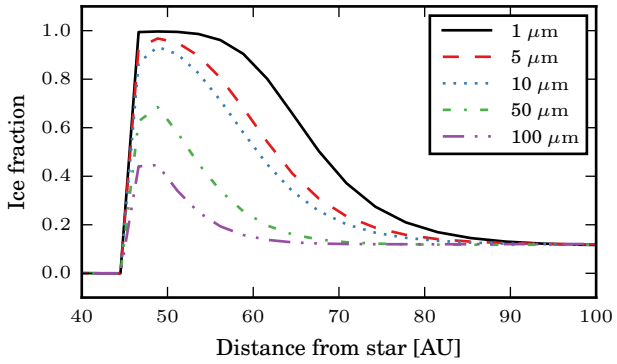

Figure 2.3: The CO ice fraction Q of particles with different silicate core sizes depending on their radial position in the disk after 1 Myr.

region of the disk. When the particles grow and their Stokes numbers approach unity, they are heavily affected by radial drift and drift rapidly towards the central star.

We do not see any enhanced particle growth at the ice line. The reason for that is the so-called drift barrier. If particles drift through the ice line and evaporate their CO, this CO vapor can diffuse backwards through the ice line and can recondense on the particles there. These particles then grow in size. Therefore, their Stokes number increases and with that their drift velocity, making them drift even faster through the ice line.

In fact, the feature we see in Σ_{dust} in figure 2.2 at the ice line should rather be seen as a depletion inside the ice line instead of an enhancement outside, because it is solely caused by evaporation of the CO ice on the inwards drifting particles. This depletion approximately corresponds to the input ratios of f_{g2d} and f_{g2CO}.

Figure 2.2 also shows a complete lack of sub-micrometer sized grains in a region of approximately 10 AU outside the ice line. Those particles do not exist here, because the backwards diffusing CO vapor preferentially recondenses on the smallest particles since they contribute the most to the total surface area. Therefore, these particles grow in size. The particles with the smallest silicate cores have ice fractions of $Q > 0.999$. Therefore, their mass is enhanced by a factor of at least 1 000 and their radius by a factor of at least 10. Particles with a silicate core of $a_{\text{sil}} < 1\,\mu m$ therefore have a resulting radius of $a_{\text{real}} > 1\,\mu m$.

Figure 2.3 shows these ice fractions $Q\,(R)$ as a function of distance from the star after 1 Myr of the simulation for different silicate core sizes of the particles. Since we do not take into account any curvature effects for our evaporation/condensation algorithm, this means the evaporation/condensation rate per unit surface area is the same for all particle sizes. In the case of condensation, the absolute change in radius would be the same for all particles independent of their size. But the relative gain in particle mass

is therefore larger for smaller particles and therefore their Q-value increases faster. Figure 2.3 shows this effect. The smaller the particle is, the larger its CO ice fraction Q at the ice line at 47 AU. Also, it can be seen that the CO vapor is redistributed to large distances outwards of the ice line. Even at $R > 70$ AU, there is a noticeable increase of Q for the small particles.

Figure 2.4 shows different snapshots of the size evolution in our fiducial model. Plotted are the following distribution functions:

$$\begin{aligned} \sigma_{\text{dust, tot}}(a; R) &= \int_{-\infty}^{\infty} n(a; R, z) \cdot m \cdot a \, \mathrm{d}z \\ \sigma_{\text{dust, CO}}(a; R) &= \int_{-\infty}^{\infty} nQ(a; R, z) \cdot m \cdot a \, \mathrm{d}z. \end{aligned} \tag{2.43}$$

The solid line denotes the particles with a Stokes number of unity. The dashed line is an analytical estimate of the maximum drift-limited particle size as given by Birnstiel et al. (2012). At first, the particle growth is most effective in the inner regions of the disk because of the larger collission rates of the particles. The particle growth is later hindered by radial drift. In the snapshots at 500 000 yrs and 1 Myr, a region from the ice line at 47 AU outwards can be seen where there are no small particles (dotted line). Because of the recondensation of CO, these particles grow in size. The distribution functions σ are therefore compressed towards larger sizes leading to the darker spot at intermediate particle sizes in the μm range. The total number density of particles has no discontinuity at the ice line.

To investigate the typical particle size $\bar{a}_m$ that carries most of the CO ice mass and the typical particle size $\bar{a}_F$ that transports most of the CO ice, we define the following quantities:

$$\bar{a}_m(R) = \frac{\int a \cdot \sigma_{\text{dust, CO}} \, \mathrm{dln}a}{\int \sigma_{\text{dust, CO}} \, \mathrm{dln}a} \tag{2.44}$$

$$\bar{a}_F(R) = \frac{\int a \cdot v_{\text{gas}} \cdot \sigma_{\text{dust, CO}} \, \mathrm{dln}a}{\int v_{\text{gas}} \cdot \sigma_{\text{dust, CO}} \, \mathrm{dln}a}. \tag{2.45}$$

$\bar{a}_m$ is the average particle size weighted by the CO dust distribution and $\bar{a}_F$ is the average particle size weighted by the CO ice flux. Both quantities are plotted in figure 2.5. It can be seen by comparing figure 2.5 with figure 2.4 that $\bar{a}_m$ is always close to the maximum particle size. Furthermore, $\bar{a}_m$ is always close to the particle size $\bar{a}_F$ that is responsible for the ice flux on the particles in the disk.

2.3.1 Transport of CO in the Dust Phase

Figure 2.6 shows the excess in total dust surface density compared to a model without CO, the dust-to-gas ratio and the ice-to-dust ratio for different values of the initial gas-

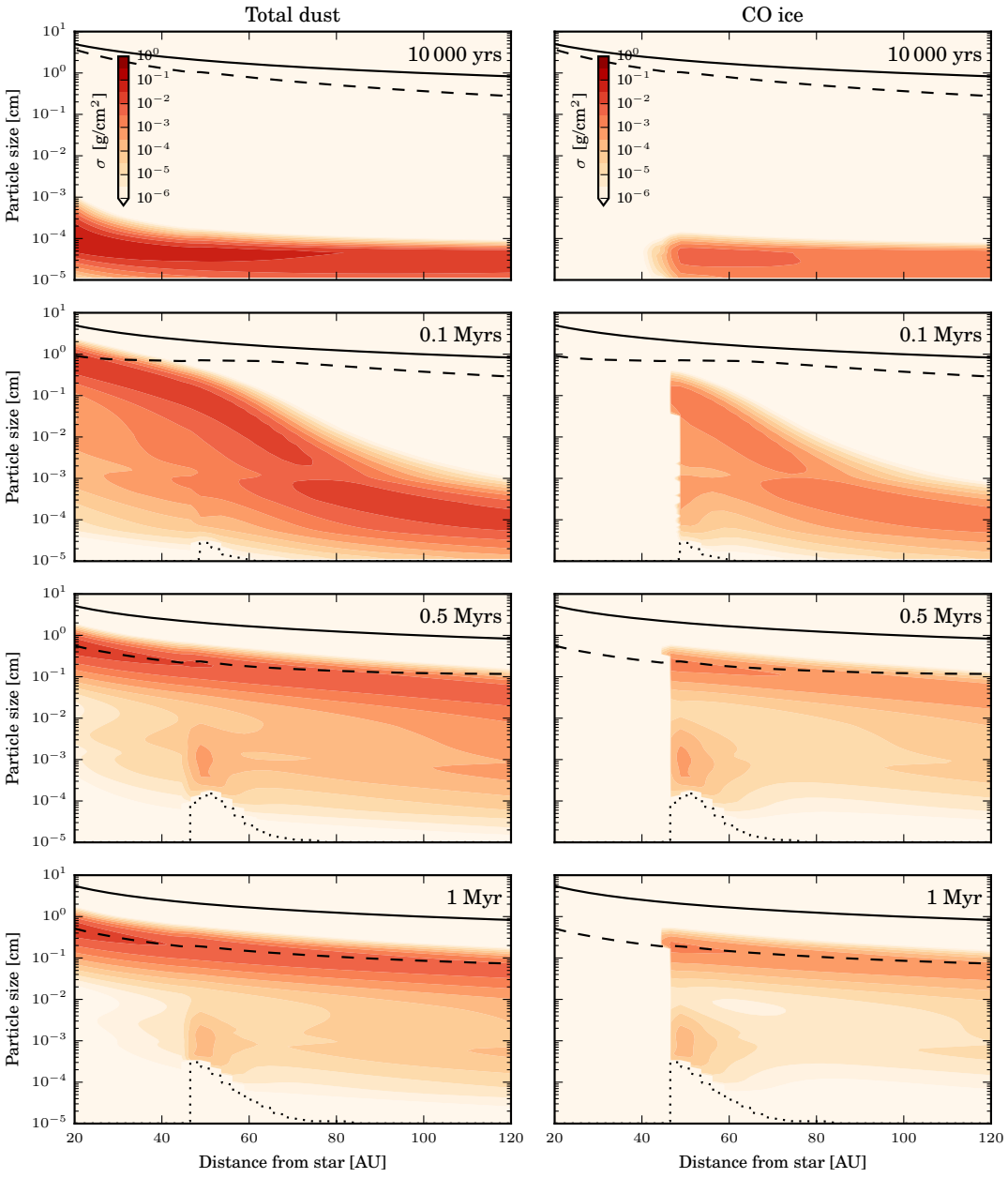

Figure 2.4: Different snapshots of our fiducial model. Shown are the different distribution functions as defined by equations (2.43) at 10 000 yrs, 100 000 yrs, 500 000 yrs, and at 1 Myr. The solid line denotes the particle sizes with Stokes number unity, The dashed line is an analytical estimation of the drift barrier. The dotted line encompasses a region outside of the ice line that is free of small particles.

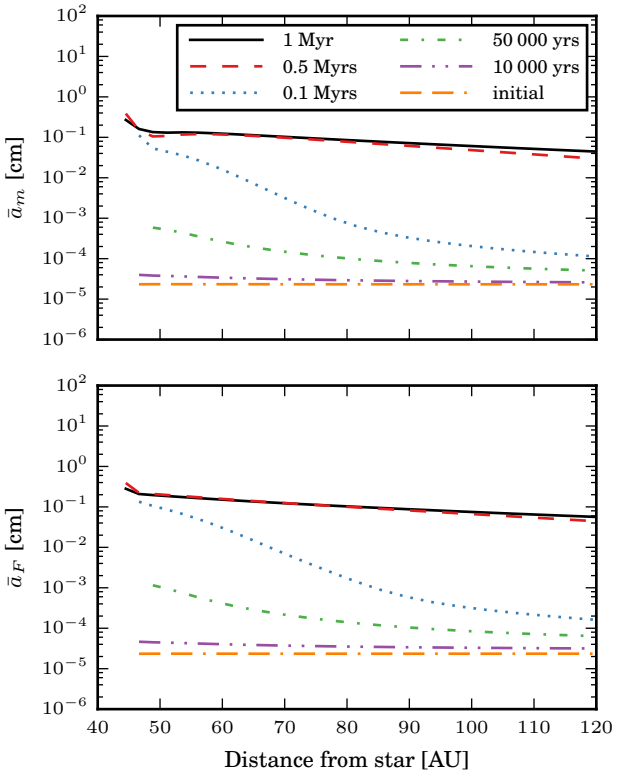

Figure 2.5: The typical particle size $\bar{a}_m$ that carries most of the ice mass, and the typical particle size $\bar{a}_F$ that transports most of the ice mass for different snapshots in our fiducial model.

to-CO ratio f_{g2CO} at different times in the simulation. We used values for f_{g2CO} of 70, 700 (fiducial model), and 7000, which correspond to CO abundances of 10^{-3}, 10^{-4}, and 10^{-5}. For guidance, the horizontal lines mark the values for the quantities one would expect outside the ice line simply from the initial conditions. The excess is defined as $\Sigma_i/\Sigma_0 - 1$, where Σ_i is the total dust surface density in the models of the different CO abundances and Σ_0 is the total dust surface density in the model without CO. The initial value of the excess outside the ice line is $f_{\mathrm{g2d}}/f_{\mathrm{g2CO}}$. The initial value of the gas-to-dust ratio is $1/f_{\mathrm{g2d}} + 1/f_{\mathrm{g2CO}}$. The ice-to-dust ratio compares the surface density of CO ice to the total dust surface density. Its initial value is $f_{\mathrm{g2d}}/(f_{\mathrm{g2d}} + f_{\mathrm{g2CO}})$.

It can be seen that the closer the CO ice line is to the star, the higher the CO abundance is. Further, the more CO there is in the system, the more saturated the evaporation/condensation is, causing the ice line to be pushed inwards. This varies the position of the CO ice line in these models from approximately 40 AU to 50 AU, initially.

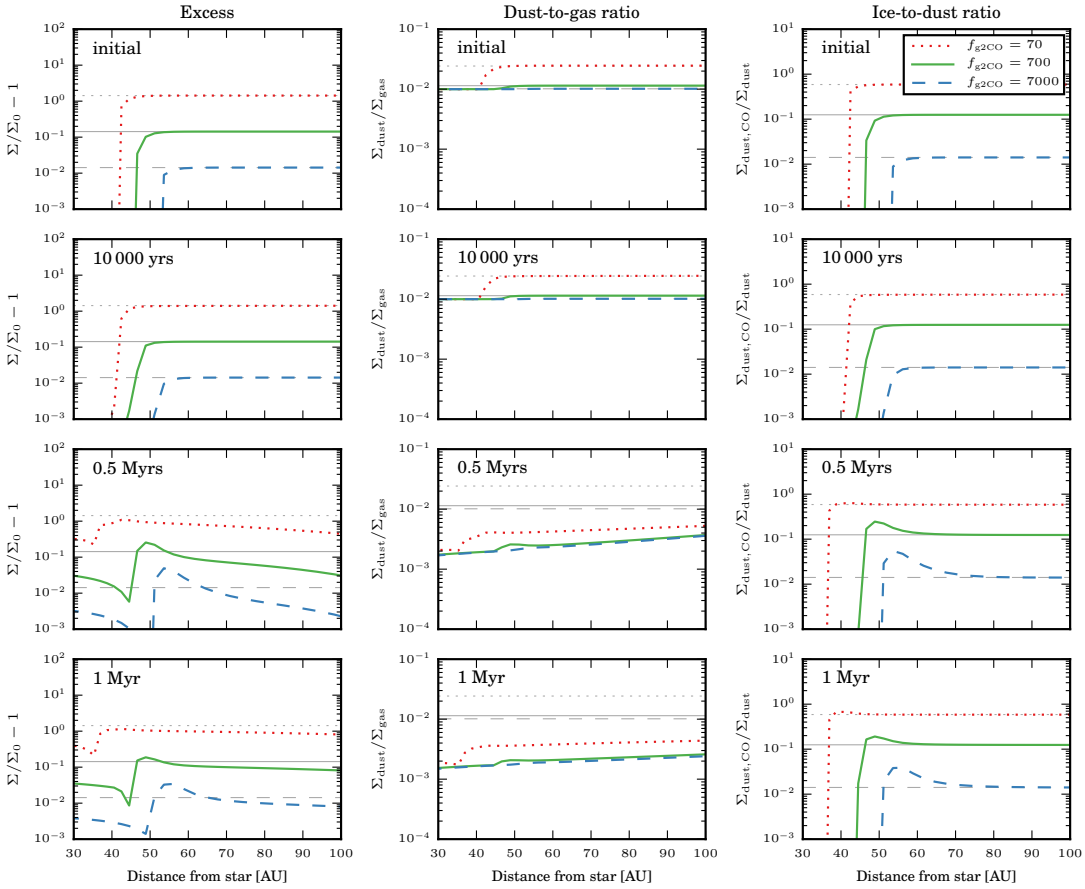

Figure 2.6: The excess of total dust surface density compared to a model without CO, the dust-to-gas ratio and the ice-to-dust ratio at different times for initial gas-to-CO ratios of 70 (dotted red line), 700 (fiducial model, solid green line) and 7000 (dashed blue line). The horizontal gray lines are the respective quantities one would expect from the initial conditions outside the ice line.

The left panels show the excess compared to a model without CO. Notably, the excess inside the ice line is nonzero in all cases, meaning the total surface density is still higher than in the comparison model without CO. Because of the larger CO-coated particles in the models with CO, and therefore the more effective drift, the dust surface density is enhanced inside the ice line. This is especially visible in the high abundance model. In some models, the excess at the ice line can be a few times larger than one would expect from the initial values. This is due to accumulation and redistribution of CO at the ice line.

In general, the dust-to-gas ratio decreases with time. The dust surface density de-

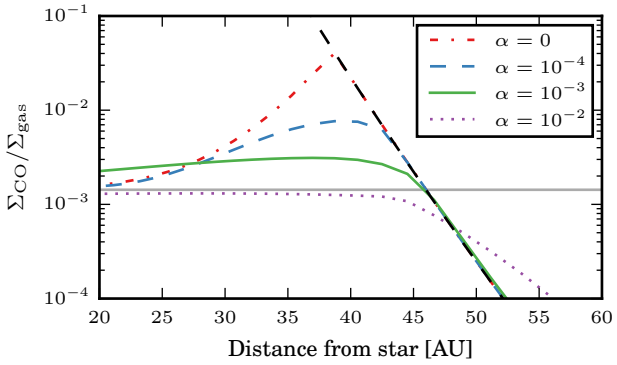

Figure 2.7: The ratio of CO gas surface density to total gas surface density after 1 Myr in the region of the ice line. Shown are the fiducial model with $\alpha = 10^{-3}$ (solid green line), a low-viscosity model with $\alpha = 10^{-4}$ (dashed blue), and a high-viscosity model with $\alpha = 10^{-2}$ (dotted purple). The ratio of $\Sigma_{CO}^{eq}/\Sigma_{gas}$ is plotted with a dashed black line. Also plotted is the case of a disk without viscous spreading (red dash-dotted line). The horizontal gray line is our input value for the CO-to-gas mass ratio.

creases while the gas density remains approximately constant over time, as discussed later. The dust-to-gas ratio decreases from inside out because the particle growth is most efficient in the inner parts of the disk, meaning the particles start to drift earlier than outside. The dust-to-gas ratio is increased at the location of the ice line. This is due to two effects: first, as the particles drift through the ice line, they shrink because of evaporation, making drift less efficient and therefore leading to a "traffic jam", and second, the backwards-diffusing and recondensing CO vapor increases the ice surface density outside the ice line.

This effect can also be seen in the ice-to-dust ratio. At 1 Myr, the ice-to-dust ratio is enhanced above the initial value even at radii larger than 70 AU depending on the model.

2.3.2 Transport of CO in the Gas Phase

CO is radially transported in the disk via three mechanisms: viscous accretion and diffusion in the gas phase and frozen-out as ice on drifting particles. As, outside of the ice line, most of the CO is frozen-out on particles, the dominant radial transport mechanism there is particle drift. Inside the ice line, on the other hand, all of the CO exists in the gas phase and is radially transported by viscous accretion and diffusion.

This means that transport of CO through the ice line from the outside into the inner part of the disk happens on drifting dust particles, while transport from the inside to

the outside takes place in the gas phase. The efficiency of viscous accretion is highly dependent on the viscosity parameter α while the drift velocity of particles depends on their size and is only indirectly related to α through the dust growth.

Particles are drifting through the ice line and deposit their CO as vapor there. The strength of α determines how rapidly this CO vapor is diffused from there. This is shown in figure 2.7 where we compared our fiducial model, with $\alpha = 10^{-3}$, with a low-viscosity model of $\alpha = 10^{-4}$ and a high-viscosity model of $\alpha = 10^{-2}$ at the time of 1 Myr. Plotted is the ratio of the CO gas surface density $\Sigma_{\rm CO}$ to the total gas surface density $\Sigma_{\rm gas}$ at the region of the ice line. Also plotted is the ratio of $\Sigma_{\rm CO}^{\rm eq}$ to $\Sigma_{\rm gas}$. The ice line is therefore defined as the position where the CO gas phase abundance approaches the level set by the equilibrium density (dashed black line). This can happen anywhere from 39 to 49 AU approximately, depending on the assumed viscosity and consequently the CO gas abundance. The lower the viscosity, the more efficient the accumulation of gas, pushing the ice line closer to the star.

Even though the temperature structure is the same for all three models, there is still a difference in the location of the ice line. The reason for this is that evaporation/condensation not only depends on the temperature but also on the partial pressure of CO, as seen in equation (2.28). The partial pressure depends on the amount of vaporized CO at a given location and on the temperature (cf. equation (2.32)). This means that, in principle, any system can be in saturation (ie., equation (2.28) equals zero) for any temperature if the density is high enough. In our fiducial model, at 1 Myr, (green solid line in figure 2.7) this happens at ~ 47 AU where the temperature is ~ 22 K.

In the beginning of the simulations, the ice lines of the different models were at the same position. As soon as the particles start to grow, they drift inwards, cross the ice line, and deposit their CO there. Depending on the efficiencies of accretion and mixing, the system can become saturated at the ice line if more CO vapor gets deposited there by drifting particles than can be transported away in the gas phase. If that is the case, then the ice line moves inwards because the particles can only evaporate when they are in a region where the system is not in saturation. Therefore, the ice line in the low-α models is closer to the star than the ice line in the fiducial model. As mentioned above, this inward motion of the ice line is entirely due to non-thermal effects, as we consider a time invariant temperature structure. Should the midplane temperature change, due to changes in disc flaring, for example, this would have a more noticeable effect on the ice line location as shown in Panić and Min (2017).

We also show, in Fig. 2.7, a model where we turned off the viscous evolution of the gas disk by not solving equation (2.7). This is equivalent to setting $\alpha = 0$. In this case, all the CO vapor remains where it is evaporated, and this moves the ice line inwards to approximately 39 AU compared to the fiducial case at 47 AU. In the region just inside the ice line, the ratio $\Sigma_{\rm CO}/\Sigma_{\rm gas}$ is largely increased compared to the initial ratio of $1/f_{\rm g2CO}$ depending on the strength of viscosity. In the fiducial model, $\Sigma_{\rm CO}/\Sigma_{\rm gas}$

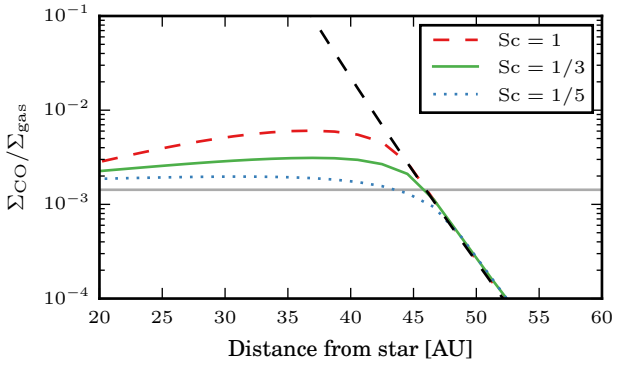

Figure 2.8: Dependency of the ratio of CO vapor surface density to total gas surface density on the Schmidt number at 1 Myr. The fiducial model is identical to the model with Sc $= 1/3$ (green solid line). The dashed black line represents the ratio of $\Sigma^{eq}_{CO}/\Sigma_{gas}$. The horizontal gray line corresponds to the initial CO-to-gas ratio.

is, in general, slightly increased in the inner part of the disk, since the transport of evaporated CO from the ice line to the inner disk is more effective here.

In the high viscosity case, the redistribution of vapor is stronger than the recondensation onto the particles. Meaning, vapor from inside the ice line becomes diffused outwards faster than it can recondense onto the particles. This can be seen as the ratio of CO vapor to total gas is decoupled from the equilibrium evaporation line. In this case, no increase of CO vapor in the inner disk can be seen.

2.3.3 The Influence of Diffusion on the Position of the Ice Line

By rewriting the equation (2.4) for viscous accretion, one can see that it consists of an advective and a diffusive term with a diffusivity $D = 3\nu$, as can be seen in equation (2.7). By introducing the Schmidt number Sc $= \nu/D$, we disentangled the advective and diffusive terms. The Schmidt number compares the strength of angular momentum transport to pure mass transport. To investigate the influence of the diffusivity on the transport of CO, we performed simulations where we kept the viscosity, as in the fiducial model, at $\alpha = 10^{-3}$, and changed the diffusivity by choosing different Schmidt numbers.

The result is shown in figure 2.8. The green models in figures 2.7 and 2.8 are the fiducial model and are therefore identical. It can be seen that the diffusivity D is relevant for distributing the CO in the gas disk; it smears out concentration gradients. With lower diffusivities (higher Schmidt numbers), the pile-up of CO gas just inside the ice line gets larger because it cannot be transported rapidly enough as it gets

deposited there. The ice line is therefore shifted slightly to the inside of the disk for models with higher Schmidt numbers.

One possibility to trap particles is to assume a pressure bump. The dust particles drift in the direction of the pressure gradient (cf. equation (2.17)). Kretke and Lin (2007) proposed such a pressure bump at ice lines because of a sharp transition of the turbulent viscosity parameter α at the ice line. In our model, we do not change α at the ice line. The pressure bumps we could create are therefore only due to evaporation of CO on inward-drifting particles, but to create such a pressure bump only by depositing CO gas is rather unrealistic since one would need to increase the CO gas surface density by a factor larger than f_{g2CO}.

Figure 2.9 shows the distribution of ice along the different particle sizes dependent on α. For high-viscosity cases, the CO ice gets distributed as far out as 90 AU for small particles. In the low-viscosity case, the CO ice region is restricted up to 60 AU. Also, the higher the viscosity, the farther out the ice line. With high α (and therefore, via the Schmidt number, also high D), CO vapor cannot be accumulated at the ice line. This prevents any saturation effect.

2.4 Discussion

The CO Surface Density and Ice Line Position

In the previous section, we showed that Σ_{CO}, the vapor density of CO, approximately follows the equilibrium vapor density $\Sigma_{\mathrm{CO}}^{\mathrm{eq}}$, as long as there is enough CO in the disk. If the evaporation/condensation timescales are shorter than the dynamical time scales of the system, the CO exactly follows the equilibrium density; if the evaporation/condensation timescales are longer than the dynamical timescales, it can decouple from the equilibrium vapor density. To first order, one can therefore approximate the CO vapor surface density in the whole disk with the equation

$$\Sigma_{\mathrm{CO}} = \min\left[\frac{1}{f_{\mathrm{g2CO}}}\Sigma_{\mathrm{gas}},\ \Sigma_{\mathrm{CO}}^{\mathrm{eq}}\right]. \tag{2.46}$$

Outside the ice line, the CO surface density is equal to $\Sigma_{\mathrm{gas}}^{\mathrm{CO}}$; inside the ice line it is approximated by using the total surface density and the initial gas-to-CO ratio. Although, one should note that in figures 2.7 and 2.8, the ratio of $\Sigma_{\mathrm{CO}}/\Sigma_{\mathrm{gas}}$ can be significantly increased just inside the ice line, depending on the values of α and Sc.

The position of the ice line R_{ice} is then defined as the point where the CO surface density joins the equilibrium density and can be approximated by equating:

$$\frac{1}{f_{\mathrm{g2CO}}}\Sigma_{\mathrm{gas}}\left(R_{\mathrm{ice}}\right) = \Sigma_{\mathrm{CO}}^{\mathrm{eq}}\left(R_{\mathrm{ice}}\right). \tag{2.47}$$

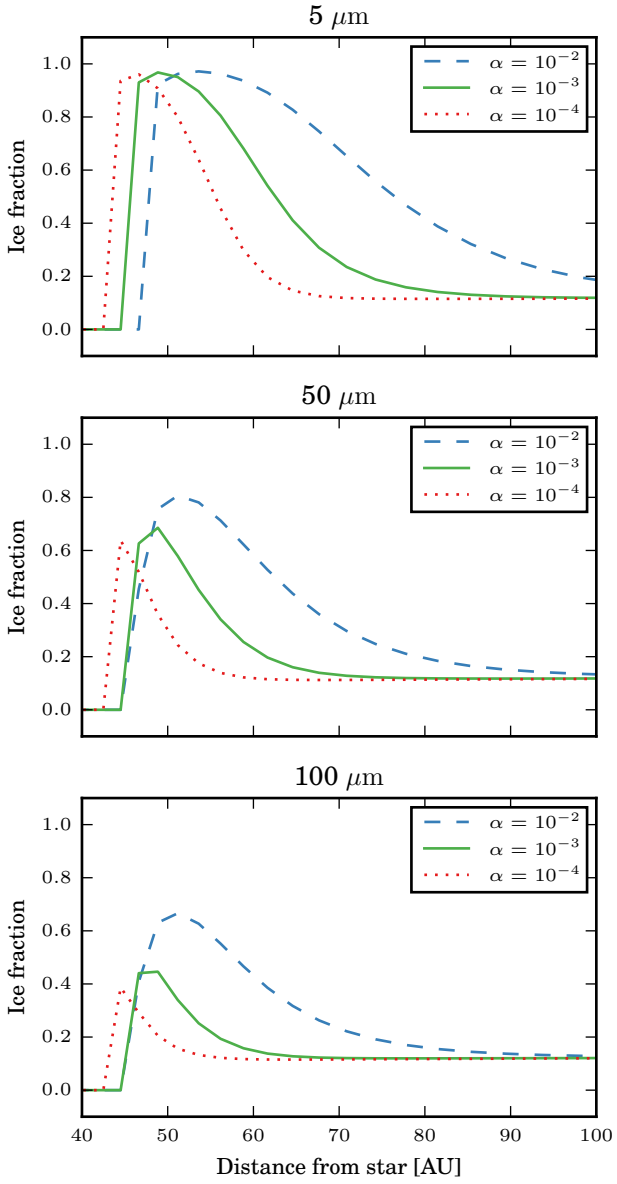

Figure 2.9: The distribution of Q according to R for different silicate core sizes a_{sil} and different values of $\alpha = 10^{-4}$ (dotted red line), $\alpha = 10^{-3}$ (fiducial, solid green line) and $\alpha = 10^{-2}$ (dashed blue line) after 1 Myr.

Piso et al. (2015) showed, by comparing the desorption time t_{des} of evaporating particles with their respective drift timescale t_{drift}, that the location of the ice line does not necessarily coincide with the location where the system gets out of saturation. When the particles drift faster than they evaporate (i.e., $t_{\mathrm{des}}/t_{\mathrm{drift}} \gg 1$), the particles drift far

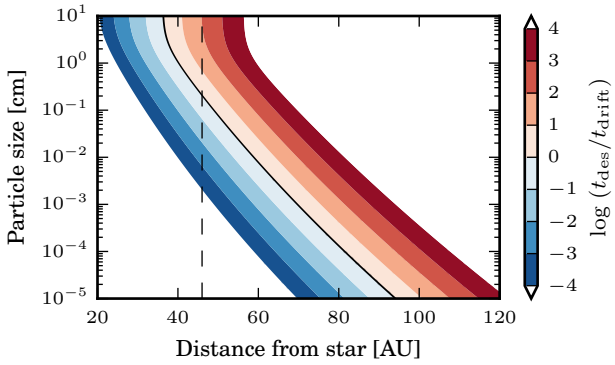

Figure 2.10: Comparing the desorption time $t_{\rm des}$ with the drift timescale $t_{\rm drist}$. If the ratio $t_{\rm des}/t_{\rm drift}$ is larger than unity, the particles can drift past the ice line before they fully evaporate their ices. The vertical dashed line is the location of the ice line in our model.

past the ice line before they evaporate their ice, leading to icy particles inside the ice line.

Figure 2.10 shows the ratio of the desorption time $t_{\rm des}$ to the drift timescale $t_{\rm drift}$ for our fiducial model. The desorption time is given by

$$t_{\rm des} = \frac{a}{\dot{a}} = \frac{a\,\rho_{\rm CO}}{m_{\rm CO}} \frac{k_{\rm B}T}{v_{\rm therm} P^{\rm eq}(T)}, \tag{2.48}$$

whereas the drift timescale is given by

$$t_{\rm drift} = \frac{R}{v_{\rm dust}}. \tag{2.49}$$

By comparing figure 2.10 with figure 2.4, one can see that the particles at the location of the ice line have a size where this 'smearing-out' begins to happen. Figure 2.11 shows the CO ice surface density after 1 Myr in our fiducial model. The ice line of the smaller particles is at approximately 47 AU, whereas the ice line for the largest particles is at approximately 45 AU.

By using equation (2.46), one has to keep in mind that the values for $\Sigma_{\rm CO}$ around the ice line and the position of the ice line itself highly depend on the transport properties of CO in the gas phase, that is, the viscosity ν and therefore the α turbulence parameter, and on the diffusivity D. If the transport mechanism of CO in the gas phase is not strong enough, that is, low α or low D, a pile-up of vaporized CO is created just inside the ice line. This brings the system into saturation even closer to the star and therefore shifts the ice line closer to the star. This can lead to differences in the position of the ice line of up to 10 AU and a change in temperature at the ice line from 21 K to 23 K. In an evolving disk, where the temperature profile is not fixed, the change in the position

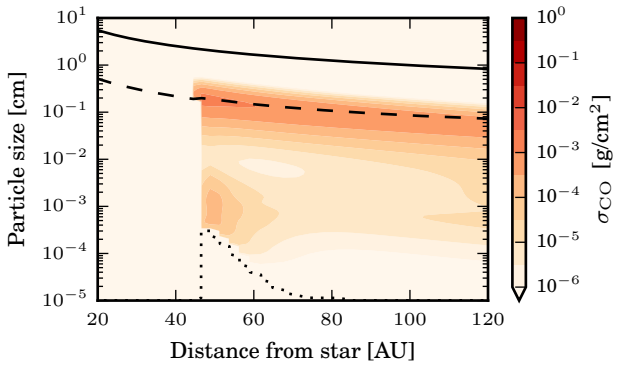

Figure 2.11: CO ice surface density in our fiducial model after 1 Myr. The largest particles are just large enough such that their drift timescale is smaller than their desorption timescale leading to a 'smearing-out' of the ice line. The solid line denotes the particle sizes with Stokes number of unity. The dashed line is the drift barrier. The dotted line encompasses an empty region outside the ice line.

of the ice line can be even stronger due to changes in the midplane temperature (e.g., Panić and Min, 2017). Also, in the high viscosity case, redistribution of CO can be strong enough for the vapor to be decoupled from the equilibrium vapor pressure.

By looking at figures 2.7 and 2.8, one can see that the CO vapor abundance in the inner part of the disk is significantly increased over to the canonical ISM value. This was also predicted by Cuzzi and Zahnle (2004, Regimes 1 and 2 therein). However, we cannot reproduce a depleted inner nebula as in Stevenson and Lunine (1988) and Cuzzi and Zahnle (2004, Regime 3) because we do not have any sink terms such as immobile planetesimals outside the ice line that can remove the vapor from the disk. Our particles on which the CO vapor recondenses outside the ice line are still mobile and drift inwards through the ice line replenishing the CO vapor there. Only in the high-viscosity case does the inner disk become slightly depleted in CO vapor around the ice line due to the turbulent diffusion being effective enough to push the gas farther out against recondensation.

Particle Growth at the Ice Line and Detectability

We do not see an enhanced particle growth just outside the ice line; instead we see a depletion in surface density of dust inside the ice line. This depletion is entirely due to loss of CO ice mantles, thereby making the dust particles smaller and less massive. The particle surface density is dominated by particles close to their local drift barrier. CO vapor, that previously diffused backwards from inside the ice line and then recondensed on those particles outside the ice line, only increase their size and

Stokes number, making them drift even more rapidly though the ice line. This drift barrier limits the sizes of the particles in our models to less than one centimeter at the CO ice line.

The depression in total dust surface density seen in figure 2.2 is therefore related to the amount of CO in the system. The radial jump in the total dust surface density is approximately given by the ratio $\frac{f_{\mathrm{g2d}}}{f_{\mathrm{g2CO}}}$. If we assume that the loss of the CO ice mantle at the CO ice line does not cause any differences to the optical properties of the dust in the mm-wavelength regime, then the difference in the intensity by thermal continuum emission of the dust S_ν is dominated by the difference in surface density of the dust. Using the optically thin approximation

$$\frac{S_{\nu,\,\mathrm{in}}}{S_{\nu,\,\mathrm{out}}} = \frac{\Sigma_{\mathrm{dust,\,in}}}{\Sigma_{\mathrm{dust,\,out}}} \frac{B_\nu(T_{\mathrm{in}})}{B_\nu(T_{\mathrm{out}})}, \tag{2.50}$$

where $B_\nu(T)$ is the Planck function and *in*/*out* refers to locations shortly inside/outside the ice line. The dust densities are given by

$$\begin{aligned} \Sigma_{\mathrm{dust,\,in}} &= \Sigma_{\mathrm{dust}}\left(R_{\mathrm{in}}\right)\left(1 - \frac{f_{\mathrm{g2d}}}{f_{\mathrm{g2CO}}}\right) \\ \Sigma_{\mathrm{dust,\,out}} &= \Sigma_{\mathrm{dust}}\left(R_{\mathrm{out}}\right) = \Sigma_{\mathrm{dust}}\left(R_{\mathrm{in}}\right)\left(\frac{R_{\mathrm{out}}}{R_{\mathrm{in}}}\right)^{p}, \end{aligned} \tag{2.51}$$

by assuming a simple power law for the dust surface density $\Sigma_{\mathrm{dust}}\left(R\right) = \Sigma_0\left(\frac{R}{1\ \mathrm{AU}}\right)^{p}$. This leads to

$$\frac{S_{\nu,\,\mathrm{in}}}{S_{\nu,\,\mathrm{out}}} = \left(1 - \frac{f_{\mathrm{g2d}}}{f_{\mathrm{g2CO}}}\right)\left(\frac{R_{\mathrm{in}}}{R_{\mathrm{out}}}\right)^{p} \frac{B_\nu(T_{\mathrm{in}})}{B_\nu(T_{\mathrm{out}})} \simeq 0.86\left(\frac{R_{\mathrm{in}}}{R_{\mathrm{out}}}\right)^{p}, \tag{2.52}$$

by assuming a canonical ISM value of $f_{\mathrm{g2d}}/f_{\mathrm{g2CO}} = 1/7$ (see e.g., Yamamoto et al., 1983) and $B_\nu(T_{\mathrm{in}})/B_\nu(T_{\mathrm{out}}) \simeq 1$. To detect the effect of the CO evaporation and to quantify $f_{\mathrm{g2d}}/f_{\mathrm{g2CO}}$ (under the assumption that no other process causes a bump at the ice line), it is clear that one needs to constrain p in the region beyond the ice line and measure S_ν at R_{ice} to S/N much greater than 7.

Influence of the Particle Size on the Fragmentation Velocity

Okuzumi et al. (2016) showed that a change in the fragmentation velocity due to sintered aggregates in the proximity of ice lines can produce rings in disks, as observed for example in the disk around HL Tau. Evaporation preferentially happens on convex surfaces, while condensation preferentially happens on concave surfaces. Close to the ice line, evaporation starts to happen on the convex surface of a monomer, while simultaneously, condensation can happen on the concave contact point ("neck") of two connected monomers (Sirono, 2011b). This effect stiffens the neck making it harder

for the monomers to roll around this contact point. Aggregates can absorb the impact energy of collisions by restructuring via rolling (Dominik and Tielens, 1997). Sintering reduces the possibility of rolling leading to a breakup of the monomer connections and therefore a lower fragmentation velocity.

In contrast to that, the critical breaking velocity necessary to break up the connection of two monomers is inversely proportional to the monomer size $v_{\text{crit}} \propto a_0^{-5/6}$ (cf. Dominik and Tielens, 1997) leading to lower fragmentation velocities for aggregates with larger monomer sizes. We showed in figure 2.3 that our particles with a silicate core of 0.1 μm (the monomers) have an ice fraction of $Q > 0.999$ in the region outside the ice line. The monomer size in that region is therefore increased by a factor of at least 10 and the fragmentation velocity decreased by a factor of approximately 7. This could lead to enhanced fragmentation just outside ice lines and is discussed in chapter 3.

Possible Improvements of the Model

1. Our model is one-dimensional and we only use surface densities in our calculations. This leads to errors in Σ_{CO} in our treatment of the evaporation/condensation described in section 2.2.5. We underestimate Σ_{CO} since we are neglecting the CO in the hot surface layers of the disk. However, since the disk's atmosphere is small compared to its scale height, and its density is significantly smaller than the midplane density, this should not be a large effect.

2. We do not take into account the vertical movement of dust particles. This movement could also influence the vertical distribution of CO gas. One could imagine that the CO gas condenses on small dust particles in the surface of the disk. These particles then sink more easily towards the midplane and remove CO vapor from the disk's atmosphere. Or, vice versa, small CO-coated dust particles are pushed through the atmospheric ice line due to turbulence, depositing their CO as gas in the disk's surface. This is a topic of further investigation.

3. We also do not take into account the vertical diffusion of CO vapor and how this affects the local CO vapor pressure in the midplane. As particles grow, they settle to the midplane. When they drift inwards through the ice line, one would think that most of the CO vapor is set free close to the midplane and is not instantaneously in thermal equilibrium as we assume in our model.

4. In our model we treat the particles as compact spheres, but Kataoka et al. (2013) showed that, through fractal growth, the particles can potentially overcome the drift barrier. The reason for this is that fluffy aggregates have larger cross-sections than compact aggregates of the same mass. This decreases the growth timescales of the particles, making the growth of the particles more efficient and potentially making it possible to overcome the drift barrier.

5. Treating particles as compact spheres and not as fluffy aggregates could lead to an artificial 'non-fragmentation' by evaporation, since we combine the silicate mass of the particle in one particle core after evaporation of the CO instead of creating many small particles as Aumatell and Wurm (2011) suggested.

6. Including fragmentation and looking at the inner disk can potentially change some results. In general, the particle size in the inner parts of the nebula is fragmentation limited instead of drift limited, as in the outer disk. Therefore, the particle dynamics and distributions change, which can have effects on the various volatile redistribution mechanisms discussed in this paper.

2.5 Conclusion

We developed a model for dust growth with a volatile species including particle drift and diffusion, evaporation and condensation of the volatiles, and viscous evolution of the gas. We do not find any enhanced particle growth by recondensation just outside the ice line, since the particles there are already close to their drift barrier. Due to particle drift through the ice line, evaporation, diffusion and recondensation on particles outside the ice line, we find a dust surface density enhancement at the ice line that could be observable at the CO ice line. The vapor that gets deposited at the ice line by inwards-drifting particles can push the ice line closer to the star. If the efficiency of redistribution of vapor in the disk is low, then the vapor accumulates at the ice line, bringing the system into saturation and therefore preventing evaporation. The location of the ice line itself does depend on disk parameters such as temperature, volatile abundance, viscosity, or diffusivity. Furthermore, different particle sizes can have, in general, different locations at which they fully evaporate their volatile species. The increase in monomer size just outside the ice line could lead to fragmentation, exactly as proposed for sintering.

Our model is not restricted to CO. By using the analogous parameters for water ice, we can transfer the simulation to the water ice line in the inner disk. Here, one has to take into account that the collisional properties of water-ice-coated particles and purely silicate particles differ tremendously (e.g., Blum and Wurm, 2008, Güttler et al., 2010). For ice-free particles, fragmentation plays an important role and has to be taken into account for particles crossing the ice line. Furthermore, the water ice line is at locations in the disk where viscous heating is important and has to be taken into account. The question of the location and distribution of H_2O has an important role in astrophysics and planetary sciences. Whether the Earth formed dry, that is, inside the water ice line, or in a region outside the ice line remains to be determined. If the Earth formed dry, the origin of the Earth's water is unclear. If it formed wet, the relatively small amount of water observed on Earth is curious. By transforming our model to water ice and implementing fragmentation, we will try to come closer to elucidating these subjects in future work.

3

The Influence of Ice Lines on Dust Growth in Protoplanetary Disks

3.1 Motivation

Recent high-resolution observations of protoplanetary disk at millimeter wavelengths revealed ringed substructures. The otherwise smooth disks of HL Tauri (ALMA Partnership et al., 2015), TW Hydrae (Andrews et al., 2016, Tsukagoshi et al., 2016), and HD 163296 (Isella et al., 2016) are interrupted by axis-symmetric gaps, that show deficits in dust emission. Figure 3.1 shows exemplarily millimeter observations of TW Hydrae taken by Andrews et al. (2016). Interestingly, the aforementioned disks cover a relatively large range of ages with HL Tauri being $\lesssim$ 1–2 Myrs (Briceño et al., 2002), HD 163296 being 5 Myrs (Natta et al., 2004), and TW Hydrae being about 10 Myrs old (Weinberger et al., 2013). This suggests that the mechanisms that is forming the gaps is universal for a broad range of disk ages.

Several mechanisms of gap formation have been proposed so far, that can be categorized as either dynamical, magnetic, or chemical in their nature. The most prominent model is the dynamical creations of gaps in the gas disk by existing planets. Planets can open gaps via tidal interactions with the gas (Lin and Papaloizou, 1986, Kley and Nelson, 2012). Subsequently, particles react to the gas pressure gradients induced by the planets and are being pushed out of the gas gaps and can even be trapped at the gap edges (Paardekooper and Mellema, 2006, Zhu et al., 2014). Duffell and MacFadyen (2013) and Zhu et al. (2013) showed that even low-mass planets of only a few Earth masses could potentially open gaps in protoplanetary disks. Given the young age of HL Tauri, this suggests that planets can be formed already in the very early stages of the disk's evolution, under the assumption that these gaps in HL Tauri are indeed caused by planets. Furthermore, the three aforementioned disks look remarkably similar in continuum emission images, even though their ages differ quite significantly.

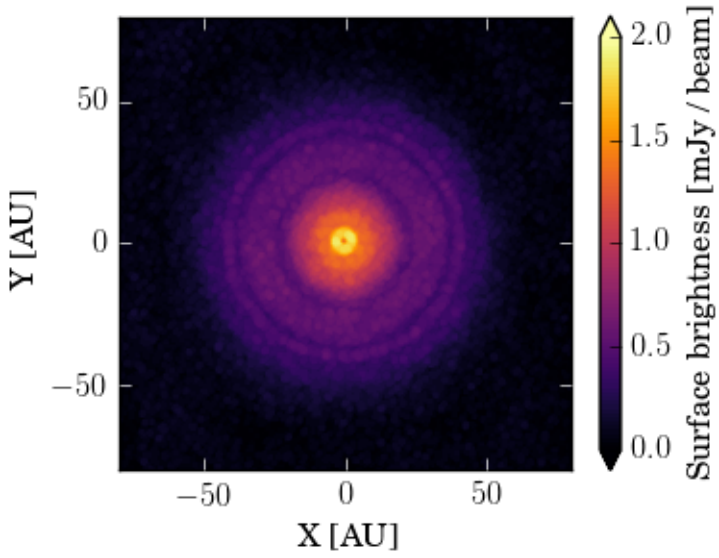

Figure 3.1: Observation of TW Hydrae at a wavelength of $\lambda = 870\,\mu$m taken by Andrews et al. (2016).

This would indicate, that after a rapid formation of planets not much changes for several million years.

Magnetized disks are subject to the magnetorotational instability (Balbus and Hawley, 1991), which can build up zonal flows in the disk (Johansen et al., 2009). These zonal flows have been shown to collect dust (Dittrich et al., 2013), that might be seen as rings in millimeter observations. It is, however, unclear if these local shearing box simulations can be translated into global simulations of protoplanetary disks.

The magnetorotational instability (MRI) is thought to be one of the main sources of viscosity in protoplanetary disks and therefore responsible for accretion in these disk, since the viscosity is providing a mechanism for transporting angular momentum outwards. MRI can only work if the ionization fractions in the disk are large enough. Therefore, in regions of low ionization – so-called *dead zones* – accretion is suppressed. Therefore, at the outer edge of dead zones, there is a transition from strong accretion to low accretion. This creates pressure bumps at the outer edge of dead zones, that can trap dust particles. Pinilla et al. (2016) showed, that this effect can build up material, that can be seen as rings in observations of dust.

Zhang et al. (2015) interpreted the gaps in HL Tauri as ice lines. Ros and Johansen (2013) showed that recondensation of water vapor on ice particles outside the water ice line can be a significant mechanism for dust growth. In that case, the optical depth

in a region outside the ice line would be decreased, because of the presence of larger particles. This can be seen as gaps in observations, with the ice line being located at the inner edge of the gap. However, Ros and Johansen (2013) did not include any dust growth and fragmentation in their model. Water vapor can therefore only recondense outside the ice line on the large ice particles that are already there. In chapter 2 we could show, that – by using a full dust growth model with evaporation and condensation – no discontinuity in the maximum particle sizes can be observed across ice lines.

Okuzumi et al. (2016) investigated the effect of sintering on dust growth in protoplanetary disks. The evaporation rate, in general, depends on the curvature of the surface that gets evaporated, with convex surfaces having higher evaporation rates than concave surfaces. It is therefore possible that at a given temperature the convex particles within a dust aggregate can evaporate while at the same time the vapor can recondense on the concave connection points between the particles of the aggregate (Sirono, 2011a). This process, that stiffens the connections between two particles, is called *sintering*. In a collision, sintered particles cannot dissipate the impact energy by rolling of their monomers in the aggregate. These stiffened connections between monomers therefore rather break than roll. This leads to lower fragmentation velocities in regions where sintering is important.

Okuzumi et al. (2016) showed, that sintering is important in regions shortly outside of ice lines, where the temperature is just high enough such that convex surfaces already evaporate while vapor can still recondense on concave surfaces. This leads to decreased fragmentation velocities in regions just outside of ice lines, and thus, to smaller particle sizes. Since smaller particles drift less efficiently, this causes traffic jams and accumulations of dust, which can be seen as bright rings in continuum observations of dust in protoplanetary disks.

We showed in chapter 2 that ice lines can have a significant effect on the transport of volatiles in protoplanetary disks. Outside of ice lines, where all the vapor is frozen out as ice, the main transport mechanism of the volatile species is by drift on dust particles. Inside of ice lines, the volatile exists in its vapor form and can be advected and diffused with the gas. The vapor can even diffuse backwards through the ice line and can recondense on the particles there. The vapor will mostly condense on the smallest particles, since they contribute the most to the total surface area. Thus, significantly increasing the particle sizes of those small particles.

So far, we did not include fragmentation. The particle size were therefore solely limited by radial drift. The aim of this work is therefore to investigate the influence of fragmentation on the results obtained in chapter 2. Furthermore, we want to find out, if the increase in monomer size is strong enough to have an effect on the fragmentation velocity, which in general depends on the size of the monomers in dust aggregates (Dominik and Tielens, 1997). This, in turn, can have an effect on the maximum particle sizes and could lead to the formation of rings as in Okuzumi et al. (2016).

In section 3.2 we will introduce the numerical methods used in this work. In section 3.3 we present our results, which are discussed in section 3.4. We conclude this chapter in section 3.5.

3.2 Numerical Method

In chapter 2, we investigated the influence of ice lines on the transport of volatiles in protoplanetary disks. Outside of ice lines, the volatile is frozen out as ice on dust particles. The main transport mechanism of volatile species is therefore by drifting dust particles. When dust particles drift through the ice line, they lose the volatile by evaporation. This newly created vapor can then diffuse backwards through the ice line and can recondense on the particles there. We showed in chapter2, that the vapor mostly recondenses on the smallest particles, increasing their size.

Dominik and Tielens (1997) showed, that the fragmentation velocity is inversely proportional to the monomer size, the smallest particles in the disk. To investigate the influence of this effect on dust in protoplanetary disk, we have to include fragmentation into our dust coagulation model. This will change the particle size distribution. It will reduce the maximum particle size and will increase the amount of smaller particles, that are created in fragmenting collisions.

This, in turn, has an effect on the efficiency of particle drift, since the drift velocity depends on the Stokes number of the particles and therefore on the particle size.

3.2.1 Fragmentation Model

We did not include fragmentation in chapter 2. To add fragmentation in this work we have to modify the Smoluchowski equation. The Smoluchowski equation with fragmentation reads as follows assuming that the particle distribution $f(m)$ has only one parameter, the particle mass m:

$$\frac{\partial}{\partial t} f(m) = \int_0^\infty \int_0^\infty f(m') f(m'') M(m;\, m', m'')\, \mathrm{d}m' \mathrm{d}m'', \tag{3.1}$$

where the collision kernel $M(m,\, m', m'')$ is given by

$$\begin{aligned} M(m;\, m', m'') \;&= \frac{1}{2} K(m', m'')\, \delta(m' + m'' - m) \\ &\quad - K(m', m'')\, \delta(m'' - m) \\ &\quad + \frac{1}{2} L(m', m'')\, S(m;\, m', m'') \\ &\quad - L(m', m'')\, \delta(m'' - m)\,. \end{aligned} \tag{3.2}$$

K and L are the coagulation and fragmentation kernels given by

$$K\left(m,m'\right) = \Delta v\left(m,m'\right)\sigma_{\text{geo}}\left(m,m'\right)p_{\text{c}} \tag{3.3}$$
$$L\left(m,m'\right) = \Delta v\left(m,m'\right)\sigma_{\text{geo}}\left(m,m'\right)p_{\text{f}}, \tag{3.4}$$

where $\Delta v\left(m,m'\right)$ is the relative velocity of particles with masses m and m', $\sigma_{\text{geo}}\left(m,m'\right) = \pi\left(a+a'\right)^2$ the geometrical cross section, and p_{c} and p_{f} the probabilities of sticking and fragmenting. If $p_{\text{c}} = 1$ and $p_{\text{f}} = 0$, equation (3.2) reduces to the fragmentation-free Smoluchowski equation presented in chapter 2. For the fragmentation probability we use the following prescription

$$p_{\text{f}} = \begin{cases} \frac{1}{2}\exp\left[\frac{\Delta v - v_{\text{frag}}}{\delta v}\right] & \text{if } \Delta v < v_{\text{frag}} \\ 1 - \frac{1}{2}\exp\left[\frac{v_{\text{frag}} - \Delta v}{\delta v}\right] & \text{else} \end{cases} \tag{3.5}$$

to allow for a smooth transition between the coagulation and fragmentation regimes. v_{frag} is the fragmentation velocity and $\delta v = 0.5\,\frac{\text{cm}}{\text{s}}$. The coagulation probability is then given by $p_{\text{c}} = 1 - p_{\text{f}}$. We do not include bouncing, for which $p_{\text{c}} = p_{\text{f}} = 0$ would hold.

The source function $S\left(m;\ m',m''\right)$ in equation (3.2) is the distribution function of fragments created in a collision of particles with masses m' and m'', which is commonly described by a power law

$$S\left(m;\ m',m''\right)\mathrm{d}m \propto m^{-\xi}\mathrm{d}m. \tag{3.6}$$

The parameter ξ can be determined either experimentally (Blum and Münch, 1993) or theoretically (Ormel et al., 2009). We adopt here the value 1.83 chosen by Birnstiel et al. (2009). $S\left(m;\ m',m''\right)$ is normalized, such that a total mass of fragments $m_{\text{frag}}\left(m',m''\right)$ gets distributed.

We distinguish between full fragmentation and cratering. In cases where the masses m' and m'' of the two colliding particles differ by more than one order of magnitude it is unrealistic that both particles fragment completely. Here we assume that the smaller particle fragments completely and will excavate some mass from the larger particle. This process is called cratering. The resulting fragment mass is then $m_{\text{frag}} = (1+\chi)m_{\text{small}}$, where m_{small} is the mass of the smaller particle in the collision. χ is the mass in units of m_{small} that gets excavated from the larger particle. We use $\chi = 1$ in this work. If the masses of both colliding particles differ by less than one order of magnitude, we assume that both particles fragments completely. The fragment mass is then $m_{\text{frag}} = m' + m''$.

To account for ices, we have to assume a particle distribution $f\left(m,Q\right)$ with two parameters m and Q. As in chapter 2, we use the moments method introduced by Okuzumi

et al. (2009). Instead of integrating the full distribution $f(m, Q)$, we only integrate the first two moments of the distribution

$$n(m) = \int_{-\infty}^{\infty} f(m, Q)\, \mathrm{d}Q \tag{3.7}$$

$$\overline{Q}(m) = \frac{1}{n(m)} \int_{-\infty}^{\infty} Q f(m, Q)\, \mathrm{d}Q. \tag{3.8}$$

We also assume that the distribution $f(m, Q) = n(m)\,\overline{Q}(m)$ is extremly narrow in Q. In that way, we can formulate two one-dimensional Smoluchowski equations for $n(m)$ and $n\overline{Q}(m) = n(m)\,\overline{Q}(m)$, that can be solved significantly faster than one two-dimensional equation

$$\begin{aligned}\frac{\partial}{\partial t} n(m) =& \frac{1}{2} \int_0^{\infty} n(m')\, n(m - m')\, \overline{K}_Q(m', m - m')\, \mathrm{d}m' \\ & - n(m) \int_0^{\infty} n(m')\, \overline{K}_Q(m, m')\, \mathrm{d}m' \\ & + \frac{1}{2} \int_0^{\infty} \int_0^{\infty} n(m')\, n(m'')\, \overline{LS}_Q(m;\, m', m'')\, \mathrm{d}m' \mathrm{d}m'' \\ & - n(m) \int_0^{\infty} n(m')\, \overline{L}_Q(m', m - m')\, \mathrm{d}m'\end{aligned} \tag{3.9}$$

$$\begin{aligned}\frac{\partial}{\partial t} n\overline{Q}(m) =& \frac{1}{2} \int_0^{\infty} n(m')\, n(m - m')\, \overline{KQ^{\mathrm{new}}}_Q(m', m - m')\, \mathrm{d}m' \\ & - n(m) \int_0^{\infty} n(m')\, \overline{KQ}_Q(m, m')\, \mathrm{d}m' \\ & + \frac{1}{2} \int_0^{\infty} \int_0^{\infty} n(m')\, n(m'')\, \overline{LSQ^{\mathrm{frag}}}_Q(m;\, m', m'')\, \mathrm{d}m' \mathrm{d}m'' \\ & - n(m) \int_0^{\infty} n(m')\, \overline{LQ}_Q(m', m - m')\, \mathrm{d}m'.\end{aligned} \tag{3.10}$$

Here we already applied the narrow-Q assumption. The new quantities are the Q-averages of their respective counterparts in equation 3.2

$$\overline{K}_Q(m,m') = K\left(m,\overline{Q}(m),m',\overline{Q}(m')\right) \tag{3.11}$$

$$\overline{KQ}_Q(m,m') = \overline{K}_Q(m,m')\,\overline{Q}(m) \tag{3.12}$$

$$\overline{KQ^{\text{new}}}_Q(m,m') = \overline{K}_Q(m,m')\,Q^{\text{new}}\left(m,\overline{Q}(m),m',\overline{Q}(m')\right) \tag{3.13}$$

$$\overline{L}_Q(m,m') = L\left(m,\overline{Q}(m),m',\overline{Q}(m')\right) \tag{3.14}$$

$$\overline{LQ}_Q(m,m') = \overline{L}_Q(m,m')\,\overline{Q}(m) \tag{3.15}$$

$$\begin{aligned}\overline{LS}_Q(m;\,m',m'') = {}& \overline{L}_Q(m,m')\times \\ & \times S\left(m;\,m',\overline{Q}(m'),m'',\overline{Q}(m'')\right)\end{aligned} \tag{3.16}$$

$$\begin{aligned}\overline{LSQ^{\text{frag}}}_Q(m;\,m',m'') = {}& \overline{LS}_Q(m;\,m',m'')\times \\ & \times Q^{\text{frag}}\left(m;\,m',\overline{Q}(m'),m'',\overline{Q}(m'')\right).\end{aligned} \tag{3.17}$$

In these definitions $Q^{\text{new}}(m,Q,m',Q')$ is the Q value the new particle has after a sticking collision of two particles with masses m and m', and parameters Q and Q'. Likewise, $Q^{\text{frag}}(m;\,m',Q',m'',Q'')$ is the Q-distribution function of the fragments that were produced in a collision of two particles with m', m'', Q', and Q''.

As in chapter 2, we assume that our particles consist of a core and an ice mantle. Then we identify Q as the ice fraction of a particle with core mass m. The total mass of a particle is then given by

$$m_{\text{tot}} = \frac{m}{1-Q} \tag{3.18}$$

and the ice mass is given by

$$m_{\text{ice}} = m_{\text{tot}}Q = \frac{mQ}{1-Q}. \tag{3.19}$$

The new ice fraction of a particle resulting from a sticking collision of two particles is given by

$$Q^{\text{new}}(m,Q,m',Q') = \frac{(1-Q')\,Qm + (1-Q)\,Q'm'}{(1-Q')\,m + (1-Q)\,m'}. \tag{3.20}$$

In fragmenting collisions we assume that all fragments have the same ice fraction $Q^{\text{frag}}(m;\,m',Q',m'',Q'') = Q^{\text{frag}}(m',Q',m'',Q'')$. In equal size collisions, when both collision partners fragment completely, the ice fraction of the fragments $Q^{\text{frag}} = Q^{\text{new}}$ is the average ice fraction of both particles. In eroding collisions, when a small particle with mass m_{small} and ice fraction Q_{small} collides with a large particle with mass m_{big} and ice fraction Q_{big}, the resulting ice fraction of the fragments is given by

$$\begin{aligned}Q^{\text{frag}}\left(m',Q',m'',Q''\right) &= \frac{\chi Q_{\text{big}}\left(1-Q_{\text{small}}\right)+Q_{\text{small}}\left(1-Q_{\text{big}}\right)}{\chi\left(1-Q_{\text{small}}\right)+1-Q_{\text{big}}} \\ &= \frac{Q_{\text{big}}\left(1-Q_{\text{small}}\right)+Q_{\text{small}}\left(1-Q_{\text{big}}\right)}{2-Q_{\text{small}}-Q_{\text{big}}}\end{aligned} \tag{3.21}$$

which does not depend on the particle masses, since χ is given in units of m_{small}. In the last step we already used $\chi = 1$.

3.2.2 Radiative Transfer

To perform radiative transfer calculations of our dust simulations we use RADMC-3D (Dullemond et al., 2016). We split our dust surface density distribution into 28 size bins between 0.1 μm and 1 m, leading to four size bins per decade. These 28 surface densities $\Sigma_{\text{dust},i}$ are then vertically distributed with a Gaussian to get spatial densities according

$$\rho_{\text{dust},i}\left(\vec{R}, z\right) = \frac{\Sigma_{\text{dust},i}\left(\vec{R}\right)}{\sqrt{2\pi}h_i} \exp\left[-\frac{z^2}{2h_i^2}\right], \tag{3.22}$$

with the dust scale height given by Birnstiel et al. (2010)

$$h_i = H \cdot \min\left(1, \sqrt{\frac{\alpha}{\min\left(\text{St}_i, \frac{1}{2}\right)\left(1 + \text{St}_i^2\right)}}\right). \tag{3.23}$$

Here H is the disk's pressure scale height, St_i the particle's Stokes number, and α the Shakura-Sunyaev viscosity parameter.

We calculate the scattering and absorption opacities by using Mie theory and the BH-MIE code of Bohren and Huffman (1983) assuming the dust particles to be spherical. We use the optical constants taken from Dorschner et al. (1995) assuming the particles consist of pure pyroxene ($Mg_{0.7}Fe_{0.3}SiO_3$). We do not change the opacities across the ice line due to simplicity and lack of optical constants for CO.

Our radiative transfer model is set up in spherical coordinates $(R,\ \varphi,\ \theta)$ with $N_R = 128$, $N_\varphi = 64$, and $N_\theta = 64$ grid points.

3.2.3 Fiducial Model Parameters

As in chapter 2, we simulate the disk evolution and dust coagulation with one additional volatiles species, carbon monoxide (CO). The initial disk profile in our fiducial model is given by

$$\Sigma_{\text{gas}}(R) = \Sigma_0 \left(\frac{R}{R_c}\right)^{-p} \exp\left[-\left(\frac{R}{R_c}\right)^{2-p}\right]. \tag{3.24}$$

The temperature profile is kept constant throughout the simulation at

$$T(R) = T_0 \left(\frac{R}{1\,\text{AU}}\right)^{-q}. \tag{3.25}$$

Table 3.1: The fiducial model parameters.

Parameter	Symbol	Value	Unit
Initial surface density at R_c	Σ_0	11	g/cm^2
Critical Radius	R_c	115	AU
Power law surface density	p	1	–
Temperature at 1 AU	T_0	150	K
Power law temperature	q	1/2	–
Viscosity parameter	α	10^{-3}	–
Stellar mass	M_{star}	2.3	$M_\odot$
Effective stellar temperature	T_{eff}	9300	K
Gas-to-dust ratio	f_{g2d}	100	–
CO abundance	[CO]	10^{-4}	–
Silicate bulk denisty	ρ_{sil}	1.2	g/cm^3
CO bulk denisty	ρ_{CO}	1.2	g/cm^3
Fragmentation velocity	v_{frag}	5.0	m/s

Both gas species Σ_{H_2} and Σ_{CO} are independently advected as in chapter 2. Our particle size grid has about 150 grid points between 0.1 μm and 1 m. Initially the particles are distributed according the MRN distribution Mathis et al. (1977) with an upper cut-off at 1 μm. The dust particles are advected as in chapter 2, but for coagulation and fragmentation we solve now equations (3.9) and (3.10).

Pure silicate material has a fragmentation velocity of about 1 m/s (Poppe et al., 2000, Güttler et al., 2010). Since water ice has a higher surface energy compared to silicates, Wada et al. (2009) found in simulations fragmentation velocities of water ice particle in the order of 50 m/s, suggesting that outside of the water ice line particles barely fragment. However, Gundlach and Blum (2015) found in collision experiments with water ice fragmentation velocities in the order of 10 m/s. Furthermore, Musiolik et al. (2016a) found that water ice particles covered in CO_2 ice have more likely the collisional behavior of CO_2 than that of water ice. They also determined the fragmentation velocity of CO_2 ice to be in the order of 3 m/s. Data for CO ice does not exist, yet. We therefore set the fragmentation velocity in our model to $v_{frag} = 5$ m/s. We also do not change the fragmentation velocity across the CO ice line. We assume, that particles crossing the CO ice line are still covered by a significant amout of CO_2 ice and do not yet benefit the high fragmentation velocity of water ice.

Evaporation and condensation is treated by solving the Hertz-Knudsen equation as described in chapter 2 with the saturation pressure of CO as given by Leger et al. (1985)

$$P_{CO}^{eq}(T) = 1 \frac{dyn}{cm^2} \exp\left[-\frac{1030\,K}{T} + 27.37\right]. \tag{3.26}$$

Table 3.1 lists the input parameters used in the fiducial model.

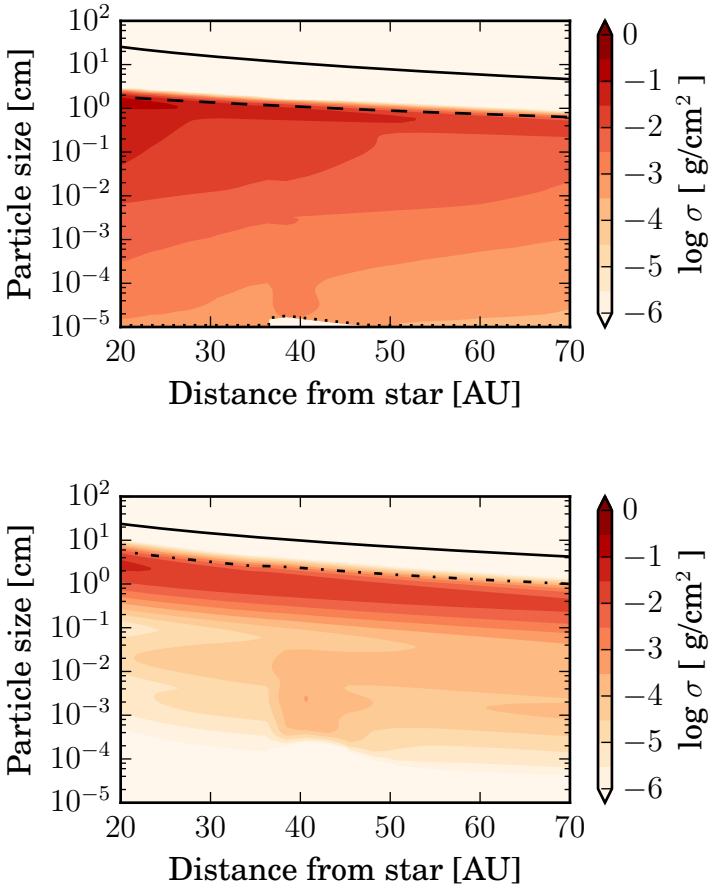

Figure 3.2: Comparison of the fiducial model (top) to a model without fragmentation (bottom) after 0.5 Myrs. The *solid* line marks in both cases particles with Stokes number St=1. The dashed line in the top plot is the analytical solution for fragmentation limited growth, while the dash-dotted line in the bottom plot is the analytical solution for drift limited growth as given by Birnstiel et al. (2012). The dotted line in the top plot shows the monomer size, that is, the smallest particles at each distance.

3.3 Results

Figure 3.2 shows a comparison of the fiducial model in this work with a model without particle fragmentation (i.e., $p_c = 1,\ p_f = 0$) as in chapter 2 after 0.5 Myrs. The quantity shown is

$$\sigma\left(a;R\right) = \int_{-\infty}^{\infty} n\left(a;R,z\right)\cdot m\cdot a\ \mathrm{d}z. \tag{3.27}$$

The solid black line in both plots shows the particle sizes that have a Stokes number of unity, that is, the fastest drifting particles. The dashed black line in the fiducial case (top) marks the analytical solution of the fragmentation barrier $a_{\text{frag}}(R)$ as given by Birnstiel et al. (2012)

$$a_{\text{frag}}(R) = \frac{2}{3\pi} \frac{\Sigma_{\text{gas}}}{\rho_{\text{sil}}} \frac{v_{\text{frag}}^2}{c_{\text{s}}^2}. \tag{3.28}$$

The dash-dotted line in the case without fragmentation (bottom) marks the analytical solution of the drift barrier $a_{\text{drift}}(R)$, by comparing the drift timescale to the growth timescale

$$a_{\text{drift}}(R) = \frac{2}{\pi} \frac{\Sigma_{\text{dust}}}{\rho_{\text{sil}}} \frac{v_{\text{K}}^2}{c_{\text{s}}^2} \left| \frac{\mathrm{d} \ln P}{\mathrm{d} \ln R} \right|^{-1}. \tag{3.29}$$

Without fragmentation, the particles grow until they approach the drift barrier. Here, the drift timescale is shorter than the growth timescale causing the particles to drift inwards rather than to grow. The small particles coagulate rapidly into larger particles and are strongly depleted. In the fiducial model with fragmentation, the particles grow until they hit the fragmentation barrier. Particles of that size rather fragment instead of growing further. When these particles fragment, the number of smaller particles down to sub-micrometer sizes gets replenished. We therefore have small particles throughout the disk. The ice line in both cases is at approximately 36 AU. When particles drift through the ice line they lose their CO through evaporation. This newly created CO vapor can diffuse backwards through the ice line and can recondense on the particles there. It will mostly recondense on the smallest particles, since they contribute most to the total surface area. The smallest particles in our simulation will therefore grow in size. The dotted line in the fiducial model in the top plot marks the smallest particle sizes at each radius. In a region outwards the ice line up to 50 AU the size of the smallest particles, the monomers, is enhanced by recondensation of CO vapor onto them.

Figure 3.3 shows the ice fraction Q of the smallest particles in each simulation after 0.5 Myrs. We compare the fiducial model to a model without fragmentation. Without fragmentation, the ice fraction is significantly higher outside the ice line at 36 AU compared to the fiducial model. Also, the region outwards the ice line, where the ice fraction is enhanced above normal, is significantly larger. The reason for that is twofold. Without fragmentation the particles are larger on average. This leads to a higher flux of CO ice on the dust particles through the ice line, since larger particles drift more rapidly. This deposits more CO vapor at the ice line that can recondense on the particles just outside the ice line. And second, the absence of small particles in the model without fragmentation decreases the available surface area outside the ice line on which the CO vapor could recondense. Therefore, the backwards diffusing CO vapor can reach larger distances, before it is fully recondensed on the particles.

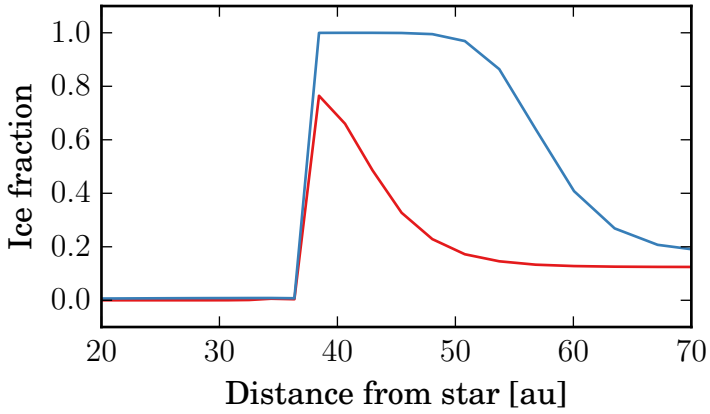

Figure 3.3: Comparison of the ice fraction of the monomers in the fiducial model (red) with a model without fragmentation (blue) after 0.5 Myrs.

3.3.1 Monomer Size-dependent Fragmentation Velocity

The fragmentation velocity, in general, depends on the monomer sizes within dust aggregates aggregates. The larger the monomers, the smaller is the fragmentation velocity. Dominik and Tielens (1997) showed that the fragmentation velocity depends on the monomer size a_0 as

$$v_{\text{frag, mono}} \propto a_0^{-\frac{5}{6}}. \tag{3.30}$$

Therefore, we implemented a monomer size-dependent fragmentation velocity in our model with

$$v_{\text{frag, mono}}\left(R\right) = v_{\text{frag}} \left(\frac{a_0\left(R\right)}{a_{\text{min}}} \right)^{-\frac{5}{6}}, \tag{3.31}$$

where $a_{\text{min}} = 0.1$ μm is the size of ice-free monomers in our simulations. $a_0\left(R\right)$ is the monomer size, i.e, the smallest particle size at each radius.

Figure 3.4 shows a model with the same initial conditions as the fiducial model after 0.5 Myrs, but where we implemented the fragmentation velocity as in equation (3.31) (called *mono* model from now on). The color map on top shows the vertically integrated dust surface densities as in equation (3.27). The solid black line marks the particle sizes of Stokes number unity. The dashed black line is the analytical solution for the fragmentation barrier $a_{\text{frag}}\left(R\right)$ (cf. equation (3.28)), which is now depending on the monomer size. The CO ice line is at about 36 AU. Compared to the fiducial model in figure 3.2, the mono model shows a depression in the maximum particle size shortly outside the ice line. As seen in 3.4 (bottom), the monomer size (red line) outside the ice line is increased by up to 50 %, because of recondensation of CO vapor. This leads

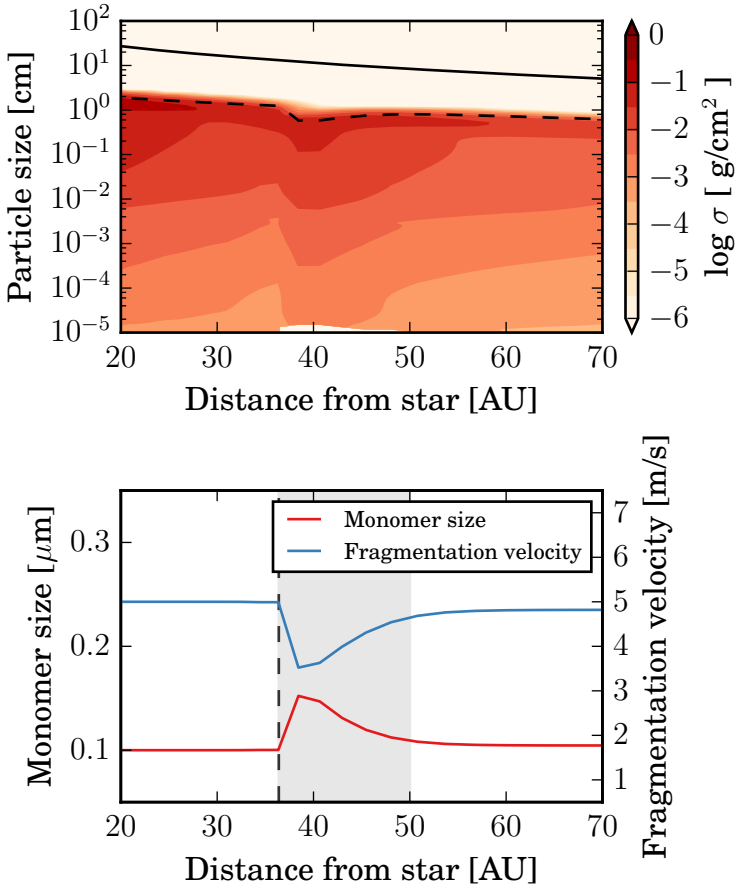

Figure 3.4: Top: Model in which the fragmentation velocity depends on the monomer size after 0.5 Myrs. The solid black line marks the particles with Stokes number St=1. The dashed line is the analytical solution for fragmentation limited growth $a_{\mathrm{frag}}(R)$ as in equation (3.28). Bottom: the red line shows the monomer size, that is, the size of the smallest particles, while the blue line shows the resulting monomer-dependent fragmentation velocity. The vertical dashed line is the location of the ice line and the gray shaded area is the recondensation region, in which the monomer sizes are enhanced.

to a decrease in the fragmentation velocity (blue line) and therefore to a decrease in the maximum particle sizes. The vertical dashed line marks the location of the ice line. The gray shaded area is the region, where the recondensation takes effect.

Figure 3.5 compares the particle size distributions in the fiducial model (red lines) with the mono model (blue lines) shortly inside the CO ice line (35 AU, solid lines) and shortly outside the ice line (40 AU, dashed). The particle size distributions in the fiducial model are very similar at both locations. The distribution outside the ice

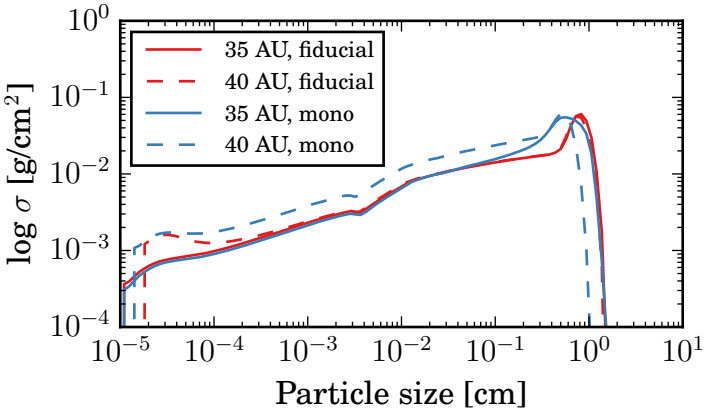

Figure 3.5: Particle size distributions shortly inside the ice line at 35 AU (solid lines) and shortly outside the ice line at 40 AU (dashed lines) in the fiducial model (red) and in a model with monomer size-dependent fragmentation velocities (blue) after 0.5 Myrs.

line (red dashed) lacks small particles. These particles are pushed to larger sizes by recondensation of CO vapor; therefore the bump at the lower end of the distribution. The distribution in the mono model outside the ice line (blue dashed) has a smaller maximum particle size compared to the fiducial model, which is caused by the lower fragmentation velocity in this region. The distribution in the mono case is in general larger at all particle sizes. At 35 AU both models have similar distributions. Only at the upper end, the mono model has a broader bump compared to the fiducial model.

In the mono model the particles are on average smaller in the region shortly outside the ice line. Smaller particles have smaller Stokes numbers and drift therefore less rapidly as seen by equation 1.31. This causes a "traffic jam" in the region of recondensation, where the particle sizes are reduced by smaller fragmentation velocities. Therefore, in these recondensation regions the surface density is enhanced. This is shown in figure 3.6, where we compare the surface densities of different characteristic particle sizes in the fiducial model with the mono model. The vertical dashed line is the CO ice line at 36 AU. The gray shaded area is the region of recondensation, where the monomer sizes are enhanced. In the mono model there are more smaller particles in the recondensation region, leading to a pile-up of material and therefore to an enhancement in total surface density. The bump in the fiducial model in total surface density just outside the ice line is solely caused by additional CO that gets evaporated when drifting through the ice line as seen already in chapter 2.

We ran several additional models, where we changed the CO abundance from 10^{-5} to 10^{-3} in both cases: with constant fragmentation velocity throughout the disk, and with a monomer size-dependent fragmentation velocity. Figure 3.7 shows the surface

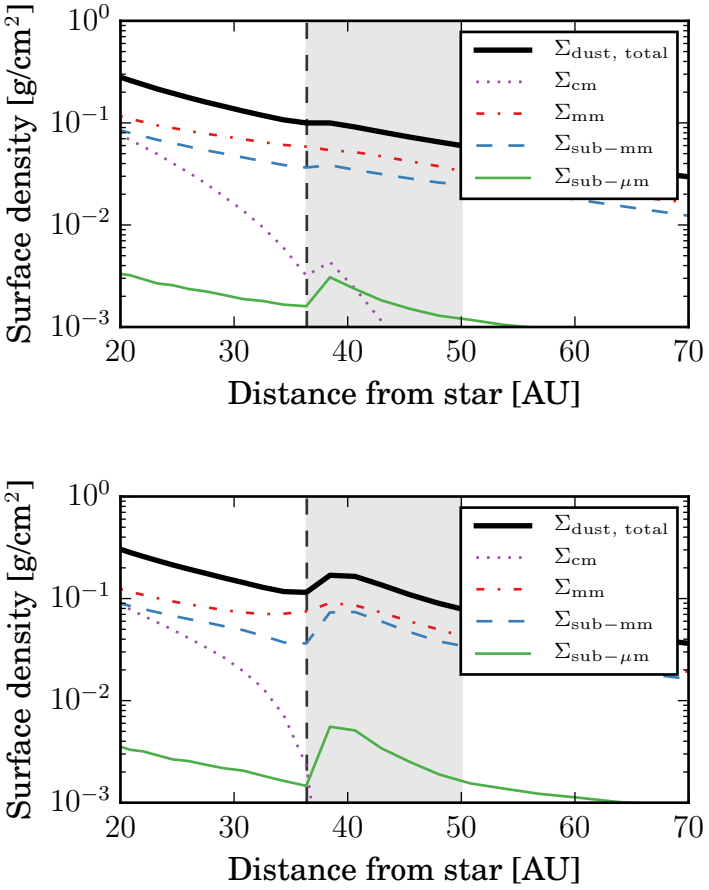

Figure 3.6: Comparison of the surface densities of different particle sizes in the fiducial model (top) and a model with monomer size-dependent fragmentation velocity (bottom) after 0.5 Myrs. The vertical dashed line is the location of the ice line and the gray shaded region is the recondensation region, in which the monomer sizes are enhanced.

densities after 0.5 Myrs in these models. The solid lines are models with a constant fragmentation velocity, while the dashed lines represent the models with a monomer size-dependent fragmentation velocity. The fiducial model is shown with a solid blue, the mono model with a dashed blue line. It can be seen that the CO ice line is closer to the star, the higher the CO abundance. With higher abundances evaporation and condensation can be in saturation at higher temperatures, shifting the ice line closer to the star as discussed in chapter 2. In the models with constant fragmentation velocities the features at the ice lines are only due to evaporation of CO. With monomer size-dependent fragmentation velocities the surface densities outside the ice line are enhanced due to the traffic jam effect. These pile-ups can enhance the surface densities

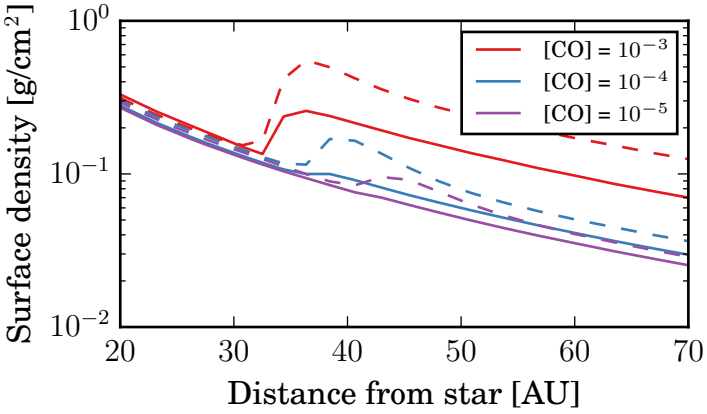

Figure 3.7: Total dust surface densities after 0.5 Myrs in models with constant fragmentation velocities (solid lines) and monomer size-dependent fragmentation velocities (dashed lines) for three different values of the CO abundance. The fiducial model is the solid blue line, the mono model in dashed blue.

significantly, as seen by the bump in the model with a CO abundance of 10^{-5} in the monomer size-dependent model, which is larger than the bump in the model with constant fragmentation velocity with a CO abundance of 10^{-4}.

In all these model the total dust surface densities show features at the ice line, while the total gas surface densities remain unchanged. In figure 3.8 we plot the total gas surface densities (solid lines) and the CO gas surface densities (dashed lines) for different CO abundances after 0.5 Myrs in models with monomer size-dependent fragmentation velocities. The dotted gray line represents the equilibrium CO surface density $\Sigma_{\mathrm{CO}}^{\mathrm{eq}}$. If the CO gas surface density follows this line, then evaporation and condensation are in equilibrium. In the inner disk the CO gas surface density decouples from the equilibrium CO gas surface density, because all CO ice is already evaporated. The location where this decoupling happens is then the position of the ice line (vertical lines). The more CO in the system, the closer to the star this decoupling happens. While there is a change in CO surface density at the ice line, no change in total gas surface density can be seen. Merely in the high abundance model, enough CO ice was transported through the ice line and evaporated, such that a tiny effect can be seen on the total gas surface density.

3.3.2 Radiative Transfer Simulations

We performed radiative transfer simulations at wavelengths of $\lambda = 1.3\,\mathrm{mm}$ and $\lambda = 1.6\,\mu\mathrm{m}$ to trace both, the millimeter continuum emission of the dust and the scattered light from the star.

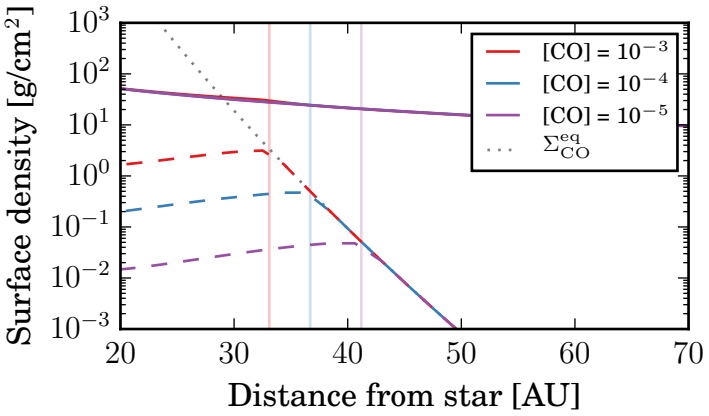

Figure 3.8: Gas surface densities in models with monomer size-dependent fragmentation velocities after 0.5 Myrs for three different CO abundances. The solid lines are the total gas surface densities, while the dashed lines are the pure CO gas surface densities. The dotted gray line represents the equilibrium CO gas surface densities Σ_{CO}^{eq}. The vertical lines are the positions of the ice lines in these models.

Figure 3.9 shows intensity maps of the millimeter continuum emission at a wavelength of $\lambda = 1.3$ mm of models with constant fragmentation velocity (top row) and monomer size-dependent fragmentation velocities (bottom row) for CO abundances of 10^{-5} (left column), 10^{-4} (middle column), and 10^{-3} (right column). The fiducial model is shown in the top middle panel, while the mono model is shown in the bottom middle panel. The intensity units are arbitrary but the same in all plots. In some of the models, ring-like features in the intensity can be seen. In general, the higher the CO abundance, the higher the contrast between the bright ring and the dark gap. In all cases, the CO ice line is located at the outer edge of the gaps, and is closer to the star, the higher the CO abundance is due to saturation effects.

Also, by using monomer size-dependent fragmentation velocities, the enhancement in surface densities outside the CO ice line caused by traffic jams increases the contrast between gap and ring. While in the models with constant fragmentation velocities and CO abundances of 10^{-5} and 10^{-4} barely any feature can be seen, there is clearly a ring visible in the low abundance case of 10^{-5} in the model with monomer size-dependent fragmentation velocities.

Figure 3.10 shows intensity maps in scattered light at a wavelength of $\lambda = 1.6$ μm of the same models as in figure 3.9 and with the same arbitrary intensity units. The scattered light traces small particles and therefore especially the recondensation region in the models with monomer size-dependent fragmentation velocities, since they get replenished by small particles due to the lower fragmentation velocities.

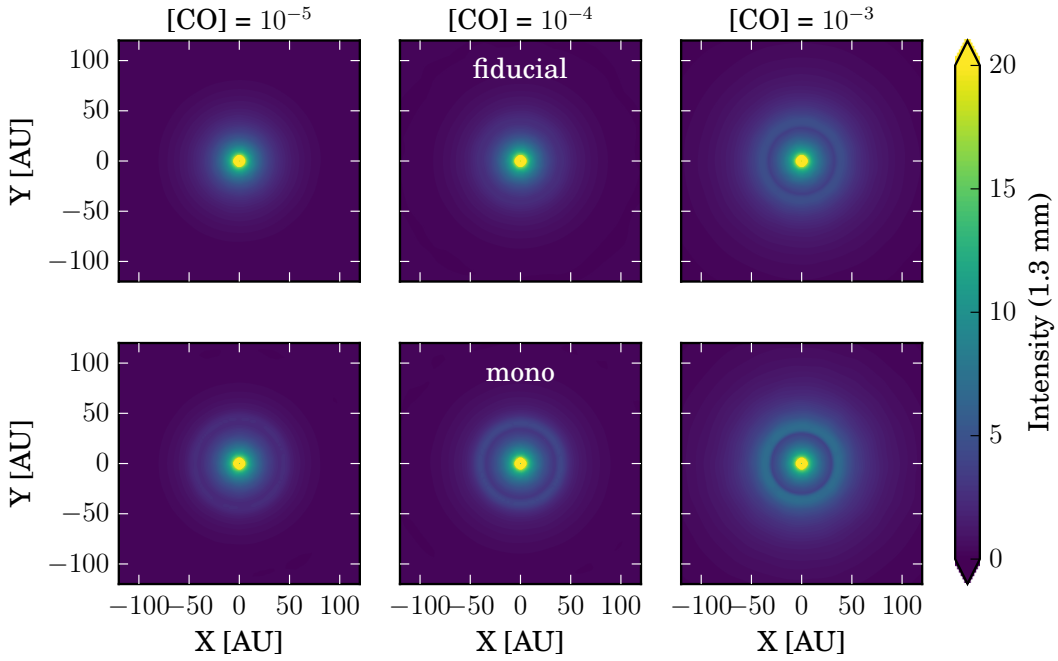

Figure 3.9: Radiative transfer simulations at a wavelength of $\lambda = 1.3\,\mathrm{mm}$ after 0.5 Myrs. In the top row are models with constant fragmentation velocities throughout the disk, whereas the bottom row shows models with monomer size-dependent fragmentation velocities. The left panels have CO abundances of 10^{-5}, the middle panels of 10^{-4}, and the right panels of 10^{-3}. The intensity units are arbitrary but the same for figures 3.9 and 3.10.

Figure 3.11 shows the radial intensity profiles of figures 3.9 and 3.10 in the region of interest around the CO ice line. The dashed lines are the models with constant, the solid lines with monomer size-dependent fragmentation velocities. The fiducial model is in dashed blue, the mono model in solid blue. At both wavelengths for the ISM CO abundance of 10^{-4}, the traffic jam caused by the variable fragmentation velocity, can enhance the intensity by a factor of approximately 2 compared to the models with constant fragmentation velocity. This enhancement then creates the optical illusion of a gap inside of the CO ice line.

3.4 Discussion

We implemented fragmentation in the dust and ice coagulation model presented in chapter 2. This has two effects on the particle sizes. First, the maximum particles size

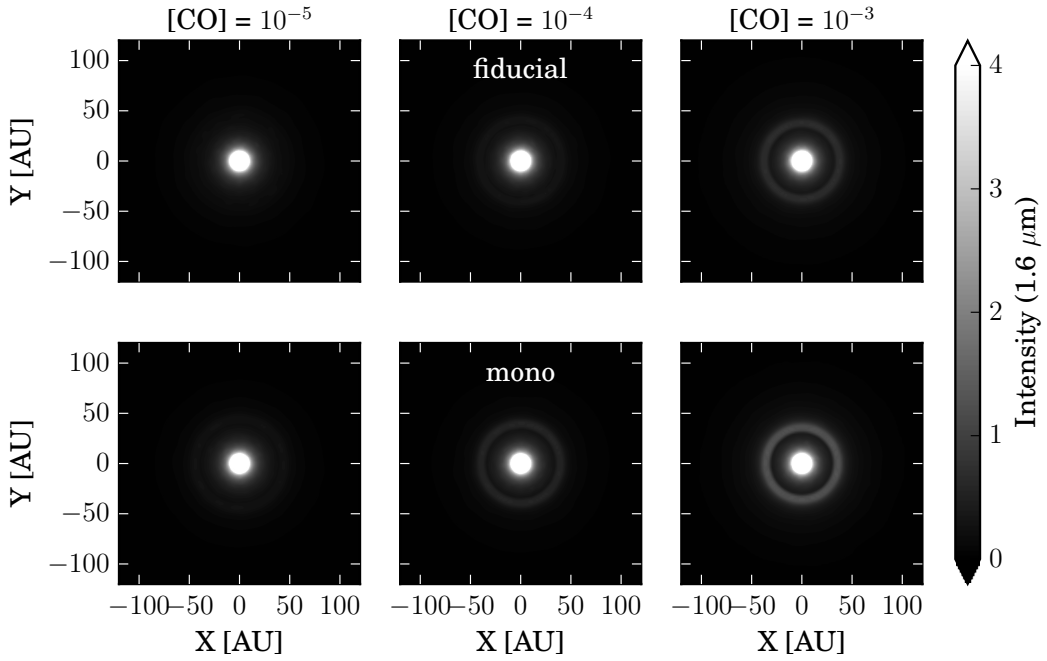

Figure 3.10: Radiative transfer models at a wavelength of $\lambda = 1.6$ ¯m after 0.5 Myrs. In the top row are models with constant fragmentation velocities throughout the disk, whereas the bottom row shows models with monomer size-dependent fragmentation velocities. The left panels have CO abundances of 10^{-5}, the middle panels of 10^{-4}, and the right panels of 10^{-3}. The intensity units are arbitrary but the same for figures 3.9 and 3.10.

is slightly reduced compared to the case without fragmentation. And secondly, fragmentation itself replenishes the small particles that are absent without fragmentation. This, in turn, has consequences on the distribution of CO ice on the particles. Without fragmentation, the particles have in a region of approximately 15–20 AU outside the ice line ice fractions of about 1. With fragmentation, the maximum ice fraction is about 0.8. Furthermore, the region of increased ice fraction is only 10 AU wide. Since the particles are on average smaller, their drift velocity and therefore the flux of CO ice through the ice line is smaller. Therefore, less CO vapor is deposited at the ice line. The small particles have also a higher combined surface compared to the large particle in the model without fragmentation. Thus, the CO vapor cannot diffuse far out in the disk before it gets recondensed.

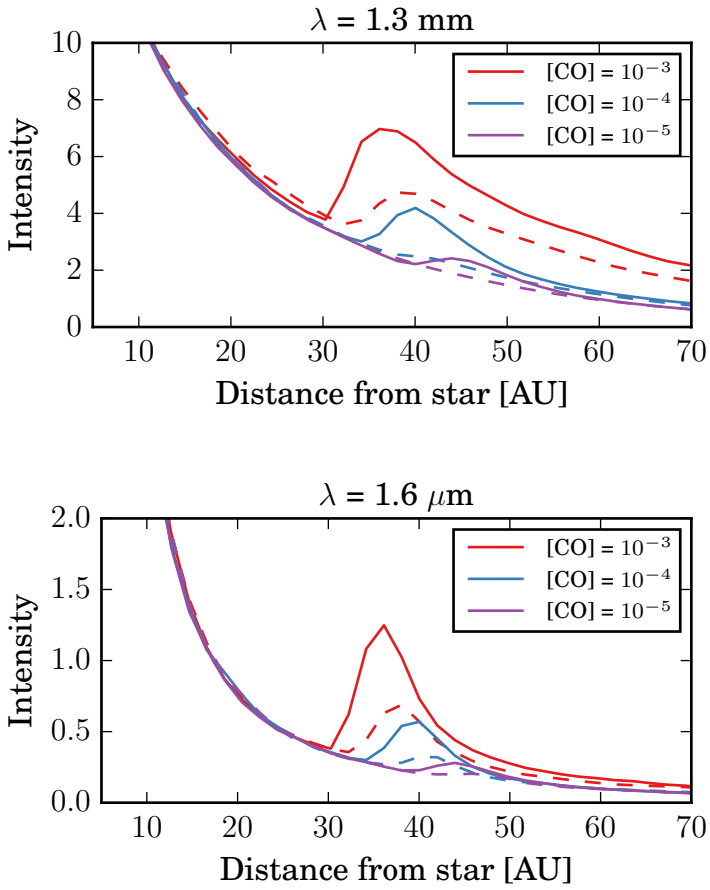

Figure 3.11: Radial intensity profiles of the radiative transfer models shown in figures 3.9 and 3.10. Top: $\lambda = 1.3\,\mathrm{mm}$. Bottom: $\lambda = 1.6\,\mu\mathrm{m}$. The dashed lines represent the models with constant, the solid lines the ones with monomer size-dependent fragmentation velocities.

Rings and Gaps caused by Ice Lines

But even in the case of fragmentation, the recondensation of CO vapor on particles outside the ice line is strong enough to increase the radius of the smallest particles by a factor of 1.5. Since the fragmentation velocity depends on the monomer size (Dominik and Tielens, 1997), this decreases the fragmentation velocity from 5.0 m/s down to 3.5 m/s in a narrow region outside the ice line. Due to enhanced fragmentation, this decreases the average particle sizes in this region. The smaller particles drift less efficiently, which lead to a traffic jam and an enhancement of the dust surface density.

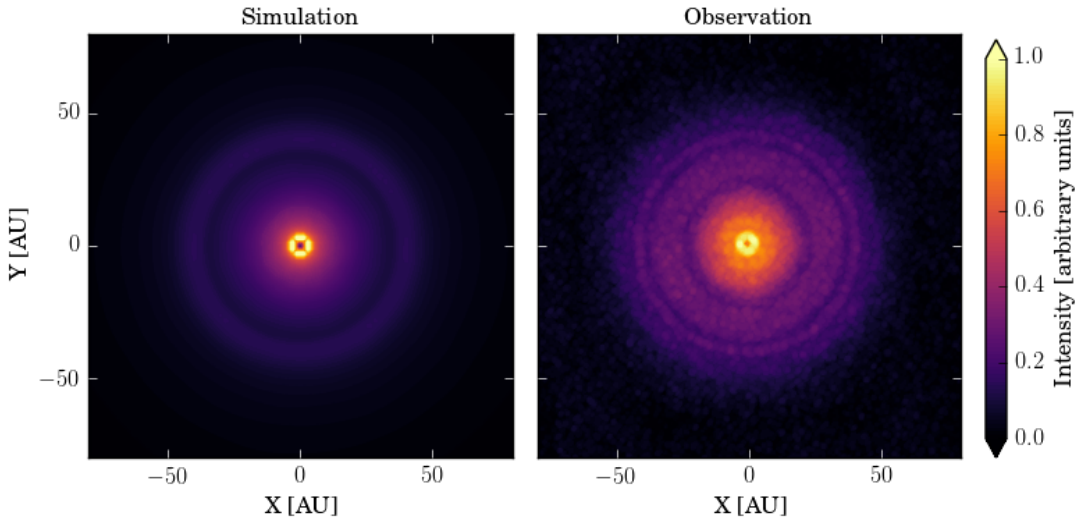

Figure 3.12: Comparison of the radiative transfer image of the mono model at $\lambda = 870\,\mu$m with the observations of TWydra at the same wavelength taken by Andrews et al. (2016). The intensities are normalized to the maximum in both cases.

Our radiative transfer calculations show, that this creates ring-like, axis-symmetric features in the intensity images. The strength of these features depends on the abundance of the considered volatile. This effect is very similar to the sintering-induced dust ring formation as proposed by Okuzumi et al. (2016). In sintering curvature effects are taken into account in the treatment of evaporation and condensation to the effect that the fragmentation velocity is reduced shortly outside of ice lines. In our model, we did not take into account sintering, nor any curvature of the particles, which would further increase the reduction of the fragmentation velocity.

In figure 3.12, we compare the intensity map of our mono model at $\lambda = 870\,\mu$m with the observations of the disk of TW Hydrae taken at the same wavelength by Andrews et al. (2016). Both, the intensities in the simulation and the observation, are normalized to their maximum. We did not fine-tune our simulation to match the observation. Hence, we do not match any of the gap locations. TW Hydrae is also significantly older. The position of the gap in the simulation does not match any of the gaps in TW Hydrae, suggesting that our chosen temperature profile differs from the one in TW Hydrae. Furthermore, the width of the gap is slightly larger in our model compared to any gap in TW Hydrae. This can be seen better in figure 3.13, where we compare the radial intensity profiles of the model with the observations. Both are again normalized to their maximum. The intensity profile of TW Hydrae is azimuthally averaged by Andrews et al. (2016). The ice line in the simulation is at 36 AU. Outside the ice line the intensity shows a rather broad excess. The intensity

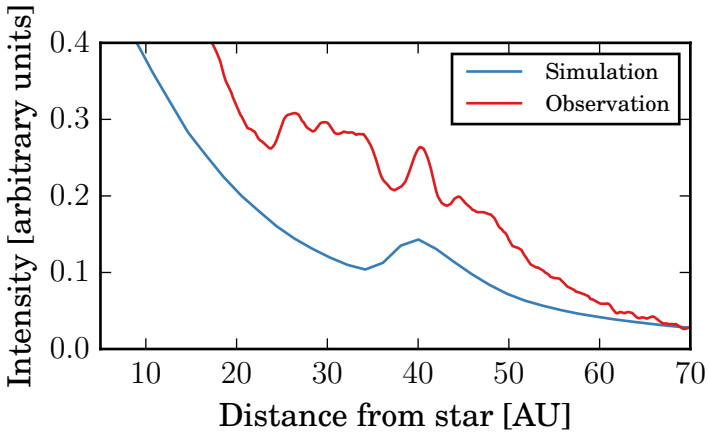

Figure 3.13: Comparison of the radial intensity profile of our mono model with the azimuthally averaged intensity profile of TW Hydrae taken by Andrews et al. (2016). Both intensities are normalized to their maximum.

features in the observation are more narrow compared to the simulation. It is open to future work to investigate the influence of other parameters, such as the temperature profile, the initial surface density profile, or the viscosity parameter α on the shape of the ice line features in our model.

Opacity Effects

Due to lack of experimental data for the optical constants of CO ice, we neglected any opacity changes across the ice line. In future works we aim to investigate, whether changes in the opacities across the ice line can enhance or reduce the features in the intensity maps at the ice line.

Gas Surface Density

We showed that changes in the fragmentation velocity can lead to accumulations of dust and to ring-like feature in dust observations. However, the total gas surface density does barely change across the ice line. Even in the case of high CO abundances, the accumulated CO at the ice line does not significantly change the total gas surface density. This is an important result, since this can help to discriminate between the ice line and the planet scenario for gap formation.

Planets carve gaps in the gas disk. The dust particles then follow the planet induced pressure gradients and clear the gap. By looking at gas observations in protoplanetary disks, it could be possible to identify the formation mechanism of the gaps. Dust gaps

caused by planets should also show a depression in the gas disk. Gaps by ice lines as presented in this chapter should not have any features in the gas disk.

Isella et al. (2016) discovered in their observations of HD 163296 three gaps in the millimeter continuum emission. The intensity profiles of the outer two gaps are consistent with being formed by a planet by comparing the shape of the gaps with simulations. However, the inner most gap seems to be too wide to be created by a planet. Isella et al. (2016) also presented gas observations of HD 163296. Both, the middle and the outer gap are depleted in gas, consistent with the planet scenario. Interestingly, the gas data at the inner gap could be consistent, within the error, with no gap at all. Therefore, the inner gap of HD 163296 is a candidate for a formation mechanism other than planets.

Are the Gaps in TW Hydrae caused by Ice Lines?

The model, presented in this chapter, is universal and should create gaps in every disk, at least for the most abundant molecules. We therefore tried to identify the molecules that could have formed the gaps in TW Hydrae under the assumption that all gaps are formed by ice lines. One possibility to do so is to compare the evaporation temperatures of the most abundant molecules with the temperature profile at the location of the gaps.

However, the mid-plane temperature of disks is typically rather unconstrained. We therefore look at the distance ratio A_{ij} of the gaps at R_i and R_j in TW Hydrae

$$A_{ij} = \frac{R_i}{R_j}, \tag{3.32}$$

such that A_{ij} is a number between 0 and 1. The gaps in TW Hydrae are at $R_1 = 22\,\mathrm{AU}$, $R_2 = 37\,\mathrm{AU}$, and $R_3 = 43\,\mathrm{AU}$ with widths of about 2 AU. Therefore, we have in total three different ratios A_{ij}.

By assuming a temperature profile as in equation (3.25), we can transform the ratio of the evaporation temperature of two molecular species i and j into a distance ratio

$$\frac{R_i}{R_j} = \left(\frac{T_{\mathrm{evap},j}}{T_{\mathrm{evap},i}}\right)^{\frac{1}{q}}. \tag{3.33}$$

In this way we drop the dependency on T_0. We can now compare the distance ratios of the evaporation temperature for several molecular species with the gap ratios in TW Hydrae and test whether they are consistent with a power law and what this would imply for T_0. We only look at the most abundant species as compiled in table 3.2.

Figure 3.14 shows three of the best fitting molecule combinations for TW Hydrae and the parameters of the temperature profiles. The data points are the evaporation

Table 3.2: Molecular species and their evaporation temperature taken from Zhang et al. (2015) and the references therein.

Molecular species	T_{evap} [K]
N_2	13.5 ± 1.5
CO	25.5 ± 2.5
CH_4	29.0 ± 3.0
H_2S	48.5 ± 3.5
CO_2	66.0 ± 6.0
NH_3	80.0 ± 6.0
CH_3OH	102.0 ± 8.0
HCN	110.0 ± 10.0
H_2O	141.5 ± 13.5

temperatures from table 3.2. The vertical gray areas are the location of the gaps of TW Hydrae. The order of the molecules in the caption of each plot is from the hottest to the coldest evaporation temperature of the molecules and therefore from the inner to the outer gap.

The two plots in the top row in figure 3.14 and the plot on the bottom left are the three combinations of three molecules that fit best with a power law and the distances of the gaps in TW Hydrae. The system with water (H_2O), hydrogen cyanide (HCN), and methanol (CH_3OH) seems to fit perfectly the gap distances in TW Hydrae and a power law with an exponent of $q = 0.49$ leading to a temperature of $T_0 = 639\,\mathrm{K}$ at 1 AU.

However, Hogerheijde et al. (2016) found the exponent of the power law in the brightness temperature in the inner 50 AU of TW Hydrae to be ~ 0.7. Also, Andrews et al. (2016) noted that the water ice line in TW Hydrae should be at about 1 AU, suggesting that $T_0 \sim 150\,\mathrm{K}$. Given that, all of the three fits are too hot to be consistent with the observations. The model on the bottom right of figure 3.1 shows the combination with the smallest T_0 of all the possible molecule combinations. Even here T_0 is too high to be consistent with the observations. And in addition to that, the fit is rather bad.

We therefore conclude, that either not all of the gaps in TW Hydrae are caused by ice lines, or the temperature profile in the region of the gaps can not be described by a power law. It is still possible, that one or two of the gaps are caused by ice lines, but this cross-correlation technique presented here does only work with three or more ice line gaps.

Another possibility is that the molecular ice species in protoplanetary disk do not exist in their pure form but as clathrates, where the molecule is trapped inside the lattice of a larger molecule. This changes the evaporation temperatures and would therefore lead to significantly different results. We showed in chapter 2 that inwards drifting

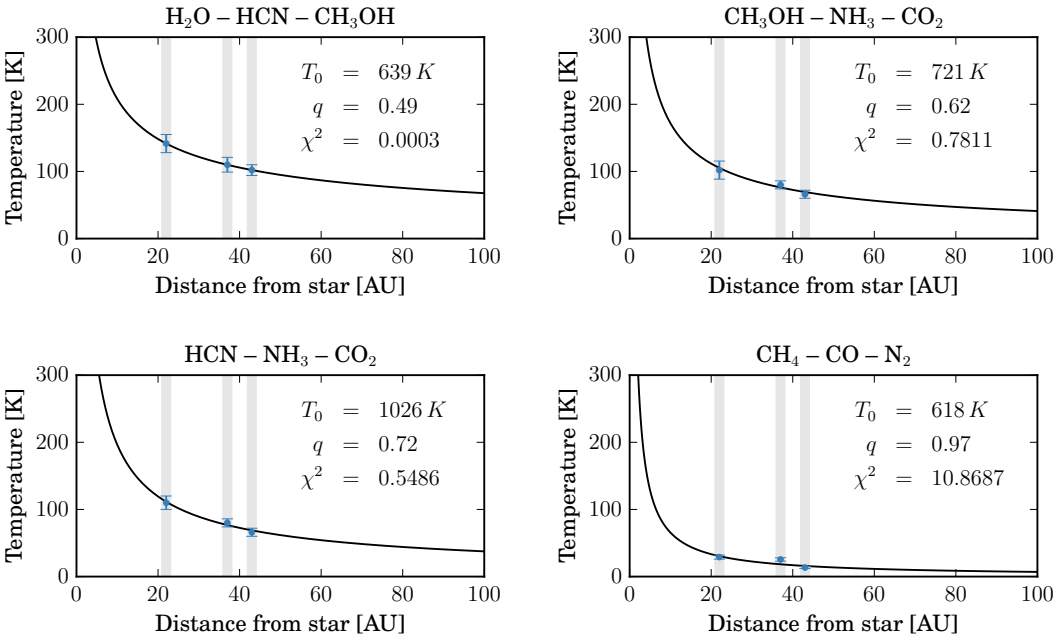

Figure 3.14: Four molecule combinations and their temperature power law fit to the gap locations in TW Hydrae.

particles can push the CO ice line several AU closer to the star. This would increase T_{evap} by about 2 K, which is smaller than the errors in T_{evap}.

3.5 Conclusion

Outside of ice lines, the volatile species is frozen out on dust particles. These dust particles drift inwards in the disk. When they cross the ice line, the volatile species evaporates. The newly created vapor can diffuse backwards in the disk and can recondense on the particles there. It will mostly condense on the smallest particles, since the contribute most to the total surface area. This increases the size of the smallest particles, the monomers, in regions just outside of ice lines.

The fragmentation velocity, in turn, is inversely proportional to the monomer size of dust aggregates. A larger monomer size just outside of ice lines leads to enhanced fragmentation and therefore to smaller particles in this region. Smaller particles drift less efficiently in protoplanetary disks. This causes a traffic jam which increases the dust surface density in these recondensation regions just outside of ice lines.

This enhancement in the dust surface density can be seen as ring-like, axis-symmetric features in millimeter continuum emission and in scattered light. This effect is stronger,

the higher the abundance of the volatile species is and might only be observable for the most abundant species in typical protoplanetary disks, such as H_2O, CO, CO_2, and N_2.

The gaps created by ice lines seem to be slightly broader than the gaps observed in TW Hydrae. But the influence of parameters like the temperature profile or the turbulent viscosity is still open to investigation. The three gaps in TW Hydrae seem to be inconsistent with being all caused by ice lines or with a single temperature power law.

In this model presented here, where gaps are caused by ice lines, the total gas surface density does not show a gap. Gas observations can therefore be used to distinguish gaps caused by planets from gaps caused by other mechanisms, such as ice lines. The inner most dust gap in HD 163296 is, for example, inconsistent with current planet gap models and might not have a gap in the gas surface density.

The influence of opacity changes across ice lines will be part of future works.

4

Chondrule Formation in Shock Waves

4.1 Motivation

The origin of chondrules is one of the biggest mysteries in meteoritics. These 0.1 mm to 1 mm sized silicate and once molten droplets, abundantly found in chondritic meteorites, must have cooled and solidified within a matter hours (e.g. Hewins et al., 2005). From short-lived radionuclide chronology data (e.g. Villeneuve et al., 2009) it is known that this must have taken place during the first few million years after the start of the solar system, during the phase when the sun was still likely surrounded by a gaseous disk (the "solar nebula"). What makes chondrule formation mysterious is that this rather short cooling time is orders of magnitude shorter than the typical time scale of a few million years of the evolution of the solar nebula. Thus, chondrules can not be a natural product of the gradual cooling-down of the nebula. Instead, chondrules must have formed during "flash heating events" of some kind – but which kind is not yet known. There exists a multitude of theories as to what these flash heating events could have been. So far none of these theories has been universally accepted.

One of the most popular theories is that nebular shock waves can melt small dust aggregates in the nebula, causing them to become melt droplets and allowing them to cool again and solidify (Hood and Horanyi, 1991). The origin of such shocks could be, for instance, gravitational instabilities in the disk (e.g. Boley and Durisen, 2008) or the effect of a gas giant planet (e.g. Kley and Nelson, 2012). Detailed one-dimensional models of the structure of such radiative shocks, and the formation of chondrules in them, were presented by Iida et al. (2001), Desch and Connolly (2002), Ciesla and Hood (2002) and Morris and Desch (2010). These models show that such shocks, in an optically thick solar nebula, would lead to a temperature spike in the gas and the dust that lasts for only a few seconds to minutes with cooling rates of up to 10^3 K/h, followed by a more gradual cooling lasting for several hours, with cooling rates of

the order of 50 K/h. These appear to be the right conditions for chondrule formation, which is one of the reasons why this model is one of the favored models of chondrule formation nowadays.

In this chapter we revisit this shock-induced chondrule formation model. Our aim is to investigate the role of the downstream boundary condition and the role of sideways radiative cooling.

If the shock is a large scale shock, e.g., due to a global gravitational instability, then on a small scale (the scale of several radiative mean free paths λ_{free}) the shock can be modeled as an infinite one-dimensional radiation hydrodynamic flow problem. Infinite, in this context, means that the three-dimensional geometry of the problem only becomes important on scales much larger than λ_{free}, so that on scales similar to λ_{free} a one-dimensional geometry can be safely assumed where the pre-shock boundary is set at $x = -\infty$ and the post-shock boundary is set at $x = +\infty$. With $\lambda_{\text{free}} = 1/(\kappa\rho)$ the pressure scale height of a typical minimum mass solar nebula is several hundred times larger than the optical mean free path. The shock is assumed to be stationary in the x-coordinate system, i.e., the coordinates move along with the shock and the shock is always at $x = 0$. In such an infinite one-dimensional system the full shock structure can be reconstructed when the physical variables at the upsteam boundary $x = -\infty$ are all given. No downsteam boundaries at $x = +\infty$ need to be given. In fact, the physical variables at the downstream boundary follow uniquely by demanding that the mass-, momentum- and energy-flux at the downstream boundary equals those at the upstream boundary, but with subsonic gas velocities. This gives a *global* Rankine-Hugoniot condition including all the radiative and dust physics. Note that right at the shock at $x = 0$ the jump in the gas variables is given by a *local* Rankine-Hugoniot condition in which only the gas fluxes on both sides are set equal. We will introduce our shock model in section 4.2 and show that after the temperature spike they lack a slow cooling phase of a few hours. Instead, they stay at a constant temperature, i.e., the temperature in accordance with the global Rankine-Hugoniot condition. We will investigate in section 4.3.1 whether the chondrule peak temperature can be made high enough for melting while keeping the post-spike temperature low enough to retain volatile elements. According to Fedkin et al. (2012) and Yu et al. (1996) the high-temperature phase should be of the order tens of minutes rather than of hours. From textural constraints, Hewins et al. (2005) and Desch et al. (2012) conclude that the cooling rates have to be of the order of $(10^1 - 10^3)$ K/h.

Since the infinite one-deimensional shock solution is a geometric approximation we will implement effects of sideways cooling (i.e., from the top and bottom of the disk) in section 4.3.2 to improve the realism of the model. This will re-introduce the slow cooling phase after the temperature spike, but we find that this slow cooling phase is of the order of weeks or months rather than hours, because two- or three-dimensional radiative diffusion will take place on lengthscales of the same order as the vertical scale height of the disk.

In section 4.3.3 we discuss two versions of the shock-induced chondrule formation where the cooling time can be rapid. One is a locally induced one, for instance due to a supersonic planetesimal bow shock (Hood, 1998, Morris et al., 2012). The other one is if the disk is fully optically thin, allowing the post-shock material to cool straight to infinity.

Finally, in section 4.3.4 we have a look at low velocity shocks that are not able to produce chondrules, but that have just the right temperatures to evaporate and crystallize water ice, which can have importance for dust coagulation models.

4.2 The Model

Our one-dimensional shock model is built upon the work of Desch and Connolly (2002). We used their approach, generalized it to arbitrarely many gas species, particle populations and chemical reactions and modified it where we think modifications or corrections are needed.

In this model we assume that all the parameters (densities, temperatures, velocities, etc.) only change along one direction, the x-direction. Therefore, the model consists of infinitely extended, plane-parallel layers of constant temperatures, velocities and densities.

4.2.1 Radiative Transfer

Even though the model is one-dimensional, we must allow the photons to move into all three directions. But fortunately, because of the plane-parallel assumption the radiative transfer equations here can be vastly simplified.

In this case the optical depth τ is a monotonically increasing function of the distance from the post-shock boundary and therefore a meassure of the position x inside the computational domain:

$$\tau(x) = \int_{x}^{x_{\text{post}}} \alpha \, \mathrm{d}x, \tag{4.1}$$

where x_{post} is the location of the post-shock boundary. This means the optical depth increases from $\tau(x_{\text{post}}) = 0$ at the post-shock boundary to a maximum value of $\tau(x_{\text{pre}}) = \tau_{\text{max}}$ at the pre-shock boundary. α is the absorption coefficient, which is the sum of the contribution of the gas and the particles:

$$\begin{aligned} \alpha &= \alpha_{\text{g}} + \alpha_{\text{p}} \\ &= \rho_{\text{g}} \kappa_{\text{P}} + n \pi a^2 \varepsilon. \end{aligned} \tag{4.2}$$

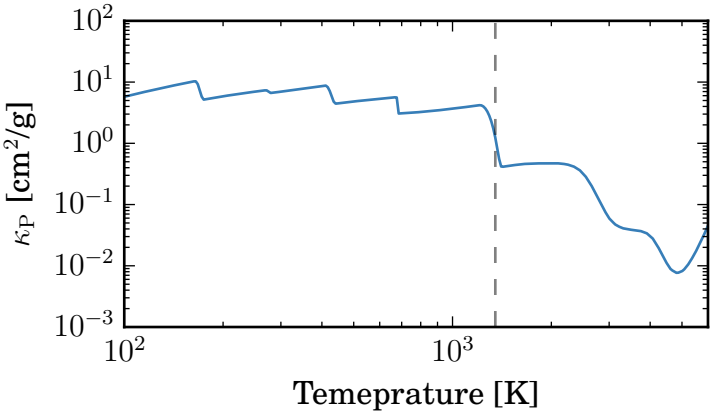

Figure 4.1: Planck-mean opacity taken from Semenov et al. (2003). At about 1 350 K (vertical line) the fine-grained dust associated with the gas gets evaporated. Therefore, the opacity drops by one order of magnitude at this temperature. This is responsible for the "opacity knee" in the pre-heating phase, where the gas becomes optically thin.

The absoption coefficient of the gas is the product of the gas mass density ρ_g and the temperature-dependent Planck-mean opacity κ_P, which we took from Semenov et al. (2003) shown in figure 4.1. The absorption coefficient of the particles is the product of their number densities n, their geometrical cross-section and their absoprtion efficiency ε, which we adopted from Desch and Connolly (2002) as

$$\varepsilon = 0.8 \times \min\left[1,\ \left(\frac{a}{2\ \mu\mathrm{m}}\right)\right], \tag{4.3}$$

where a is the particle radius.

To calculate the thermal histories of the particles one has to calculate the mean intensity $J_{\mathrm{rad}}(\tau)$ at every position τ. Our radiative transfer is grey, i.e., wavelength independent. The mean intensity is defined as the average intensity I per solid angle coming from all directions

$$J_{\mathrm{rad}}(\tau) = \frac{1}{4\pi} \int_{\Omega} I(\tau, \mu)\, \mathrm{d}\Omega. \tag{4.4}$$

In the plane-parallel assumption the intensity depends only on the position τ and the

angle θ between the incoming ray and the x-axis, where μ is defined as $\mu = \cos\theta$. Therefore, the mean intensity can be simplified to

$$\begin{aligned} J_{\text{rad}}(\tau) =& \frac{I_{\text{pre}}}{2} E_2(\tau_{\max} - \tau) + \frac{I_{\text{post}}}{2} E_2(\tau) \\ &+ \frac{1}{2} \int_0^{\tau_{\max}} S(\tau') E_1(|\tau' - \tau|) \, \mathrm{d}\tau', \end{aligned} \tag{4.5}$$

by using the exponential integrals

$$E_n(x) = \int_1^{\infty} \frac{e^{-xt}}{t^n} \mathrm{d}t, \tag{4.6}$$

as described by Mihalas and Mihalas (1984). $I_{\text{pre}} = \frac{\sigma}{\pi} T_{\text{pre}}^4$ and $I_{\text{post}} = \frac{\sigma}{\pi} T_{\text{post}}^4$ are the incoming radiations from both boundaries. The source function $S(\tau)$ is defined as

$$S = \frac{\rho_{\text{g}} \kappa_{\text{P}} B(T_{\text{g}}) + n\pi a^2 \varepsilon B(T)}{\rho_{\text{g}} \kappa_{\text{P}} + n\pi a^2 \varepsilon}, \tag{4.7}$$

which are the wave-length integrated Plank functions $B(T) = (\sigma/\pi) T^4$ of the gas and the particles at their given temperatures weighted by their respective emission efficiencies, which are the same as their absoprtion efficiencies according Kirchoff's law. σ is the Stefan-Boltzmann constant.

The radiative flux F_{rad} is defined as the net flux of radiative energy in x-direction

$$\begin{aligned} F_{\text{rad}} &= -\int_{\Omega} I(\tau, \mu) \cos\theta \mathrm{d}\Omega \\ &= -2\pi \int_{-1}^{1} I(\tau, \mu) \, \mu \mathrm{d}\mu. \end{aligned} \tag{4.8}$$

Later, we need the derivative of the radiative flux with respect to the x-direction. In the plane-parallel assumption this is simply

$$\begin{aligned} \frac{\partial F_{\text{rad}}}{\partial x} &= -4\pi\alpha (J_{\text{rad}} - S) \\ &= -4\pi\rho_{\text{g}}\kappa_{\text{P}} \left(J_{\text{rad}} - \frac{\sigma T_{\text{g}}^4}{\pi} \right) \\ &\quad - 4\pi \sum_{j=1}^{N_J} n_j \pi a_j^2 \varepsilon_j \left(J_{\text{rad}} - \frac{\sigma T_{\text{j}}^4}{\pi} \right), \end{aligned} \tag{4.9}$$

where we now included N_J different particle populations. Therefore, we have to take the sum over all populations.

4.2.2 Hydrodynamics

To calculate the evolution of the gas and particle parameters we used the one-dimensional stationary Euler equations, which are

$$\frac{\partial}{\partial x}(\rho V) = S_\rho \tag{4.10}$$

$$\frac{\partial}{\partial x}\left(\rho V^2 + P\right) = S_p \tag{4.11}$$

$$\frac{\partial}{\partial x}\left(\left(\rho e_{\text{tot}} + P\right) V\right) = S_e, \tag{4.12}$$

with the total mass density ρ, the velocity V, the pressure P and kinetic and thermal energy density e_{tot}. These equations are simply conservation laws of mass, momentum and energy respectively. S_ρ, S_p and S_e are the source terms of the designated quantities.

Particle Dynamics

In this model we have N_J different particle populations with radius a_j, temperature T_j, velocity V_j and number density n_j. The particles are not allowed to evaporate completely. This means the continuity equation (4.10) states

$$\frac{\partial}{\partial x}\left(n_j V_j\right) = 0. \tag{4.13}$$

The particles are accelerated or decelerated by the drag force $F_{\text{drag},j}$ acting on population j. The drag force is given by

$$F_{\text{drag},j} = -\pi a_j^2 \rho_g \frac{C_{D,j}}{2} \left|V_j - V_g\right| \left(V_j - V_g\right) \tag{4.14}$$

(Gombosi et al., 1986), with the gas' mass density ρ_g and the drag coefficient $C_{D,j}$ of population j. If the gas velocity is higher than the particle velocity, the particles get accelerated and vice versa. With that, the force equation of the particles is

$$m_j \frac{\mathrm{D}}{\mathrm{D}t} V_j = F_{\text{drag},j}, \tag{4.15}$$

with the particles' mass m_j and the comoving derivative $\mathrm{D}/\mathrm{D}t$, which is defined as

$$\frac{\mathrm{D}}{\mathrm{D}t} \equiv \frac{\partial}{\partial t} + \vec{V}_j \cdot \vec{\nabla} = V_j \frac{\partial}{\partial x}. \tag{4.16}$$

The last equality is for the one-dimensional, stationary case. Using this, the force equation (4.15) yields

$$m_j V_j \frac{\partial}{\partial x} V_j = F_{\text{drag},j}. \tag{4.17}$$

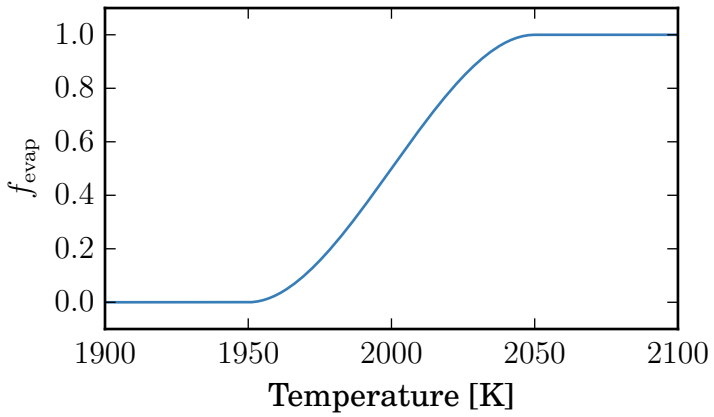

Figure 4.2: The fraction of evaporation f_{evap} yields for a smearing of the evaporation temperature of 2 000 K within our choice of the interval $\Delta T = 100\,\mathrm{K}$.

The energy budget of the particles is given by the balance between frictional heating by the gas drag, thermal contact with the gas and radiative heating on one hand and radiative cooling on the other hand. The effects of frictional heating and thermal contact with the gas are combined into a single heating rate q_j per unit surface area of the particle given by

$$q_j = \rho_{\mathrm{g}} C_{\mathrm{H},j} \left(T_{\mathrm{rec}} - T_j\right) \left|V_{\mathrm{g}} - V_j\right| \tag{4.18}$$

as given by (Gombosi et al., 1986), with the heat transfer coefficient $C_{\mathrm{H},j}$ and the recovery temperature T_{rec}. In the limit of $V_{\mathrm{g}} = V_{\mathrm{j}}$ there can be still heat exchange if $T\mathrm{g} \neq T\mathrm{j}$. The radiative heating rate per unit surface area of the paticles is given by $\varepsilon_j \left(\pi J_{\mathrm{rad}} - \sigma T_j^4\right)$, which is the balance between radiation received by the mean intensity J_{rad} and the energy radiated away according the Stefan-Boltzmann law. Combining the effects of frictional and thermal heating and radiative heating the net heating rate per unit surface area is $q_j + \varepsilon_j \left(\pi J_{\mathrm{rad}} - \sigma T_j^4\right)$.

This net heating rate can raise the particles' temperatures and/or evaporate them. We assume that the fraction of the net heating rate that goes into evaporation is $f_{\mathrm{evap},j}$, which is a function of the particle temperature. $f_{\mathrm{evap},j}$ increases monotonically from 0 to 1 within a temperature interval ΔT centered on the evaporation temperature of 2 000 K used by Desch and Connolly (2002). We have arbitrarely chosen $\Delta T = 100\,\mathrm{K}$ (see figure 4.2). We had to do this because of numerical reasons. Strong if-statements can make it impossible to estimate the Jacobian for the implicit integration scheme. But the positive side effect is that we can account now for the heterogeneity of the particle material with different evaporation temperatures.

Therefore, the change in the particles' temperature is given by

$$m_j C_{\mathrm{P},j} \frac{\mathrm{D}}{\mathrm{D}t} T_j = \left(1 - f_{\mathrm{evap},j}\right) \times \\ \times 4\pi a_j^2 \left[q_j + \varepsilon_j \left(\pi J_{\mathrm{rad}} - \sigma T_j^4\right)\right], \tag{4.19}$$

with the specific heat capacity at constant pressure $C_{\mathrm{P},j}$ of the particle material. Using again the definition of the comoving derivative (4.16), the particles' material mass density ρ_j and using $m_j = 4/3\pi\rho_j a_j^2$ the change in the particles' temperature can be written as

$$\frac{\partial}{\partial x} T_j = \frac{3\left(1 - f_{\mathrm{evap},j}\right)}{\rho_j a_j V_j C_{\mathrm{P},j}} \left[q_j + \varepsilon_j \left(\pi J_{\mathrm{rad}} - \sigma T_j^4\right)\right]. \tag{4.20}$$

The other part of the net heating rate, that goes into evaporation, is given by

$$H_{\mathrm{evap},j} \frac{\mathrm{D}}{\mathrm{D}t} m_j = - f_{\mathrm{evap},j} \times \\ \times 4\pi a_j^2 \left[q_j + \varepsilon_j \left(\pi J_{\mathrm{rad}} - \sigma T_j^4\right)\right], \tag{4.21}$$

with the latent heat of evaporation $H_{\mathrm{evap},j}$ of the particle material. The negative sign is needed because the heat received here goes into shrinking the particles' mass. This yields for the change in the particle radius

$$\frac{\partial}{\partial t} a_j = - \frac{f_{\mathrm{evap},j}}{\rho_j H_{\mathrm{evap},j} V_j} \left[q_j + \varepsilon_j \left(\pi J_{\mathrm{rad}} - \sigma T_j^4\right)\right]. \tag{4.22}$$

If the net heating rate is negative then $f_{\mathrm{evap},j}$ is set to zero to avoid artificial condensation in equation (4.22). We neglect condensation and nucleation here because we assume it takes place on much longer timescales than considered here. We want to point out that this implementation of evaporation is not the correct physical treatment. To do it in an correct way one has to integrate the Hertz-Knudsen equation as described in chapter 2 and possibly include a nucleation model, which makes the whole system even more complex. We also want to point out that in our conclusive simulations, the particle temperature is always safely below the evaporation temperature.

With the continuity equation of the particles (4.13) and the change in the particle velocity (4.17), the change in the particles' number densities can be calculated

$$\frac{\partial}{\partial x} n_j = - \frac{n_j}{V_j} \frac{\partial}{\partial x} V_j. \tag{4.23}$$

With equations (4.17), (4.20), (4.22) and (4.23) all the particle parameters can be calculated throughout the computational domain, if the gas parameters are known.

Gas Dynamics

The gas consists of N_I different gas species, which are assumed to be well-coupled and share the same temperature T_g and velocity V_g. Each species i has a number density n_i, which should not be confused with n_j of the particles, and a mean molecular weight m_i.

The model also includes N_K different chemical reactions with their respective net reaction rates R_k of reaction k, which are the number of reactions per unit time per unit volume. In chemical equilibrium the net reactions rates are equal to zero, which does not mean that no chemical reaction takes place.

Every reaction costs or sets free energy. The definition is such, that a positive reaction rate R_k sets free the energy e_k. That means that the total energy per unit time and unit volume set free by reaction k is $R_k e_k$. With chemistry the continuity equations of the different gas species are

$$\frac{\partial}{\partial x}\left(n_i V_\mathrm{g}\right) = \sum_{k=0}^{N_K} R_{i,k}, \tag{4.24}$$

where $R_{i,k}$ is the creation rate of gas species i due to reaction k, i.e., the change in number density n_i due to reaction k. The $k = 0$ component of the creation rates $R_{i,0}$ accounts for changes due to non-chemical processes, for example evaporation, where the mass of the evaporated material has to be added to the gas.

The total mass loss per unit time and unit volume of all particle populations is

$$\sum_{j=1}^{N_J} n_j \frac{\mathrm{D}}{\mathrm{D}t} m_j = \sum_{j=1}^{N_J} n_j V_j 4\pi\rho_j a_j^2 \frac{\partial}{\partial x} a_j. \tag{4.25}$$

This mass has to be added to the different gas species via the $k = 0$ component of their creation rates

$$R_{i,0} = -\frac{\xi_{\mathrm{evap},i}}{m_i} \sum_{j=1}^{N_J} n_j V_j 4\pi\rho_j a_j^2 \frac{\partial}{\partial x} a_j, \tag{4.26}$$

where $\xi_{\mathrm{evap},i}$ is the fraction of the evaporated mass added to gas species i. For mass conservation $\sum_i \xi_{\mathrm{evap},i} = 1$ has to hold.

To close the system of equations one has to solve for the gas temperature T_g, the gas velocity V_g and the number densities n_i. To do so we use Euler's momentum equation (4.11) and sum up the total momentum of the gas and the particles

$$\frac{\partial}{\partial x}\left[\sum_{i=1}^{N_I}\left(\rho_i V_\mathrm{g}^2 + n_i k_\mathrm{B} T_\mathrm{g}\right) + \sum_{j=1}^{N_J} n_j m_j V_j^2\right] = 0. \tag{4.27}$$

The first term in the sum over i is the momentum carried by the gas, the second term is the pressure according the ideal gas law. The sum over j refers to the momentum carried by the particles. Since the particles are pressureless there is no pressure term. This formula can be manipulated to get to

$$\begin{aligned}
&\left(\rho_\mathrm{g} V_\mathrm{g} - \frac{k_\mathrm{B} T_\mathrm{g}}{V_\mathrm{g}} \sum_{i=1}^{N_I} n_i\right) \frac{\partial}{\partial x} V_\mathrm{g} + \left(k_\mathrm{B} \sum_{i=1}^{N_I} n_i\right) \frac{\partial}{\partial x} T_\mathrm{g} \\
&= -\sum_{j=1}^{N_J} n_j \left(F_{\mathrm{drag},j} + 4\pi a_j^2 \rho_j V_j^2 \frac{\partial}{\partial x} a_j\right) \\
&\quad - \sum_{i=1}^{N_I} \sum_{k=0}^{N_K} R_{i,k} \left(V_\mathrm{g} m_i + \frac{k_\mathrm{B} T_\mathrm{g}}{V_\mathrm{g}}\right).
\end{aligned} \tag{4.28}$$

The same kind of calculations can be done for Euler's energy equation (4.12)

$$\begin{aligned}
&\frac{\partial}{\partial x} \left[\sum_{i=1}^{N_I} n_i V_\mathrm{g} \left(\frac{m_i V_\mathrm{g}^2}{2} + \frac{f_i + 2}{2} k_\mathrm{B} T_\mathrm{g}\right)\right. \\
&\left. + \sum_{j=1}^{N_J} n_j m_j V_j \left(\frac{V_j^2}{2} + C_{\mathrm{P},j} T_j\right) + F_\mathrm{rad}\right] \\
&= \sum_{k=0}^{N_K} R_k e_k.
\end{aligned} \tag{4.29}$$

The first term in the sum over i is the kinetic energy carried by the gas, whereas the second term is the sum of the internal energy of the gas and the pressure term according the ideal gas law. f_i is the number of degrees of freedom of gas species i. The first term in the sum over j is the kinetic energy carried by the particles, the second term is the thermal energy of the particles. In addition to that the radiative flux F_rad has to be included. The right hand side is not equal to zero, because energy can be

created or consumed by chemical reactions. This equation can be further manipulated to

$$
\begin{aligned}
& V_\mathrm{g}^2 \sum_{i=1}^{N_I} n_i m_i \frac{\partial}{\partial x} V_\mathrm{g} + k_\mathrm{B} V_\mathrm{g} \sum_{i=1}^{N_I} n_i \frac{f_i + 2}{2} \frac{\partial}{\partial x} T_\mathrm{g} \\
= \; & 4\pi \rho_\mathrm{g} \kappa \left(J_\mathrm{rad} - \frac{\sigma T_\mathrm{g}^4}{\pi} \right) + 4\pi \sum_{j=1}^{N_J} n_j \pi a_j^2 \varepsilon_j \left(J_\mathrm{rad} - \frac{\sigma T_j^4}{\pi} \right) \\
& - \sum_{i=1}^{N_I} \sum_{k=0}^{N_K} R_{i,k} \left(\frac{m_i V_\mathrm{g}^2}{2} + k_\mathrm{B} T_\mathrm{g} \frac{f_i + 2}{f_i} \right) \\
& - \sum_{j=1}^{N_J} n_j V_j \left(F_{\mathrm{drag},j} + 2\pi V_j^2 \rho_j a_j^2 \frac{\partial}{\partial x} a_j \right) \\
& - \sum_{j=1}^{N_J} n_j V_j m_j C_{\mathrm{P},j} \frac{\partial}{\partial x} T_j \\
& - 4\pi \sum_{j=1}^{N_J} n_j V_j C_{\mathrm{P},j} T_j a_j^2 \rho_j \frac{\partial}{\partial x} a_j \\
& + \sum_{k=1}^{N_K} R_k e_k .
\end{aligned}
\tag{4.30}
$$

Equations (4.28) and (4.30) are a set of two coupled differential equations, which can be solved for $\frac{\partial}{\partial x} V_\mathrm{g}$ and $\frac{\partial}{\partial x} T_\mathrm{g}$. Together with the continuity equation (4.24) of the gas and the particle differential equations (4.17), (4.20), (4.22) and (4.23) this closes the system of equations.

Setting $N_I = 4$ and using the gas species H, H_2, He and SiO this reduces in principle to the model of Desch and Connolly (2002), but correcting for some sign errors and implementing the smooth transition of the evaporation temperature.

4.2.3 Numerical Method

The system of equations (4.17), (4.20), (4.22), (4.23), (4.24), (4.28) and (4.30) is extremely stiff. Therefore it would require a very small step size and a very large number of grid points to numerically integrate it with an explicit integration scheme. We used here the implicit integrator *DVODE* (Brown et al., 1989) to integrate the equations simultaneously through the computational domain.

We perform our calculations in the comoving frame of the shock front, which is set to be at $x = 0$. At the shock front the gas parameters are changed according the Rankine-Hugoniot jump conditions, while the particle parameters remain unchanged.

After every complete integration the radiative transfer calculations have to be done again with the new particle and gas parameters. Then the integration is repeated with these new radiative parameters. This is repeatedly done until convergence is reached.

Another crucial point is the calculation of the post-shock boundary temperature T_{post}, which is needed for the radiative transfer calculation. Desch and Connolly (2002) calculated T_{post} by using incorrect jump conditions adopted from Hood and Horanyi (1991). This was corrected by Morris and Desch (2010) by calculating their own jump conditions. They found post-shock temperatures on the order of 1 300 K and concluded that chondrule formation is not possible in strictly one-dimensional models. Since disks are not one-dimensional objects, they will eventually cool by radiation. Therefore, Morris and Desch (2010) loosened the one-dimensional assumption by setting the post-shock temperature to the pre-shock temperature $T_{\mathrm{post}} = T_{\mathrm{pre}}$. This approach raises a problem, however, since it forces the gas and dust to radiatively cool through the downstream boundary. Since this downstream boundary is not a physical boundary, but just a computational boundary, this does not appear to be justified. The cooling is then dependent on the distance between shock front and post-shock boundary.

In our model we do not set the post-shock temperature a-priori since in a one-dimensional stationary model all downstream parameters are completely set by the upstream conditions. Therefore we perform right before the first iteration an additional integration without radiation. The temperature reached there at the post-shock boundary is then used as a first approximation of the post-shock temperature. After every further iteration, we check the radiative flux through the post-shock boundary. If the flux is positive i.e., the final temperature of the particles and the gas is higher than the post-shock temperature, we increase T_{post} slightly and vice versa. If convergence is reached then the radiative flux at the post-shock boundary is equal to zero. We want to point out that $F_{\mathrm{rad}} = 0$ is only true at the boundaries, which have to be far enough away from the shock front.

The post-shock temperatures we found by this approach are even higher than those calculated by Morris and Desch (2010). We think this is due to some approximations performed in deriving their jump conditions. Later in section 4.3.2 we introduce a method to perform simulations with a vertical energy loss.

4.3 Results

To compare our results to Desch and Connolly (2002) we used the same input parameter as they did.

We have one particle population with initial radius of 300 μm and a material mass density of 3.3 g/cm^3. Their initial number density can then be calculated by assuming

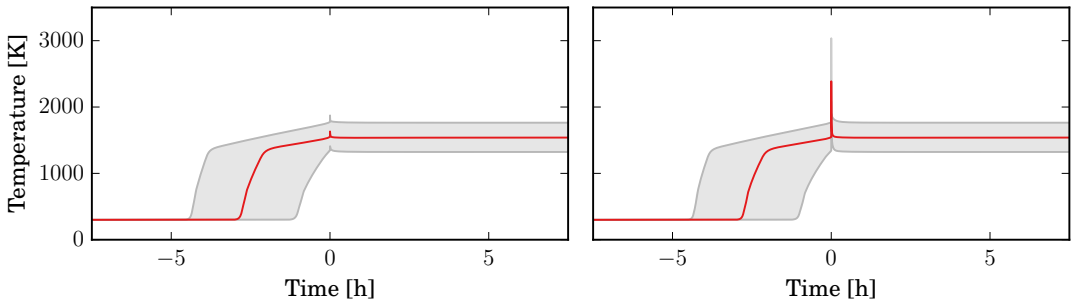

Figure 4.3: Left: Particle temperature in a shock with shock speed $V_{\mathrm{shock}} = 6.1\,\mathrm{km/s}$ (red line). The gray area marks the parameter space we explored, where the lower boundary represents a shock speed of $V_{\mathrm{shock}} = 5.3\,\mathrm{km/s}$ and the upper boundary a shock speed of $V_{\mathrm{shock}} = 7.1\,\mathrm{km/s}$. Right: Same as left but with the gas temperature.

a gas density of $10^{-9}\,\mathrm{g/cm^3}$, a dust-to-gas ratio of 0.005 and assuming that 75 % of the dust mass are in the chondrule precursors. The particles have a heat capacity of $C_{\mathrm{P}} = 10^7\,\mathrm{erg/g/K}$. Between 1 400 K and 1 820 K melting takes place. This results in an effective heat capacity of $C_{\mathrm{P}} = 2.19 \cdot 10^7\ \mathrm{erg/g/K}$ within this temperature interval. The latent heat of evaporation is $H_{\mathrm{evap}} = 1.1 \cdot 10^{11}\,\mathrm{erg/g}$.

The intial temperature of both gas and dust is 300 K. The gas consists of four species: atomic hydrogen, molecular hydrogen, helium and silicon monoxide (SiO). The only chemical reaction we consider is hydrogen dissociation and recombination, which consumes 4.48 eV for every H_2 molecule that breaks apart. We used the reaction rates given in Desch and Connolly (2002) adopted from Cherchneff et al. (1992). The reaction can also go in reverse direction; then setting free energy. If the gas exceeds 1 350 K, then the dust associated with it evaporates. The mass of the evaporated dust gets added to the silicon monoxide.

4.3.1 The Standard Shock

A standard shock with a shock speed of $V_{\mathrm{shock}} = 6.1\,\mathrm{km/s}$ is shown in figure 4.3. Most of the time the gas and the particles are well-coupled and share the same temperature. Already three to four hours before the shock front, the particles receive radiation from the hot gas and particles behind the shock. The temperature increases rapidly until roughly 1 350 K. From that point on the temperature only slightly increases towards the shock front. This change in slope is related to the opacity (see figure 4.1). As the gas reaches temperatures of $\sim$ 1 350 K the fine grained dust associated with the gas gets evaporated and the opacity drops by one order of magnitude. From that point on the opacity is purely caused by molecular lines. Therefore the pre-heating region can be sub-divided into an optically thick and an optically thin region. It is important that

the opacity is not set to zero because then the gas could not actively cool anymore. The only chance to lose energy would then be thermal contact with the particles. This would artificially slow down the cooling process.

At the position of the shock front only the parameters of the gas are changed ,i.e., without radiation or dust, according the Rankine-Hugoniot jump conditions wheareas the particle parameters remain unchanged. Therefore, the gas reaches temperatures as high as 2 500 K in the standard shock and even higher at higher shock speeds. The particles thensuddenly find themselves surrounded by gas that is much hotter than before the shock and that has velocities much smaller than those of the particles. The particles are now heated up by thermal contact with the hot gas and by frictional heating. But since the radiative cooling into the pre-shock region is relatively effective, both the gas and the particles quickly reach an equilibrium post-shock temperature before the particles are able to adapt to the high gas temperatures. In that way the maximum temperature the particles reach is $\sim$ 1 000 K smaller than the maximal gas temperature.

The constant post-shock equilibrium temperature is a consequence of the one-dimensionality of the model. As soon as the gas and the particles are a few optical depths behind the shock front there is no way for them to lose energy into the pre-shock region by radiation. Since the model consists of infinitely extended plane-parallel layers, they can not cool in lateral directions.

Therefore our model has in principle two different jump conditions: one is local at the position of the shock front, where only the gas parameters are changed according the Rankine-Hugoniot jump conditions. The other *global* jump condition forces the gas and particles to be at rather high post-shock temperatures after the relaxation of the temperature spike at the shock front.

From now on the maximum temperature the particles experience in the spike is referred to as peak temperature T_{peak}, whereas the equilibrium post-shock temperature is T_{post}.

The results for different shock speeds look similar. The lower the shock speed, the lower T_{peak} and T_{post} and the smaller the pre-heating region. Only if the shock speed is too low for the gas to reach 1 350 K, then there's also a lack of the "opacity knee" noticable.

The chemical reaction of hydrogen dissociation works as energy sink in this case. Instead of raising the temperature, energy is consumed in breaking molecular bonds. We want to point out that only a small fraction of the H_2 is dissociated as seen in figure 4.4. Since helium is chemically inert and does not react, the changes in number density seen in figure 4.4 are solely caused by compression of the gas at the shock. When the gas reaches 1 350 K the fine-grained dust associated with the gas gets evaporated. This dust gets added as SiO gas. Simulations without chemical reactions show an overall increase in temperature after the shock by $\sim$ 100 K. Because of the energy sink it is very important to include chemistry in such simulations: the temperature deviation

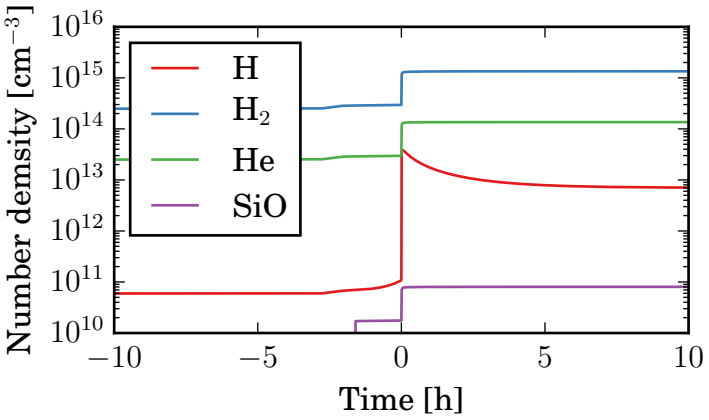

Figure 4.4: Number density profile of the gas species used in the model. Seen is the standard shock at $V_{\text{shock}} = 6.1\,\text{km/s}$. SiO gets added when the gas reaches a temperature of 1 350 K and the fine-grained dust associated with the gas evaporates.

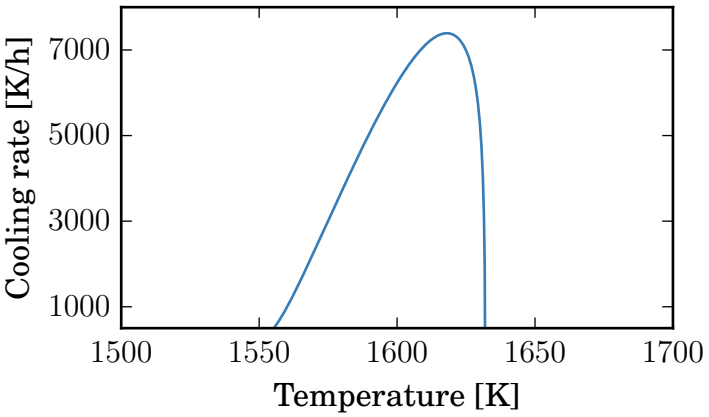

Figure 4.5: Cooling rates of the particles at particle temperatures $T > 1\,500$ K in the standard shock

can make the difference between losing particles via evaporation or not. Whether or not other chemical reactions are equaly important has to be investigated.

Figure 4.5 shows the cooling rates of the particles in the standard shock at temperatures $T > 1\,500$ K which is the important temperature regime for crystallization. As seen here the peak of the cooling rates is at the upper limit of what is allowed by experimental constraints. The standard shock itself is too weak to completely melt the

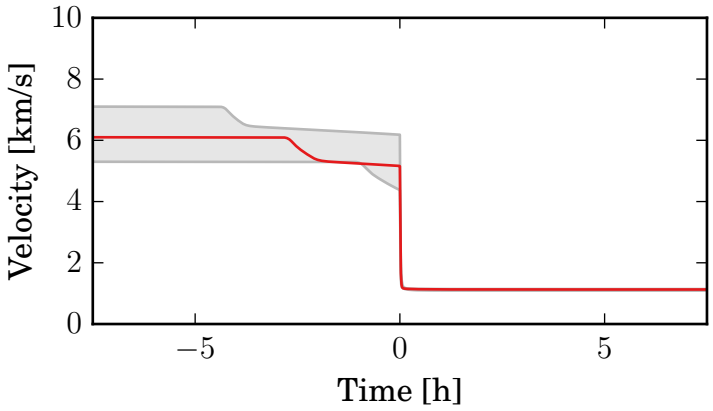

Figure 4.6: Velocity of the particles in the standard shock (red line). The gray area is the explored parameter space between 5.3 km/s and 7.1 km/s.

particles. In addition to that, the cooling rates drop to zero at already 1 630 K. This is discussed later in this section.

Another interesting feature is shown in figure 4.6. The velocity of the particles in the simulation. As soon as the pre-heating sets in the particles' velocity decreases because the gas velocity decreases. From initially 6.1 km/s to roughly 5.0 km/s shortly before the shock front. After the gas velocity is changed according the Rankine-Hugoniot conditions at the shock front the particles are rapidly decellerated by the drag force within minutes to $\sim$ 1.0 km/s.

The Mach number of the gas is initially of the order of 5. But due to the increase in temperature and decrease in velocity it is only roughly 2 at the position of the shock, where the Mach number is applied in the Rankine-Hugoniot conditions.

The problem of chondrule formation within this scenario is summarized in figure 4.7. If we assume that the particles have to reach a temperature of at least 1 820 K to be completely molten and at the same time to cool rapidly back down below at least 1 400 K to retain volatile materials which are observed in them, this is not possible in a one-dimensional model of an optically thick disk.

If we increase the gas mass density (see figure 4.8) the problem improves slightly and the two lines of peak and post-shock temperature are further apart. But only at unrealistic densities of $\gtrsim 10^{-6}\,\mathrm{g/cm^3}$ we could have both requirements fulfilled at the same time. According the disk model by Bell et al. (1997) these high midplane densities can only be found at radii of $\sim 10^{-3}$ AU or closer to the sun, where the temperatures are already on the order of 10^3 K to 10^4 K depending on the accretion rate.

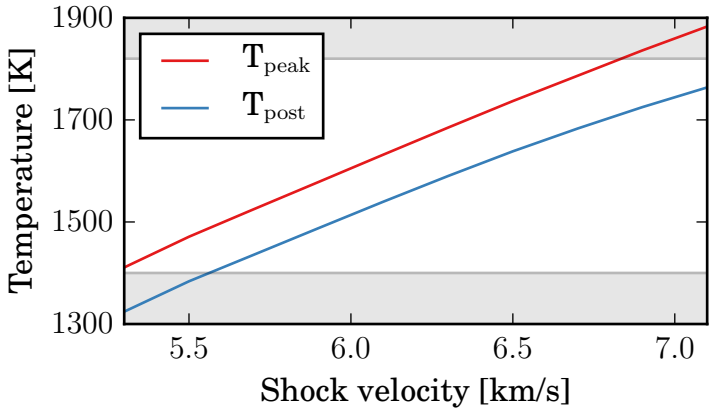

Figure 4.7: The peak and post-shock temperatures of the standard shock for different shock speeds. The upper solid line denotes a temperature of 1 820 K, which we assume the particles have to reach to be completely molten. The lower solid line is at 1 400 K. This is the temperature the particles have to reach at least after the shock to retain their volatiles. This is not possible in the standard case.

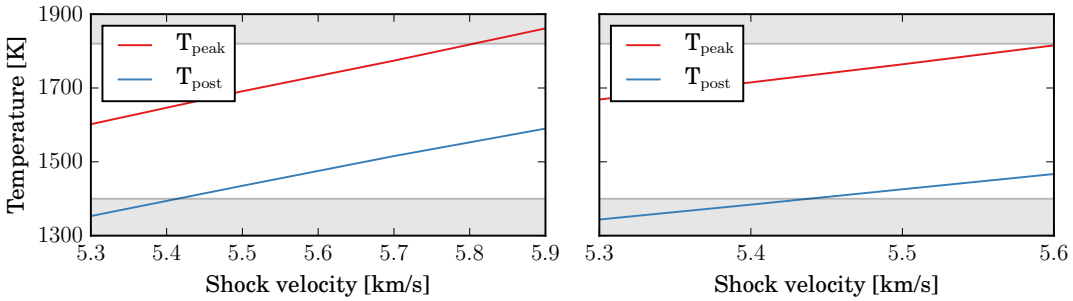

Figure 4.8: Same as figure 4.7 but with higher gas mass densities of $10^{-8}\,\mathrm{g/cm^3}$ (left) and $10^{-7}\,\mathrm{g/cm^3}$ (right). Note the different velocity scales.

But we want to point out that post-shock temperatures of 1 400 K might already be too high to retain the volatiles. In addition to that the particles are already at high temperatures in the pre-heating phase for a prolonged time ($\sim$ 3 h for the standard shock as seen in figure 4.3), which is already too long to be consistent with chondrule formation (Fedkin et al., 2012).

4.3.2 Vertical Energy Loss

It is clear that a one-dimensional, plane-parallel model does not match the situation in actual protoplanetary disks, since such disks are not one-dimensional objects. They have a vertical extent with decreasing densities at higher altitudes above the midplane. At $R = 3\,\mathrm{AU}$ (the region of the asteroid belt where most of the chondrules can be found today) the pressure scale height of a disk around a solar mass star with a midplane temperature of $T = 3\,00\,\mathrm{K}$ is $H_\mathrm{P} = \frac{k_\mathrm{B} T R^3}{\mu m_\mathrm{p} G M_\odot} \simeq 0.1\,\mathrm{AU}$, with the mean molecular weight of the gas $\mu \simeq 2.2\,\mathrm{amu}$ and the proton mass m_p.

If the disk is heated up by a shock whose propagation direction lies in the plane of the disk it can cool in vertical direction by radiative diffusion. But to cool down to the pre-shock temperature the gas and particles have to travel *at least* a distance comparable to the disk height. This is because in a vertically optically thick disk the radiative diffusion is a photon random walk: before it finds its way up a distance H_P, it has an equal chance of moving a distance H_P downstream. Radiative diffusion cooling will thus not create a steeper temperature gradient in the downstream (in-plane) direction than in vertical direction where the radiation escapes. A downstream cooling length of at least H_P (assuming $H_\mathrm{P} = 0.1\,\mathrm{AU}$) amounts, with a gas velocity of about $6\,\mathrm{km/s}$, to at least one month.

To estimate this we added an energy loss term to our equations

$$\frac{\partial}{\partial x} T^4 = -\frac{T^4 - T_\mathrm{pre}^4}{L}. \tag{4.31}$$

We transferred this energy loss into a temperature change and included it into the differential equation of our gas temperature

$$\frac{\partial}{\partial x} T_\mathrm{g} = \ \cdots\ - \frac{T_\mathrm{g}^4 - T_\mathrm{pre}^4}{4 T_\mathrm{g}^3 L}, \tag{4.32}$$

where the $\cdots$ denote the terms in the standard equation. The parameter L is a length scale, which determines the strength of the energy loss. The larger L, the smaller is the energy loss. Therefore L is also a rough estimate of the vertical extent of the disk assumed. With time the temperature should approach the pre-shock temperature.

We have done this for different length scale parameters essentially simulating disks in which all the dust has settled into a very thin midplane layer. The results are compared to the standard case, which corresponds to $L = \infty$, in figure 4.9. As seen here, the higher the energy loss (the lower the length scale L), the smaller are the pre-shock regions and the peak temperatures. The length scale parameters chosen here are extremely small, only a few percent of the disk's pressure scale height. It is very questionable if such disks exist. And even in those thin disks the particles are cooked at temperature above $1\,400\,\mathrm{K}$ for hours. The shock speed here is not even enough to completely melt the particles. And even with the vertical energy loss the particles still

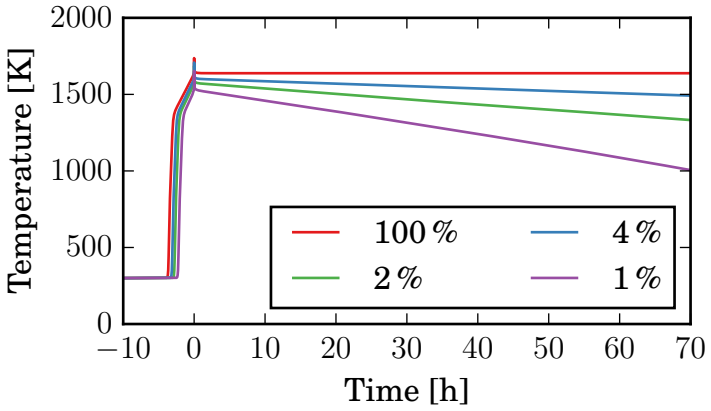

Figure 4.9: The standard shock (red) compared to simulations with a vertical energy loss with different loss parameters L of 4 % (blue), 2 % (green) and 1 % (purple) of the pressure scale height $H_P = 0.1$ AU at 3 AU.

spend upt to three hours in the high-temperature pre-shock phase. At higher shock speeds and therefore temperatures the situation is even worse.

4.3.3 Optically Thin Case

To investigate an optically thin case, where the particles can freely lose energy by radiation, we did another run where we set the mean intensity to $J_{\text{rad}}(\tau) = \frac{\sigma}{\pi} T_{\text{pre}}^4$ at every position. This means the gas and the particles are always in a radiation field with an ambient temperature of T_{pre}. At the shock front the gas parameters are changed as usual and the particles can adapt to it. This could correspond for example to bow shocks created by planetesimals on eccentric orbits (Hood, 1998). Here we assume the shocked volume of the disk is small compared to the unshocked medium such that the particles mostly see the radiation field from the unshocked gas. Of course, this assumption breaks down close to the shock front. But it could also represent the case for which the shock loses all opacity due to dust evaporation.

The result is shown in figure 4.10. As expected there is no pre-heating. Therefore the destination temperature for the jump conditions is lower and therefore also the target temperature. To reach the melting temperature in an optically thin case, we needed to increase the shock speed to $V_{\text{shock}} = 9.0\,\text{km/s}$, instead of $\sim 7.0\,\text{km/s}$ in the optically thick cases.

Right after the shock the gas and particles cool down rapidly and approach asymptotically the ambient temperature. The particles are only for a few minutes at critical temperatures and are back below 500 K after ~ 2 h.

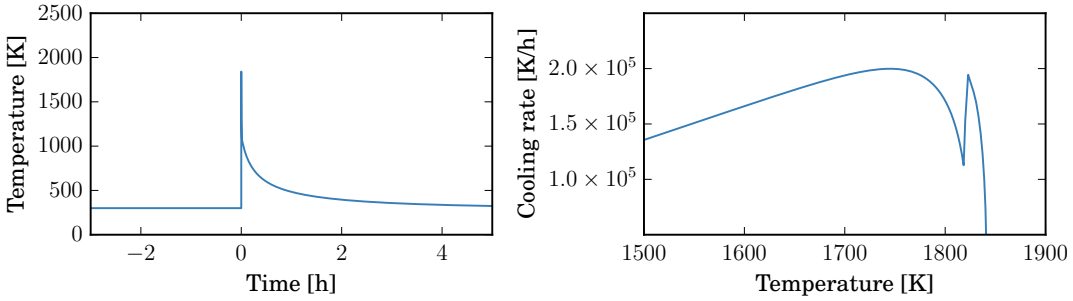

Figure 4.10: Particle temperature of an optically thin shock with a shock speed of $V_{\text{shock}} = 9.0\,\text{km/s}$.

Unfortunately, the cooling rates in figure 4.10 are at least two orders of magnitude too high in the crystallization regime at $T > 1\,500\,\text{K}$ to produce the observed chondrule textures (see e.g. Hewins et al., 2005, Desch et al., 2012). Since the Planck mean opacity is always an upper limit on the opacity we arbitrarily decreased it by a factor of 10^{-3} to investigate the effect of lower opacities. The gas has then a lower ability to directly cool by radiation. But even in this case, the cooling rates are still too large to be consistent with chondrule formation. Decreasing the opacity even further does not have any effect, since it is already low enough that the cooling via the particles is the dominant process.

In the bow shock scenario the optically thin approximation breaks down close to the shock front. Therefore, in reality there will be a pre-heating just before the shock front and less cooling after the shock. Whether this can produce the desired cooling rates has to be investigated by fully two-dimensional simulations. Further – but still one-dimensional – simulations by Morris et al. (2012) suggest that this could be the case.

4.3.4 Low Velocity Shocks

Figure 4.11 shows the thermal histories of particles in low velocity shocks of $V_{\text{shock}} = 1.575\,\text{km/s}$ (top) and $V_{\text{shock}} = 1.8\,\text{km/s}$ (bottom) with red lines. The inital temperature here is set to 70 K. The shocks have Mach numbers of about 2. We used the optically thin approximation for the radiative transfer calculations as described above. The peak temperatures are in both cases between 150 K and 200 K, which is not sufficient to melt silicate material and form chondrules. But these temperatures are just in the right range to influence water ice particles. We therefore developed a more realistic evaporation and condensation model and implemented crystallization of ice particles into the model.

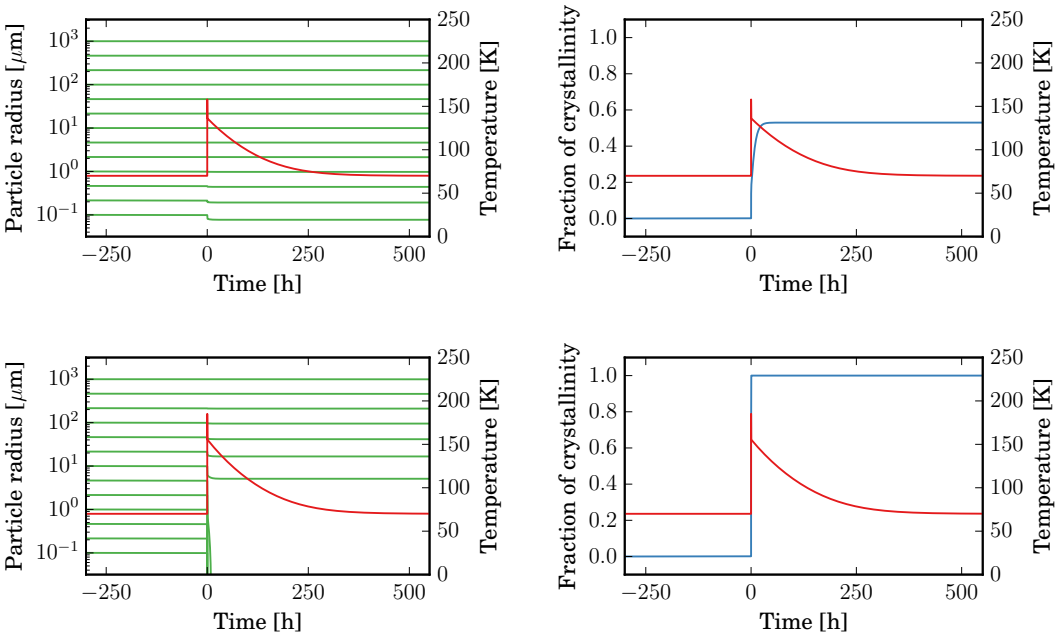

Figure 4.11: Thermal histories of water ice particles in low velocity shocks of $V_{\mathrm{shock}} = 1.575\,\mathrm{km/s}$ (top) and $V_{\mathrm{shock}} = 1.8\,\mathrm{km/s}$ (bottom) in the optically thin approximation with red lines. The green lines in the left column show the particle sizes of a few representative particles, while the blue lines in the right column show their fraction of crystallinity.

For evaporation and condensation we follow the method described by Bauer et al. (1997), which utilizes the Hertz-Knudsen equation described in chapter 2. The change in the radius of a particle due to evaporation and condensation is given by

$$\frac{\partial}{\partial t} a = \frac{\mu_{\mathrm{H_2O}}\, m_{\mathrm{p}}}{\rho_{\mathrm{H_2O}}} v_{\mathrm{th}} \left(n_{\mathrm{vap}} - \frac{P^{\mathrm{eq}}_{\mathrm{H_2O}}}{k_{\mathrm{B}} T} \right) \quad , \tag{4.33}$$

with the molecular weight of water $\mu_{\mathrm{H_2O}} = 18.015$, the bulk density of water $\rho_{\mathrm{H_2O}} = 1\,\mathrm{g/cm^3}$, the proton mass m_{p}, the thermal gas velocity $v_{\mathrm{th}} = \sqrt{8 k_{\mathrm{B}} T / \left(\pi \mu m_{\mathrm{p}}\right)}$, the water vapor number density n_{vap}, and the saturation pressure of water $P^{\mathrm{eq}}_{\mathrm{H_2O}}$, which is given by Bauer et al. (1997) as

$$P^{\mathrm{eq}}_{\mathrm{H_2O}}(T) = 1\,\frac{\mathrm{dyn}}{\mathrm{cm^2}} \times \exp\left[-\frac{6070\,\mathrm{K}}{T} + 30.86 \right] \quad . \tag{4.34}$$

McClure et al. (2015) found in observations crystalline water ice at trans-neptunian locations around T Tauri stars. The crystallization of water ice requires temperatures of about 120 K, which is by far greater than the typical temperatures expected at distances

greater than 30 AU around T Tauri stars. We therefore implemented crystallization into our shock model to investigate the influence of shocks on the crystallization fraction of dust particles. We followed here the method described by Gail (2001).

χ_{cr} is the fraction of crystallinity of a water ice particles shown in figure 4.11. But for the calculations it is more convenient to look at the quantity $\xi = \sqrt[3]{\chi_{\mathrm{cr}}}$. The change in ξ is then given by

$$\frac{\partial}{\partial t}\xi = \begin{cases} 2\sqrt[3]{\zeta_{\mathrm{cr}}}\,\nu_{\mathrm{vib}}\,\exp\left[\frac{-E_{\mathrm{a}}}{k_{\mathrm{B}}T}\right] & \text{if } \xi < 1 \\ \\ 0 & \text{else ,} \end{cases} \tag{4.35}$$

where ζ_{cr} is the initial fraction of crystalline growth centers, ν_{vib} the characteristic vibrational frequency of water ice, and E_{a} the activation energy, for which we adopted the values from Kouchi et al. (1994)

$$\begin{aligned} \zeta_{\mathrm{cr}} &= 10^{-5} \\ \nu_{\mathrm{vib}} &= 2.2 \cdot 10^{13}\,\mathrm{Hz} \\ \frac{E_{\mathrm{a}}}{k_{\mathrm{B}}} &= 5\,330\,\mathrm{K}\ . \end{aligned}$$

We integrate equations (4.33) and (4.35) together with the other quantities in the shock model. The results are shown in figure 4.11. The right column of figure 4.11 shows the fraction of crystallinity χ_{cr} in blue. In the case of a shock velocity of $V_{\mathrm{shock}} = 1.575\,\mathrm{km/s}$ (top), the crystallinity fraction rises to about 0.5 in the shock, while in the case of a shock speed of $V_{\mathrm{shock}} = 1.8\,\mathrm{km/s}$ (bottom), the particles are fully crystallized.

The left column shows the particle radii of a few representative particles in green. In the slow shock, that crystallizes the particles to about 50 %, the particles start to evaporate by a tiny amount. In the strong shock, that crystallizes the particles completely, the smaller particles fully evaporate. Only particles initially larger than 10 μm survive the shock.

4.4 Conclusion

Our one-dimensional radiative nebular shock model treats the variables at the downstream boundary as output of the model instead of boundary conditions that can be set. The iteration of the model then automatically finds the right downstream state of the matter, given the upstream boundary conditions. We find that this procedure prevents a post-shock slow (few minutes) cooling process. Instead, after the temperature spike and super-rapid cooling right after the main shock, the temperatures stay virtually constant. Only at distances from the shock comparable to the scale height

of the disk will the one-dimensional approximation break down and will sideways, i.e., upward and downward cooling set in. In our model we mimic this with a simple sideways cooling term.

For cases where the shock structure is *local*, for instance the bow shock of a planetesimal (see Morris et al., 2012), the shock scenario for chondrules might work because then the one-dimensional plane parallel assumption breaks down and sideways cooling can commence in a matter of hours. If the disk is optically thin then the cooling rates are too high to be consistent with the constraints on chondrule formation.

We conclude that while the nebular shock model for chondrules may work for local shocks (e.g. planetesimal bow shocks) the scenario has difficulties for global shocks in an optically thick nebula. This is because such global radiative shocks do not produce sufficient cooling after the temperature spike to be consistent with meteoritic constrains.

Low velocity shocks with velocities of 1.575 km/s and 1.8 km/s are not strong enough to produce chondrules, but they reach temperatures where water ice is evaporating. This can have an important effect for dust coagulation models. Since water ice is thought to be more sticky than silicate dust, losing all the water ice would decrease the fragmentation velocity and therefore the maximum particle size. At shock velocities of about 2.0 km/s, all the ice particles are fully evaporated. But even at lower shock speeds of about 1.8 km/s, the smallest particles are lost due to evaporation. Only particles larger than 10 μm survive. This, too, can have an influence on the particle growth, since the fragmentation velocity is inversely proportional to the size of the smallest particles – the monomers – as discussed in chapter 3.

Both low velocity shocks shown here are able to crystallize the water ice particle either partially or completely. Ice crystals at distances larger than 30 AU around T Tauri stars as observed by McClure et al. (2015) can therefore be explained by shocks of rather low velocities.

5

Dust Spirals triggered by Shadows in Protoplanetary Disks

5.1 Motivation

Protostars are formed by gravitational collapse of molecular gas clouds. In that process protoplanetary disks often form as a byproduct of star formation. The accreting gas and dust cannot lose its angular momentum and accumulates therefore in circumstellar disks. In the current paradigm of planet formation, planets are formed out of the gas and dust in these disks. The exact mechanism of planet formation is yet unknown.

Recent high-resolution observations of dust in protoplanetary disks show details like gaps and rings (e.g. ALMA Partnership et al., 2015, Andrews et al., 2016) or spirals (e.g. Benisty et al., 2015, 2017). Gaps in protoplanetary disks are often attributed to existing planets carving gaps by tidal interaction with the gas (Lin and Papaloizou, 1986, Bryden et al., 1999) or to ice lines (Zhang et al., 2015, Okuzumi et al., 2016). Spirals in protoplanetary disks can arise from planets that excite density waves in the disk (Goldreich and Tremaine, 1979), from gravitational instabilities (Kratter and Lodato, 2016), or from close encounters by stellar flybys (Pfalzner, 2003).

Table 5.1 lists stars with known disks that show spirals in either scattered light, continuum emission, or both. Scattered light images are taken at typical wavelengths of about 1 μm. Given typical dust temperatures of a few tens of Kelvin, black body emission of the dust does not play a role at the observed wavelength. Therefore, scattered light images trace the photons that get reflected from the star into the line of sight. This is most effective for particles with sizes comparable to the observed wavelength. The images of continuum emission are taken at wavelength of about 1 mm. Here, the black body emission of the particles does play a role. Both, images from scattered light and continuum emission, trace therefore particles of different sizes.

Table 5.1: Stars having disks with detected spirals in scattered light and/or continuum emission.

Star identifier	Scattered light	Continuum emission
HD 142527	1	–
MWC 758	2, 3	2
HD 100453	4, 5	–
HD 135344B	6, 7	8
Oph IRS 48	9	–
HD 100546	10	–
Elias 2-27	–	11

1: Fukagawa et al. (2006), 2: Grady et al. (2013), 3: Benisty et al. (2015), 4: Benisty et al. (2017), 5: Wagner et al. (2015), 6: Muto et al. (2012), 7: Stolker et al. (2016), 8: van der Marel et al. (2016), 9: Follette et al. (2015), 10: Garufi et al. (2016), 11: Pérez et al. (2016)

From the stars of table 5.1, the disk around Elias 2-27 shows, in addition to spirals, a bright ring in the continuum emission. Of special interest are also the disks of HD 142527 and HD 100453. Both disk are transitional disks with large inner cavities. And both disks show two shadows each in scattered light images in nearly opposite directions. Marino et al. (2015) showed that the shadows in HD 142527 are consistent with a smaller unresolved inclined disk inside the cavity that casts shadows onto the outer disk in opposing directions.

Montesinos et al. (2016) showed in hydrodynamical simulations of gravitationally unstable disks that these shadows can trigger the formation of spiral waves in the gas density. As seen in chapter 1, dust particles drift along pressure gradients, depending on their size, respectively their Stokes number. Particles with Stokes numbers of unity drift most efficiently towards local pressure maxima in the disk.

The aim of this work is to investigate whether spiral waves induced by shadows are strong enough to accumulate particles, and if so, what are the preferred particle sizes that get trapped in the spirals. In a final step, we produce radiative transfer images of our results in scattered light and at millimeter wavelengths to compare them with the observations.

In section 5.2 we explain the numerical methods used to simulate the evolution of the gas and dust in a gravitationally unstable disk, where two shadows are cast in opposing directions. We also explain how we obtain radiative transfer images from our simulation results. In section 5.3 we present our results, which are further discussed in section 5.4. We conclude this chapter in section 5.5 and give a brief outlook to future projects.

5.2 Numerical Method

To investigate the dynamics of dust particles in protoplanetary disks with shadow-induced spirals as seen by Montesinos et al. (2016) we follow three steps:

1. We perform hydrodynamical simulations using FARGO-ADSG to obtain the evolution of the gas disk.
2. We calculate the dust particle dynamics utilizing the previously obtained FARGO-ADSG outputs.
3. We obtain radiative transfer simulations of the dust disk using RADMC-3D.

In the first step, we use FARGO-ADSG (Baruteau and Masset, 2008) to calculate the hydrodynamical evolution of a gas disk that is shadowed from the stellar light at two directly opposing points to mimic an inner inclined disk. We do not model the inner disk hydrodynamically. Then, we use these calculations to investigate the influence of the gas on dust particles orbiting in the disk. Finally, we perform radiative transfer calculations of the dust disk using RADMC-3D (Dullemond et al., 2016) to investigate how these disks look in scattered light and in millimeter emission and to compare our simulations with observations.

5.2.1 Hydrodynamical Simulations

We use FARGO-ADSG to simulate the evolution of a self-gravitating circumstellar gaseous disk. FARGO-ADSG is a two-dimensional hydrodynamical solver for circumstellar disks, having a radial coordinate R and an azimuthal coordinate φ. To allow for shadows, cast by e.g. an inner inclined disk, the code has to be modified. We follow here the method described in Montesinos et al. (2016), who included stellar irradiation, radiative cooling and shadows cast onto the disk.

The disk is irradiated by stellar light. The heating rate by stellar irradiation $Q_\star^+$ per unit surface area is given by Frank et al. (2002) as

$$Q_\star^+(R) = (1-\beta)\frac{L_\star}{4\pi R^2}\frac{H}{R}\left(\frac{\mathrm{d}\ln H}{\mathrm{d}\ln R} - 1\right), \tag{5.1}$$

where β is the albedo, $L_\star$ the stellar luminosity, and H the disk's scale height. We assume $\beta = 0$, which means that all incoming radiation gets absorbed by the disk. We further assume local hydrostatic equilibrium, which means the scale height H is given by:

$$H = \frac{c_\mathrm{s}}{v_\mathrm{K}}R, \tag{5.2}$$

where c_s is the sound speed and v_K the Keplerian velocity.

We now assume that an inner inclined disk exists, that blocks stellar light and casts two shadows onto the outer disk. The inner disk is assumed to be inclined by 90°, such that the shadows are symmetric and cast from two directly opposing points. Therefore, the stellar irradiation rate needs to be modified to account for the shadows

$$Q^{+}_{\text{shadows}}(R,\varphi) = f(\varphi)\, Q^{+}_{\star}(R), \tag{5.3}$$

where the function $f(\varphi)$ is given by

$$f(\varphi) = 1 - A\exp\left(-\frac{\varphi^4}{\sigma^2}\right) - A\exp\left(-\frac{(\pi-\varphi)^4}{\sigma^2}\right), \tag{5.4}$$

with $A = 0.999$ and $\sigma = 0.05$. This creates two shadows for $\varphi = 0$ and $\varphi = \pi$ with a width of about 15°, where the stellar heating rate is set to nearly zero with smooth transitions between the shadowed and non-shadows regions.

FARGO-ADSG solves the energy equation

$$\frac{\partial}{\partial t}e + \nabla\cdot\left(e\vec{v}_{\text{gas}}\right) = -P\nabla\cdot\vec{v}_{\text{gas}} + Q^{+}_{\text{shadows}} - Q^{-}, \tag{5.5}$$

where e is the vertically integrated thermal energy density, P the vertically integrated pressure, and $\vec{v}_{\text{gas}}$ the velocity vector of the gas. Q^{-} is the thermal cooling rate, which is given by

$$Q^{-} = 2\frac{\sigma_{\text{SB}}T^4}{\tau}, \tag{5.6}$$

with the Stefan-Boltzmann constant σ_{SB}, the mid-plane gas temperature T and the optical depth $\tau = \frac{1}{2}\Sigma\kappa$. We assume a constant opacity of $\kappa = 1\,\text{cm}^2/\text{g}$.

An ideal equation of state is used to close the system of equations

$$P = \frac{\Sigma T R_{\text{gas}}}{M}, \tag{5.7}$$

where R_{gas} is the universal gas constant and M the molar mass of the gas. The thermal energy e is then related to the pressure via $P = (\gamma-1)\,e$, where $\gamma = 1.4$ is the the adiabatic index.

Initial conditions

The disk is initialized with as surface density of

$$\Sigma(R) = 2500\,\frac{\text{g}}{\text{cm}^2}\times\left(\frac{R}{1\,\text{AU}}\right)^{-1}, \tag{5.8}$$

with an inner boundary at $R_{\text{in}} = 10\,\text{AU}$, and an outer boundary at $R_{\text{out}} = 1000\,\text{AU}$. The Shakura-Sunyaev viscosity parameter is set to $\alpha = 10^{-4}$. The star is solar-like with a mass of $M_\star = M_\odot$ and a luminosity of $L_\star = L_\odot$. The disk's temperature is initialized, such that it is in radiative equilibrium $Q^+_{\text{shadows}} = Q^-$.

We use $N_R = 400$ radial and $N_\varphi = 900$ azimuthal grid cells. Test simulations with higher resolutions of $N_R = 512$ and $N_\varphi = 2048$ do not show any difference, but are significantly more expensive, both, with respect to computational time and memory consumption. The disk is self-gravitating, meaning the gas does feel the gravitational potential of the star as well as of the disk itself. We simulate the disk for 10 000 years.

5.2.2 Particle Dynamics

We use the outputs of the FARGO-ADSG simulation as inputs for our dust code to investigate the dynamics of dust particles in disks with shadow-triggered spirals. The dust code is based on previous works by Paardekooper (2007) and Zsom et al. (2011). Every dust particle has a radial coordinate R and an azimuthal coordinate φ and has radial and azimuthal velocities of v_R and v_φ. The dust particles feel both, the gravitational potential from the star and from the disk. Furthermore, the particles are subject to aerodynamical drag from the gas. The equations of motion for the dust particles are given by

$$\frac{\partial R}{\partial t} = v_R \tag{5.9}$$

$$\frac{\partial \varphi}{\partial t} = \frac{L}{R^2} \tag{5.10}$$

$$\frac{\partial v_R}{\partial t} = \frac{L^2}{R^3} - \frac{\partial \Phi}{\partial R} + f_{\text{drag},R} \tag{5.11}$$

$$\frac{\partial L}{\partial t} = -\frac{\partial \Phi}{\partial \varphi} + R f_{\text{drag},\varphi}, \tag{5.12}$$

where L is the specific angular momentum and $f_{\text{drag},R}$ and $f_{\text{drag},\varphi}$ the drag forces in radial and azimuthal directions. Φ is the gravitational potential of both the star and the disk $\Phi = -GM_\star/R + \Phi_{\text{disk}}$. In principle, the disk's gravitational potential Φ_{disk} is the Fourier transform of the surface density Σ of the disk. The calculations of this are computationally expensive. Since FARGO-ADSG is already calculating the accelerations a_R and a_φ that arise due to the disk's self-gravity, we extract them from FARGO-ADSG and incorporate them into our dust code. This is important, since the disk's gravitational potential increases the orbital velocity of the gas compared to non self-gravitating disks. The larger the distance to the star, the more important is this effect. If we did not include the disk's potential, particles in the outer parts of the disk would orbit too slowly compared to the gas and would feel a constant tailwind. These particles would then gain angular momentum and would be expelled from the disk.

In general, equations (5.9) to (5.12) also have inertial forces that arise from the fact, that the FARGO-ADSG coordinate frame is always centered on the star and not on the center of mass. This introduces inertial forces that have to be taken into account. But, as seen in section 5.3, our disk is always perfectly symmetric, such that the center of mass will always be the center of the star. We can therefore neglect the inertial forces.

For the calculation of the drag forces we follow the approach of Woitke and Helling (2003) and Paardekooper (2007). The drag force is given by

$$\vec{f}_{\text{drag}} = -\frac{\Omega_{\text{K}}}{\text{St}}\Delta\vec{v}, \tag{5.13}$$

with the Keplerian frequency Ω_{K}, the particle's Stokes number St and the relative velocity between the dust and the gas $\Delta\vec{v} = \vec{v}_{\text{dust}} - \vec{v}_{\text{gas}}$. The Stokes number is given by

$$\text{St} = \sqrt{\frac{\pi}{2}}\frac{(3\text{Kn}+1)^2}{9\text{Kn}^2 + g_{\text{drag}} + 3\text{Kn}k_{\text{drag}}}\frac{a}{R}\frac{\xi_{\text{dust}}}{\rho_{\text{gas}}}\frac{v_{\text{K}}}{c_{\text{s}}}, \tag{5.14}$$

where $\text{Kn} = \lambda_{\text{mfp}}/a$ is the Knudsen number, λ_{mfp} the mean free path of the gas and a the radius of the dust particle. $\xi = 3.3\,\text{g/cm}^3$ is the bulk mass density of the dust particles, and ρ_{gas} the mid-plane mass density of the gas. g_{drag} and k_{drag} are the drag coefficients in the Epstein and in the Stokes drag regimes, respectively. They are given by

$$g_{\text{drag}} = \sqrt{1 + \frac{9\pi}{128}m^2} \tag{5.15}$$

and

$$k_{\text{drag}} = \begin{cases} 1 + 0.15\,\text{Re}^{0.687} & \text{if Re} < 500 \\ 3.96\times10^{-6}\,\text{Re}^{2.4} & \text{if } 500 < \text{Re} < 1500 \\ 0.11\,\text{Re} & \text{if Re} > 1500. \end{cases} \tag{5.16}$$

Re is the Reynolds number and given by

$$\text{Re} = 3\sqrt{\frac{\pi}{8}}\frac{m}{\text{Kn}}, \tag{5.17}$$

where $m = |\Delta\vec{v}|\,/c_{\text{s}}$ is the relative Mach number of the dust particles to the gas. This rather complex method for calculating the Stokes number has the advantage that it is automatically interpolating between the different drag regimes and is therefore more stable.

We use a symplectic, first-order leapfrog method to integrate equations (5.9) to (5.12). Equations containing the Stokes number are integrated implicitly. First, equations (5.9) and (5.10) are integrated using only half of a time step Δt

$$R_{\frac{1}{2}} = R_0 + \frac{\Delta t}{2} v_{R,0} \tag{5.18}$$

$$\varphi_{\frac{1}{2}} = \varphi_0 + \frac{\Delta t}{2} \frac{L_0}{R_0^2}. \tag{5.19}$$

Then, equations (5.11) and (5.12) are integrated with a full time step and using the new values $R_{\frac{1}{2}}$ and $\varphi_{\frac{1}{2}}$

$$v_{R,1} = \frac{v_{R,0} + \Delta t \left(\frac{L_0^2}{R_{\frac{1}{2}}^3} - \frac{\partial \Phi}{\partial R} + f_{\mathrm{acc},R} + \frac{v_{\mathrm{gas},R} \Omega_\mathrm{K}}{\mathrm{St}} \right)}{1 + \frac{\Delta t \Omega_\mathrm{K}}{\mathrm{St}}} \tag{5.20}$$

$$L_1 = \frac{L_0 + \Delta t \left(-\frac{\partial \Phi}{\partial \varphi} + R_{\frac{1}{2}} f_{\mathrm{acc},\varphi} + \frac{v_{\mathrm{gas},\varphi} R_{\frac{1}{2}} \Omega_\mathrm{K}}{\mathrm{St}} \right)}{1 + \frac{\Delta t \Omega_\mathrm{K}}{\mathrm{St}}}, \tag{5.21}$$

where $f_{\mathrm{acc},R}$ and $f_{\mathrm{acc},\varphi}$ are the gravitational accelerations in R and φ directions due to the gravitational potential of the disk extracted from FARGO-ADSG.

Finally, equations (5.9) and (5.10) are integrated again with half of a time step using L_1 and $v_{R,1}$

$$R_1 = R_{\frac{1}{2}} + \frac{\Delta t}{2} v_{R,1} \tag{5.22}$$

$$\varphi_1 = \varphi_{\frac{1}{2}} + \frac{\Delta t}{2} \frac{L_1}{R_{\frac{1}{2}}^2}. \tag{5.23}$$

In addition to that, a random walk of the dust particles is introduced to simulate turbulent diffusion of the dust. After every time step the particles are displaced by a length l_turb in a random direction. The distance of displacement is given by Youdin and Lithwick (2007) as

$$l_\mathrm{turb} = \Delta t \frac{\alpha H^2 \Omega_\mathrm{K}}{1 + \mathrm{St}^2}. \tag{5.24}$$

When needed, the FARGO-ADSG outputs of the gas surface density, the gas mid-plane temperature, the gas radial and azimuthal velocities, and the gravitational accelerations due to the self-gravity of the disk are used. Every quantity is linearly interpolated onto the location of the dust particle. To be stable, the particles perform several time steps between two FARGO-ADSG outputs. Between two outputs the gas

quantities are linearly interpolated in time. To be as precise as possible two consecutive FARGO-ADSG snapshots should not lie too far apart. For our simulation we use 4 000 FARGO-ADSG snapshots. This means, we have an output every 2.5 yrs of the simulation. Since our inner boundary is at 10 AU, particles on a Keplerian orbit at this radius orbit the star once every 30 years. This means, even in the worst case we have more than ten FARGO-ADSG snapshots per orbit. Since we are performing the dust simulations after the hydrodynamical simulations, we cannot implement any back reaction of the dust particles onto the gas.

We are using 100 000 dust particles with sizes between 1 μm and 1 m, which are initially distributed according the initial gas surface density.

Test Cases

To check whether the dust code is working properly we performed simulations of several test scenarios. In all cases we kept the gas parameters constant with a surface density of

$$\Sigma(R) = 1700 \frac{\mathrm{g}}{\mathrm{cm}^2} \times \left(\frac{R}{1\,\mathrm{AU}}\right)^{-1} \tag{5.25}$$

and a temperature profile of

$$T(R) = 150\,\mathrm{K} \times \left(\frac{R}{1\,\mathrm{AU}}\right)^{-\frac{1}{2}}. \tag{5.26}$$

The star has a mass of 1 $M_\odot$. The radial evolution of the dust particles is governed by

$$\frac{\partial}{\partial t} R = \frac{v_{\mathrm{gas},R}}{1+\mathrm{St}^2} - \frac{2 v_\mathrm{P}}{\mathrm{St}+\mathrm{St}^{-1}}, \tag{5.27}$$

where v_P is the maximum particle drift velocity caused by the sub-Keplerian gas as described in chapter 1. In a fixed gas disk, the particle's radial evolution is solely dependent on the particle's Stokes number.

To check whether the code is stable and correct for a broad variety of Stokes numbers, we performed four test scenarios. In three cases we kept the Stokes number of the particles constant at 10^{-100}, 10^{100} and 1. In the first case, the particles are completely coupled to the gas and are therefore being accreted with the radial gas velocity $v_{\mathrm{gas},R}$. In the second case, the particles are completely decoupled from the gas, are on Keplerian orbits and do not change their radial position. In the third case with $\mathrm{St} = 1$, the particles experience the maximum radial drift velocity of $\frac{1}{2} v_{\mathrm{gas},R} + v_\mathrm{P}$. We also performed a fourth test case where we did not fix the Stokes number at all. Here, the Stokes number will decrease with time as the particles drift to regions with higher surface densities.

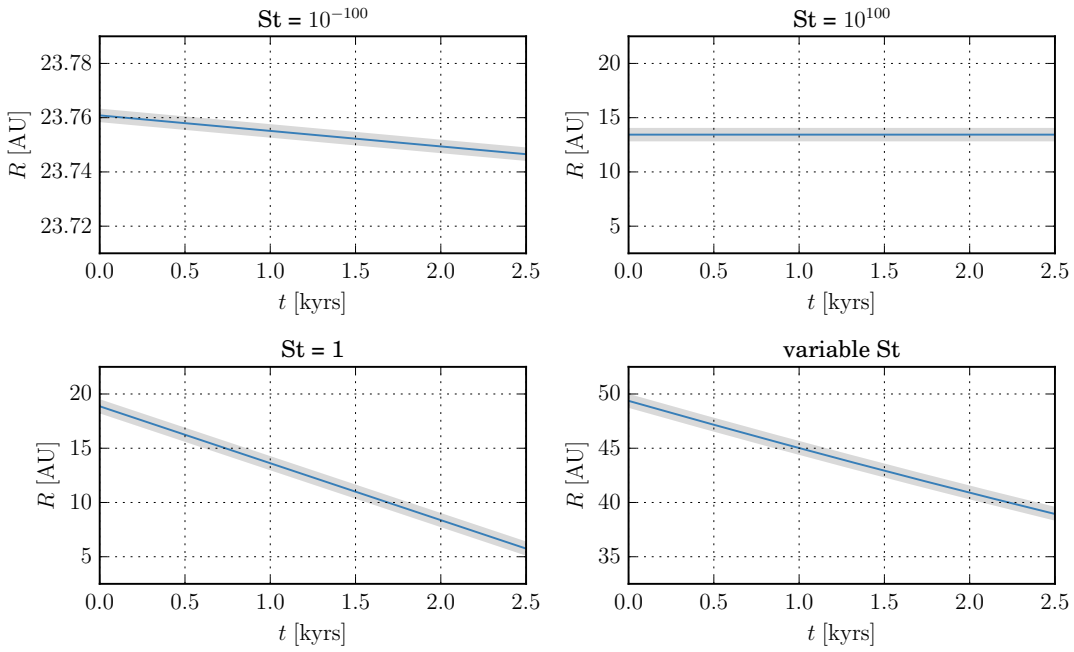

Figure 5.1: Test cases of the particle simulation. These plots compare the radial evolution of test particles in four different scenarios by using our dust code (blue lines) to the direct integration of equation (5.27) (gray lines) for four different cases of Stokes numbers: St $= 10^{-100}$ (top left), St $= 10^{100}$ (top right), St $= 1$ (bottom left), and for variable Stokes numbers (bottom right). The gas disk is not evolving in any of these cases.

Figure 5.1 shows the radial evolution of selected test particles in each of the four scenarios with blue lines. We also directly integrated equation (5.27) for all cases and overplotted the expected particle tracks with broad gray lines. The top left shows a particle with a very small Stokes number. It is perfectly coupled to the gas and is accreted with the radial gas velocity. The particle on the top right has a very high Stokes number and is therefore on an Keplerian orbit. Its radial position does not change at all. The particle on the bottom left has a Stokes number of unity and is accreted with the maximum drift velocity. Due to our choice of the surface density and temperature profiles, this drift velocity is constant with radial distance from the star. The gas velocity can be neglected here. The particle on the bottom right has a variable Stokes number that decreases with decreasing distance from the star due to higher surface densities in the inner disk. Therefore, the particle's radial velocity decreases slightly over time.

Both, the results from the particle simulation and the direct integration match perfectly. We therefore conclude, that the particle code is stable for all Stokes numbers and returns the correct results.

5.2.3 Radiative Transfer

To perform radiative transfer calculations with RADMC-3D we have to convert our discrete particles into one continuous three-dimensional dust density distribution for each particle size we want to include in the radiative transfer model. This is done as follows:

First, we spread all dust particles over a two-dimensional surface density grid with an exponential function

$$\Sigma_{\mathrm{dust},i}\left(\vec{R}\right) = \frac{m_i}{\pi D^2} \exp\left[\frac{\left(\vec{R}-\vec{R}_i\right)^2}{D^2}\right]. \tag{5.28}$$

$\Sigma_{\mathrm{dust},i}$ is the surface density one particle of mass m_i at location $\vec{R}_i$ contributes to the overall dust surface density. The factor $1/(\pi D^2)$ conserves the mass of the particle, but the overall surface density has to be gauged later nevertheless. As kernel size we use $D = 100\,\mathrm{AU}$. This seems to be large, but as seen in section 5.3, this is about the width of one spiral arm. Smaller values lead to noisy images.

For the RADMC-3D model setup we sort the particles into twelve particle size bins. Since we have particles between 1 μm and 1 mm, this leads to two bins per decade. We then sum the individual single-particle surface densities in twelve total dust surface densities according their size

$$\Sigma_{\mathrm{dust},j} = \sum_{\substack{i \\ a_{j,1}<a_i\leq a_{j,2}}} \Sigma_{\mathrm{dust},i}. \tag{5.29}$$

These surface densities are now vertically distributed with a Gaussian to get spatial mass densities according

$$\rho_{\mathrm{dust},j}\left(\vec{R},z\right) = \frac{\Sigma_{\mathrm{dust},j}\left(\vec{R}\right)}{\sqrt{2\pi}h_j} \exp\left[-\frac{z^2}{2h_j^2}\right], \tag{5.30}$$

with the dust scale height given by Birnstiel et al. (2010)

$$h_j = H \cdot \min\left(1, \sqrt{\frac{\alpha}{\min\left(\mathrm{St}_j, \frac{1}{2}\right)\left(1+\mathrm{St}_j^2\right)}}\right). \tag{5.31}$$

Since the combined mass of all our 100 000 dust particles is far too low for a typical protoplanetary disk, we multiply our densities now with a constant factor such that the total mass of the dust disk is $M_{\mathrm{dust}} = 2.5 \times 10^{-3}\,M_\odot$, which corresponds to a dust-to-gas ratio of about 10^{-2}.

We calculate the scattering and absorption opacities by using Mie theory and the BH-MIE code of Bohren and Huffman (1983) assuming the dust particles to be spherical. We use the optical constants taken from Dorschner et al. (1995) assuming the particles consist of pure pyroxene ($Mg_{0.7}Fe_{0.3}SiO_3$).

We modified RADMC-3D, such that no photons are sent from the star within 7.5° to the x-z-plane of the model to simulate the shadows that are cast by the inner inclined disk. The star has an effective temperature of $T_{\text{eff}} = 5\,700\,\text{K}$. The radiative transfer model is set up in spherical coordinates $(R,\ \varphi,\ \theta)$ with $N_R = 400$, $N_\varphi = 900$, and $N_\theta = 64$ grid points.

5.3 Results

Figure 5.2 shows the results of the hydrodynamical simulation. Shown are the gas surface density (top), the mid-plane gas temperature (second row), the pressure (third row), and the Toomre Q parameter of the gas at four different snapshots. The Toomre Q parameter is defined as

$$Q = \frac{c_s \kappa}{\pi G \Sigma} \tag{5.32}$$

and compares the strength of the thermal pressure to the gravity. κ is the epicyclic frequency

$$\kappa^2 = \frac{2\Omega}{R} \frac{\mathrm{d}}{\mathrm{d}R} \left(R^2 \Omega\right). \tag{5.33}$$

The disk is gravitationally stable, where $Q \gtrsim 1$. The red regions in the bottom panels of figure 5.2 are therefore the regions where the disk is gravitationally unstable. Usually, in simulations with gravitational unstable disks, one has to introduce a random noise initially to trigger the instabilities. In our case, however, the shadows trigger the instability without having to introduce any noise. Therefore, we always get two major spirals in the gas surface density as seen in the top panels of figure 5.2. The spirals, that arise from the gravitational collapse of the disk, grow stronger with time and expand slightly. Furthermore, a ring at 300 AU appears after about 9 000 yrs. This ring originates from the merging of two spirals located at opposite sites of the disk. In addition to that, the two large spirals split up in the outer part of the disk. This can be seen especially in the last snapshot. The exact mechanisms that leads to the formation of the ring and the *"forking"* of the spirals, however, are still unknown.

The shadows themselves can be seen in the temperature maps of figure 5.2 as slightly colder horizontal regions in the plots. The disk is colder here, since the stellar light is blocked by the shadows and cannot reach the disk. The cold regions are not exactly horizontal, because of the counter-clockwise rotation of the disk and a time delay due to radiative cooling. This effect can also be seen in the maps of the Toomre Q

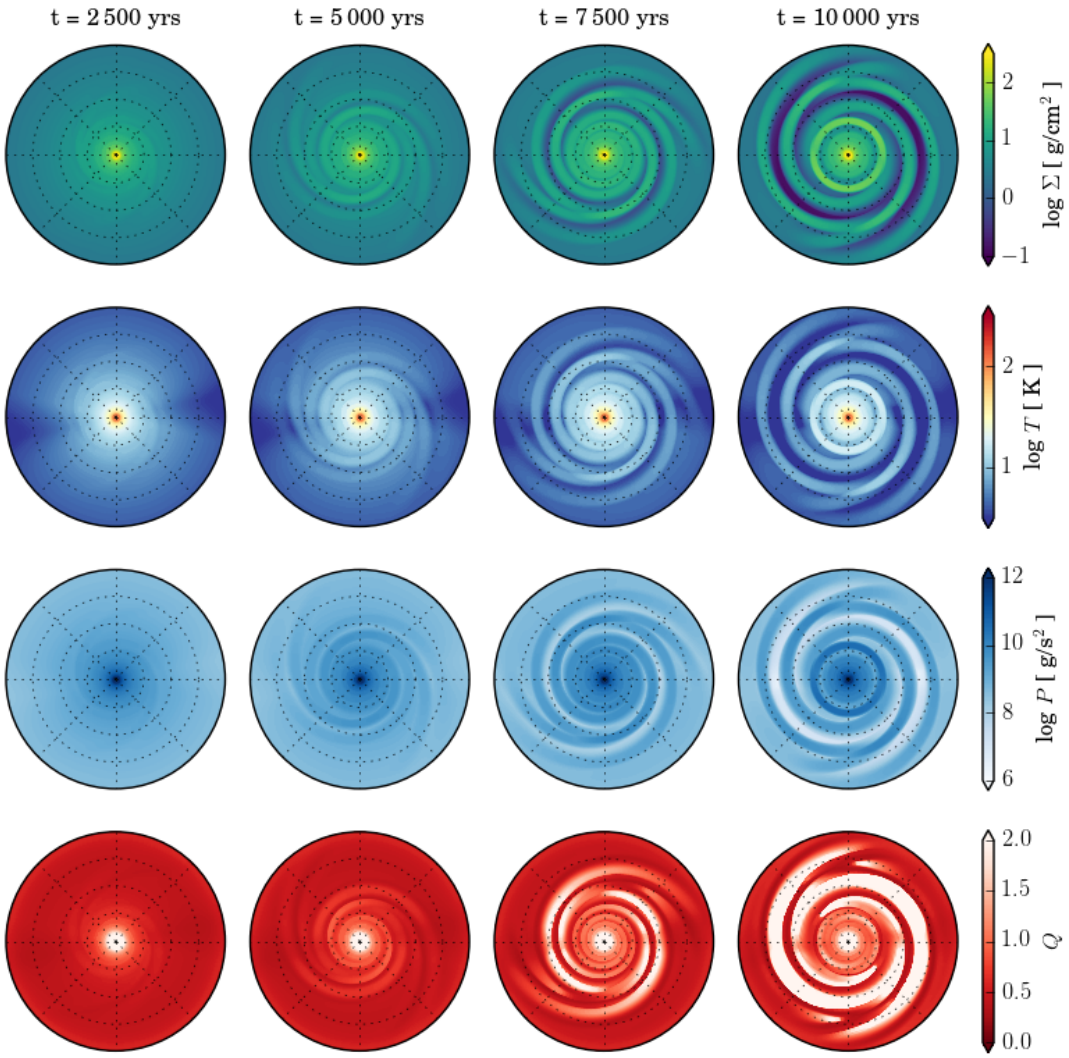

Figure 5.2: Snapshots of the gas surface density (top), the mid-plane gas temperature (second row), the gas pressure (third row), and the Toomre Q parameter (bottom) at four different snapshots of our simulations.

parameter. A colder disk is more likely to be gravitationally unstable. Therefore, the Q parameter is slightly smaller in the regions of the shadows. The spirals and the ring themselves are slightly warmer than the surrounding disk. Figure 5.2 also shows plots of the gas pressure. Note that it is the vertically integrated gas pressure as seen in equation (5.7). Hence, the units of g/s^2.

Figure 5.3 shows the results of the particle simulation. The left column shows the smallest particles with sizes of less than 100 μm, the second column intermediate size

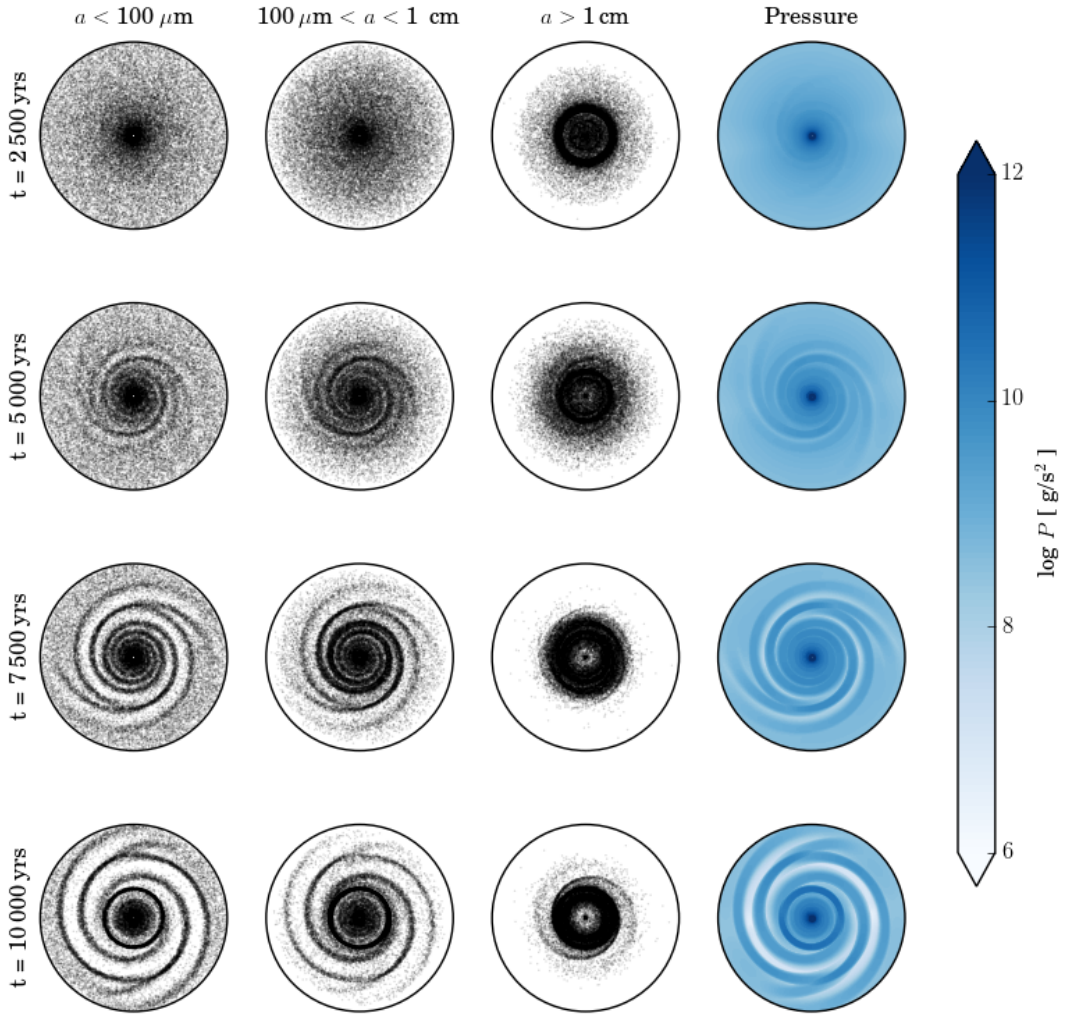

Figure 5.3: The distribution of micrometer-, millimeter-, and centimeter sized particles at four different snapshots of simulations compared to the pressure map of the gas.

particles between 100 μm and 1 cm, and the third column particles larger than 1 cm. The right column shows, in addition, the pressure maps of the gas to compare the location of the dust spirals with local pressure maxima.

The larger the particles, the larger their Stokes number. Initially, the majority of the particles have Stokes numbers smaller than one. Since the disk is very massive, the Stokes numbers are rather small. If this is the case, then the particles drift more rapidly, the larger they are. This can be seen in figure 5.3, as the larger the particles,

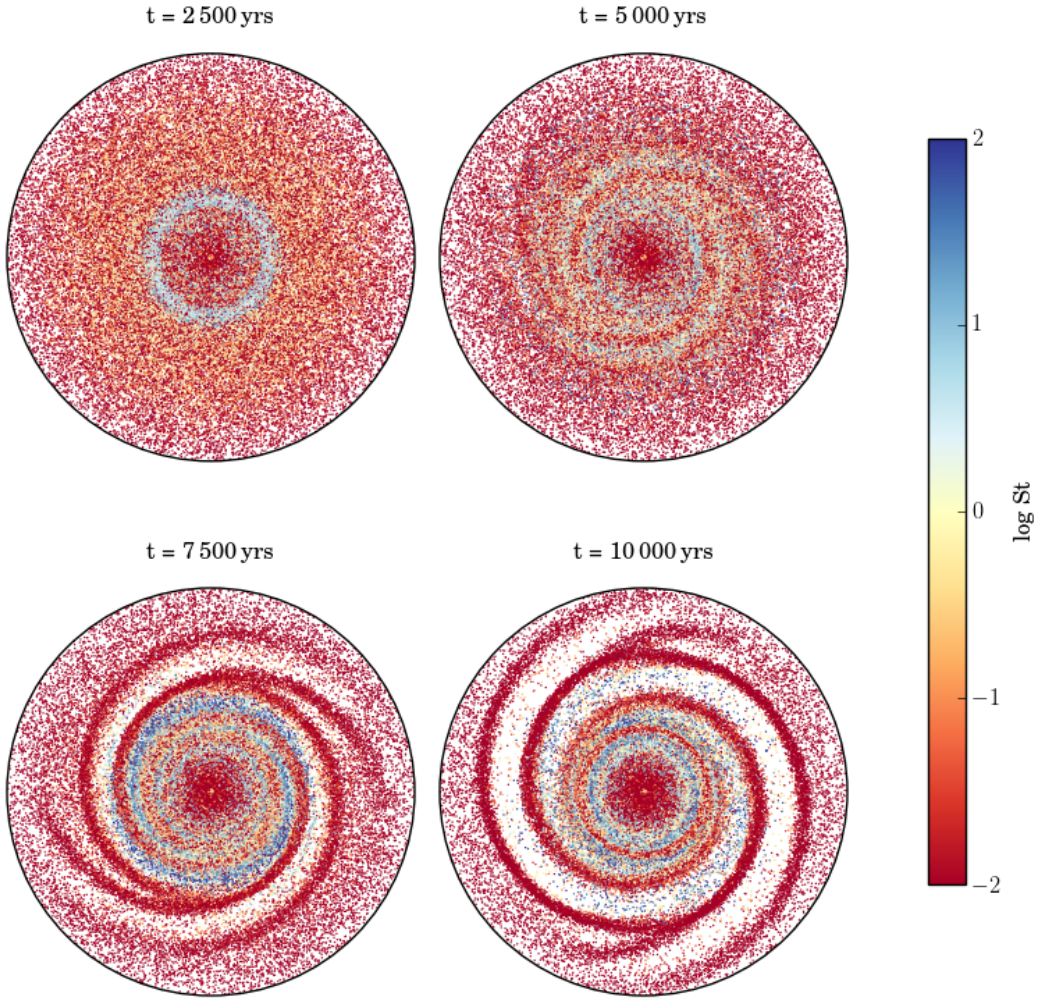

Figure 5.4: All particles, color-coded with their Stokes numbers, at four different snapshots of the simulation.

the more concentrated they are in the inner disk. By the end of the simulation after 10 000 yrs, the centimeter sized particles only exist in the inner 500 AU, while the micrometer sized particles are still distributed over the whole disk. The intermediate sized particles follow the spirals and the ring the best.

Figure 5.4 shows all particles combined, but color-coded with their Stokes numbers. In the beginning all particles have Stokes numbers smaller than unity, since the disk is very massive. After 1 000 yrs the larger particles with higher Stokes numbers are more concentrated towards the inner disk. In addition to that, a blue ring with particles

of high Stokes numbers can be seen. By comparing figure 5.4 with the Toomre Q parameter in figure 5.2, it can be seen that this ring of high Stokes numbers coincides with the transition of the gravitationally stable to the gravitationally unstable part of the disk. This is the region, where the gravitational collapse starts, which induces a spike in the radial velocity of the gas and therefore increases the relative velocities between the gas and the dust particles in this region. This effect is transient, as it is gone already in the next shown snapshot, but has temporarily an effect on the Stokes number.

In later snapshots, the particles in the spirals have low Stokes numbers due to the higher surface densities there, in contrast to the particles in the gaps between the spirals, which have high Stokes numbers. With time the gaps get depleted in particles, since they get eventually trapped in the spirals.

Figure 5.5 shows the intensity maps of our radiative transfer calculations at wavelengths of $\lambda = 1.3\,\mathrm{mm}$ (top) and $\lambda = 1.6\,\mu\mathrm{m}$ (bottom) in two configurations, face-one (left) and inclined (right). The inclination i and position angle θ are chosen to resemble the configuration of the disk around Elias 2-27. Note that $i > 180^\circ$ to invert the apparent rotational direction of the disk.

The snapshot chosen for the radiative transfer is at $t = 10\,000\,\mathrm{yrs}$. The images at $\lambda = 1.3\,\mathrm{mm}$ mostly trace the black-body radiation of millimeter sized particles. It is basically an image of the particles shown at the bottom of the second column of figure 5.3. In contrast to that, the images at $\lambda = 1.6\,\mu\mathrm{m}$ show stellar light that gets scattered by micrometer sized particles. It is therefore an image of the small particles shown in the bottom left plot of figure 5.3.

The shadows can be seen at both wavelengths. In the face-on images the shadows are exactly on the x-axis and not slightly off as seen in the temperature maps in figure 5.2. This is expected for the scattered light images at $\lambda = 1.6\,\mu\mathrm{m}$, since the stellar light cannot be scattered in the shadows. However, the millimeter emission is dependent on the particle temperature. Therefore, the shadows in the image should follow the low temperature regions in figure 5.2 and should be slightly off the x-axis. However, for the RADMC-3D images we used the dust temperature as calculated by the thermal Monte Carlo run. Since RADMC-3D is static and not time-dependent, it does not have any information about the rotating disk. Thus, the shadows and with them the low temperature regions fall exactly on the x-axis.

The small particles, that are traced in the scattered light images, are more evenly distributed throughout the disk. This is the reason why the spirals cannot be seen clearly. However, the gaps between the spirals can be seen as slightly darker regions in the images. In the gaps, there are less particles that could scatter the stellar light. Therefore, the disk appears darker here.

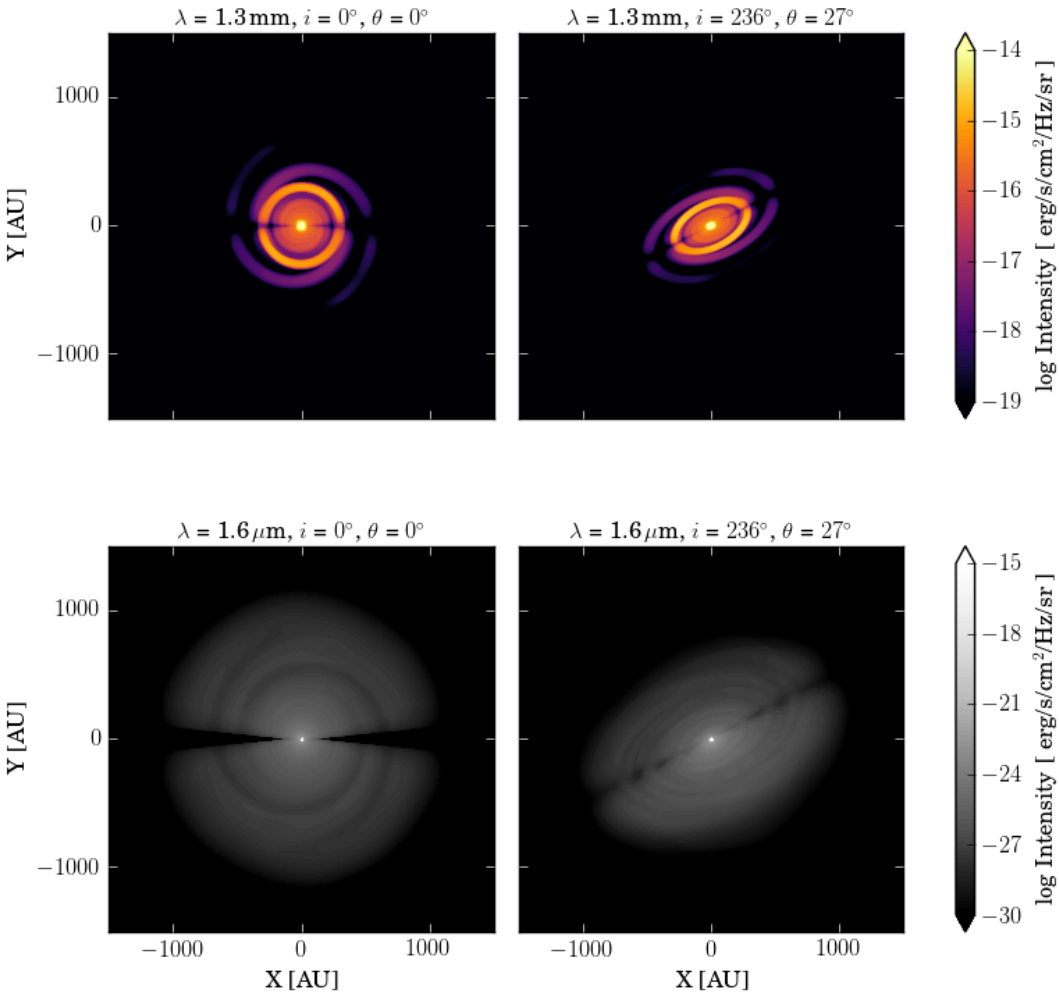

Figure 5.5: Intensity maps of the radiative transfer calculations after 10 000 yrs at millimeter wavelengths of $\lambda = 1.3\,\mathrm{mm}$ (top) and in scattered light at $\lambda = 1.6\,\mu\mathrm{m}$ (bottom), shown face-on (left) and inclined (right).

5.4 Discussion

As shown in the previous section, spiral density waves as induced by shadows cast onto a disk have an influence on the dynamics of dust particles in the disk. Shadows cast onto a gravitationally unstable protoplanetary disk, e.g. by a small inner inclined disk, trigger the formation of two major spiral waves. Dust particles in the disk are then affected by those density variations and tend to accumulate in local pressure

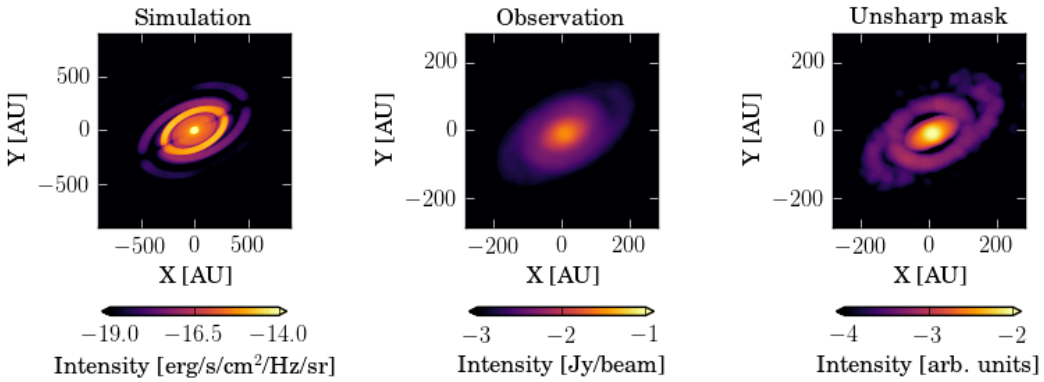

Figure 5.6: Comparison of the radiative transfer image at $\lambda = 1.3\,\text{mm}$ of our simulations (left) with the observations of Elias 2-27 by Pérez et al. (2016) (middle). The image on the right shows the observations with applied unsharp masking to enhance contrasts.

maxima. In later stages, smaller spirals originating from directly opposing points in the disk merge into a ring at about 300 AU. This ring is very efficient in trapping dust particles as seen in figure 5.3.

Radiative transfer images at a wavelength of $\lambda = 1.3\,\text{mm}$ show remarkable similarities to the observations of the disk around Elias 2-27 made by Pérez et al. (2016) shown in figure 5.6. Both, the simulations and the observations, show a bright ring and two major spirals emerging from the ring. However, one has to note that the scales are significantly different. The ring in Elias 2-27, which cannot be seen in the unprocessed image, is at about 120 AU, while the ring in our simulations is at 300 AU. The ring in our simulations seems to appear at the transition of the gravitationally stable to the gravitationally unstable disk. Increasing the surface density by a factor of two pushes the ring to about 150 AU.

Elias 2-27 has a mass of $(0.5 - 0.6)\,M_\odot$ (Natta et al., 2006, Andrews et al., 2010) and a disk with a mass of $(0.04 - 0.14)M_\odot$ (Isella et al., 2009, Andrews et al., 2010). This is a rather massive disk compared to the star. But even in simulations of the most optimistic case, we could not push the ring to 120 AU. Also, one has to note that Pérez et al. (2016) applied strong post-processing techniques, such as unsharp masking, to their observation to make the ring and the spirals visible. In unsharp masking a smoothed and scaled version of the image gets subtracted from the original image. This enhances contrasts. It is therefore unclear whether the ring is physical or only a result of the post-processing.

The observations of Pérez et al. (2016) do not show any kind of shadow that could have been cast by an inner inclined disk. However, the shadows in the millimeter image of our radiative transfer simulation are not as pronounced as in the scattered light

image. It could be possible that any existing shadow in the observation is unresolved. Tomida et al. (2017) could reproduce the observations of Pérez et al. (2016) only by three-dimensional magneto-hydrodynamic simulations of a gravitationally unstable disk without shadows. However, their simulations do not show any ring.

First synthetic ALMA observations of our radiative transfer image at $\lambda = 1.3\,\mathrm{mm}$ using CASA (McMullin et al., 2007) do not show any substructure in the disk, neither the ring nor the spirals. The reason for that is, that the spirals in our simulation are about three orders of magnitude fainter than the inner disk. Since the ALMA antennas are always picking up a small signal from the surrounding regions of the current pointing, the inner disk is always outshining the spirals.

The disks around HD 142527 and HD 100453, for example, are transitional disks with large inner cavities. Here the problem of a bright inner disk does not occur. More simulations with inner cavities are needed to investigate whether the spirals would be visible in such scenarios.

Furthermore, the disks around HD 142527 and HD 100453 show two shadows each, hinting to an inclined inner disk as assumed in our model. However, comparing our radiative transfer images in scattered light at $\lambda = 1.6\,\mu\mathrm{m}$ show some significant differences. The spirals in our model are less pronounced compared to the observations. The small micrometer sized particles that scatter the light are less concentrated in the spirals, especially in the outer disk.

Since our disk is very massive, the particles have in general small Stokes numbers, particularly the small particles. They are therefore well coupled to the gas and less likely to be trapped in spirals. Since we are only simulating the disk for 10 000 yrs there is simply not enough time for the small particles in the outer disk to be trapped in the spirals.

Simulating the disk for a prolonged time is problematic for two reasons. First, we already have to save 4 000 FARGO-ADSG snapshots for the current simulation, which is very memory consuming. More snapshots require even more memory. And second, after about 15 000 years the outer boundary induces artifacts in the disk due to reflections. Simulations past this point would require to set the outer boundary at even greater distances. Keeping the grid resolution constant would increase the file sizes even more heavily and is not feasible at the moment.

5.5 Conclusion

Shadows cast onto protoplanetary disks induce spiral density waves and rings in the gas disk. Dust particles can be trapped in these spirals and rings depending on their size. These spirals and rings can be seen in radiative transfer simulations in scattered light and in millimeter emission. However, it is unclear, whether they can actually be observed with ALMA, since the bright inner disk outshines the spirals in the outer

disk. Future simulations of transitional disks with large inner cavities will try to answer this question.

The dust spirals of our simulation seen in scattered light are less pronounced compared to observations. The simulation time is not long enough to accumulate the small micrometer sized particles, that are seen in scattered light, in the spirals in the outer disk. We will perform longer simulations to investigate whether the small particles are trapped in the spirals at later times.

We did not include dust growth and fragmentation in the model, whose typical timescales in the region of interest exceed the simulations time and can therefore be neglected. For future simulations with longer simulation times we aim to include simplified coagulation and fragmentation models.

Debes et al. (2017) discovered in observations of TW Hydrae moving azimuthal brightness asymmetries, that could be consistent with an inner inclined and precessing disk. The shadows in our model are static. In future works we aim to investigate the influence of moving shadows cast onto the disk by a precessing inclined inner disk or by a close-in orbiting optically thick clump.

Furthermore, our dust particle code can be extended way beyond the scope of this work. The dust code works for all kinds of FARGO-ADSG scenarios. It is easy to modify the particle code to allow for planets by adding the gravitational potential of the planet and the inertial forces that arise from the movement of the center of mass.

It is also straightforward to modify the particle code to allow for simulations with FARGO3D data, the three-dimensional version of FARGO. Here we can track the three-dimensional motion of the particles in the disk. This is of special interest when looking at the accretion of dust onto planets and circumplanetary disks. Furthermore, we can add more physics such as photophoresis, to check whether particles close to the star can be launched and expelled from the disk and can be re-accreted later.

We can track not only the position and velocities of the particles, but also their temperature. By looking at the thermal history of the particles we can investigate, whether the passage through density and temperature enhancements, such as spiral waves caused by gravitational instabilities or planets, is strong enough to crystallize ice or silicate particles, or even evaporate them. In the extreme case this could be interesting for chondrule formation, when the temperatures are temporarily hot enough to crystallize silicate material. This will be part of future investigations.

6

Summary and Outlook

Planets are formed out of dust in protoplanetary disks. The exact mechanism, however, how micrometer sized dust grains are transformed into large planets with sizes of several thousands of kilometers is still unknown. Several barriers hinder collisional dust growth above certain sizes, such as the fragmentation barrier and the drift barrier. In the first one, the dust particles rather fragment in collision than grow to larger sizes, while in the latter one the radial drift timescale is shorter than the growth timescale, causing the particles to be accreted onto the star. The maximum particle sizes are therefore limited to a few decimeters to meters depending on their location in the disk. Several models have been proposed to overcome these barriers, for example, planetesimal formation in dust accumulations due to the streaming instability.

Ice lines are also thought to affect dust growth in protoplanetary disks. Of special interest is hereby the water ice line. Water ice particles are supposed to be more sticky than silicate particles due to a higher surface energy. Therefore, dust particles covered with water ice can withstand higher collision velocities than pure silicate dust. These particles can then grow to larger sizes. The four giant planets in the solar system are all in the outer part beyond 5 AU, while the small and rocky terrestrial planets occupy the inner part. This might hint to the fact, that something changed in the disk between Mars and Jupiter, where the water ice line could have been. Simulations predicted that the fragmentation velocity of water ice is in the order of 50 m/s (Wada et al., 2009), while experiments showed smaller fragmentation velocities of 10 m/s (Gundlach and Blum, 2015). Water ice covered particles could therefore break through the fragmentation barrier, or could at least grow to larger sizes, which makes it more likely to trigger the streaming instability.

Ice lines, in general, are important for the chemical composition of planets. Outside of an ice line, the volatile species is frozen out as ice on the dust. This changes the chemical composition of dust particles depending on their location relative to ice lines in protoplanetary disks. Espinoza et al. (2016) showed that the C/O ratios of a sample of giant planet atmospheres rather follow the C/O ratio of the dust and not the one

of the gas. This suggests, that giant planets accrete a significant fraction of their mass from the dust. It is therefore important to understand how volatiles are transported in protoplanetary disks and how ice lines affect the distribution of the volatiles.

In chapter 2, we developed a dust coagulation and disk evolution model, that can trace the distribution of one additional volatile species. We focused hereby on the CO ice line and assumed that the collisional physics of the dust particles do not change across the ice line. Inside the ice line, the CO is transported in the gas phase via viscous accretion and diffusion. Outside the ice line, all of the CO is frozen out on the dust particles and it transported inwards via radial drift of the dust. When particles drift through the ice line and the CO evaporates, vapor gets deposited at the ice line. From here the CO vapor gets transported in the gas phase and can also diffuse back through the ice line, where it can recondense on the dust particles. We showed that the CO ice fraction of dust particles is enhanced in a region shortly outside of ice lines due to the effect of recondensation. The smaller the particles the larger is the volatile enhancement. Due to the inwards migration of CO on dust particles, the inner disk gets enhanced in CO. This process is highly dependent on the disk properties. In disks with low turbulence and low accretion, the CO vapor accumulates at the ice line. This brings evaporation in saturation and can push the CO ice line closer to the star. With higher gas accretion velocities, the CO gas can be transported inwards, which enhances the inner disk in CO. In cases of very high turbulence, the CO gas can diffuse outwards from the ice line fast than it can recondense. Here, the inner disk is not enhanced in CO. Depending on the disk properties the CO ice line can change its position by about 10 AU without changing the temperature profile.

In chapter 3, we included fragmentation into the dust coagulation model, that was previously neglected in chapter 2. This reduces the maximum particle sizes and therefore the drift efficiency. The transport and accumulation of CO at the ice line is therefore less enhanced compared to the result in chapter 2. But still, the particles shortly outside of the ice line are enhanced in CO. The smaller the particles, the larger is their CO ice fraction, since the backwards diffusing vapor predominantly recondenses on small particles, because they contribute most to the total surface area. This increases the size of the smallest particles, the monomers. Dominik and Tielens (1997) showed that the fragmentation velocity is inversely proportional to the monomer size. The fragmentation velocity is therefore reduced in the recondensation region outside of the ice line, leading to on average smaller particle sizes. Since smaller particles drift less efficiently, this causes a traffic jam of dust particles, and thus, enhancing the dust surface density just outside of ice lines. This traffic jam can be seen as ring-like, axis-symmetric emission features in observations of protoplanetary disks. This effect is, in principle, universal for any ice line. But we could show, that only the most abundant molecules, such as H_2O, CO_2, or CO, are abundant enough to produce a visible enhancement in the dust surface density. We also showed that the overall gas surface density is not affected by the ice line. This can help to distinguish the different formation scenarios of rings and gaps in protoplanetary disks. Dust gaps caused by planets are depleted in gas, while gaps caused by ice lines do not show features in the gas. Isella et al.

(2016) presented observations of dust and gas in the disk around HD 163296, which show three gaps in the dust. The two outer gaps also show depletions in the gas that are consistent with gap opening by planets. The inner gap, however, could also be consistent with no gap at all in the gas and is therefore a candidate for gap formation by a different process than planets.

As a next step, it would be interesting to investigate the water ice line and more advanced collision models in more detail. Here, the collisional physics of the dust particles change. The particles outside the water ice line are expected to have higher fragmentation velocities and can therefore grow to larger sizes. When they cross the ice line, they lose their water ice content and therefore the high fragmentation velocities. However, depending on the disk conditions and the assumed fragmentation velocities, the particles outside the water ice line could be one to two orders of magnitude larger than the particles inside the water ice line. Therefore, they drift more rapidly and can potentially drift significant distances beyond the water ice line, before their water ice content evaporates completely and they start to fragment. In that case, they are embedded in small silicate particles and might grow to planetesimals by sweep-up growth as proposed by Windmark et al. (2012a).

In future works, we plan to implement multiple ice lines to predict the radial dependency of the C/O ratio of dust in protoplanetary disk in more detail. Since the C/O ratio of giant planet atmospheres depend on the C/O ratio of the dust they accreted, this prediction can help to identify the location of formation of giant exoplanets that might have migrated from their original position. Furthermore, it would be very interesting to extend the model to two dimensions to investigate vertical ice lines and how volatiles are distributed in the atmospheres of protoplanetary disks.

In chapter 4 we revisited the formation model of chondrules in shock waves. We implemented proper downstream boundaries conditions, that are consistent with the upstream conditions. In this case, it is not possible to form chondrules, because the peak temperature cannot reach the required minimum temperature to fully melt the chondrule precursors, while at the same time the post shock temperature is low enough to retain the volatile species in the chondrules. We also investigated vertical energy loss in more realistic disks by introducing an energy loss rate to account for radiative diffusion. Even in this case the post shock cooling is not strong enough to be consistent with chondrule formation, even in unrealistically thin disks. In optically thin shocks, on the other hand, the thermal histories of the particles are consistent with the requirements on chondrules formation, however, the cooling rates are too high to explain the observed textures in chondrules. We also used the optical thin shock models to investigate the influence of low velocity shock on water ice particles in protoplanetary disks. Relatively low shocks with Mach numbers of about two are able to partially of fully crystallize water ice particles. This could be important in the context of observations made by McClure et al. (2015), who found crystallized ice particles beyond 30 AU around T Tauri disks, at distances that are typically too cold to explain crystallized ices. Shocks could explain the formation of ice crystals at these distances.

The source of the shocks, however, is unknown. We also showed that shocks of certain velocities can evaporate small water ice particles, while retain larger particles. In the shock showed in section 4.3.4, only particles larger than 10 μm survived. This, in turn, can have an effect on the fragmentation velocity as described in chapter 3, where the fragmentation velocity depends on the size of the smallest particles.

In chapter 5 we investigated the influence of shadows cast on protoplanetary disks on the transport of dust particles. Several observations of disks in scattered light showed shadows. Marino et al. (2015) showed that the shadows cast on the disk around HD 142527 are consistent with being cast by an inner inclined disk. Montesinos et al. (2016) showed in hydrodynamical simulations that these shadows can trigger spiral waves and rings in gravitationally unstable disks. We used these hydrodynamical simulations to investigate the dynamics of the dust that is affected by pressure gradients. We showed that the dust particles are accumulated in the spirals and the ring in the gas imposed by the shadows. Radiative transfer calculations at millimeter wavelengths are similar to observations of Elias 2-27 made by Pérez et al. (2016), that also show a dust ring and spirals. In future works, we plan to investigate the influence of moving shadows, that are produced, for example, if the inner disks, that casts the shadows, is precessing, or by optically thick dust clumps that orbit the star and cast shadows on the outer disk.

Bibliography

Adachi, I., Hayashi, C., and Nakazawa, K. (1976). The gas drag effect on the elliptical motion of a solid body in the primordial solar nebula. *Progress of Theoretical Physics*, 56:1756–1771.

Alexander, R. D., Clarke, C. J., and Pringle, J. E. (2006). Photoevaporation of protoplanetary discs - II. Evolutionary models and observable properties. MNRAS, 369:229–239.

Ali-Dib, M., Mousis, O., Petit, J.-M., and Lunine, J. I. (2014). The Measured Compositions of Uranus and Neptune from their Formation on the CO Ice Line. ApJ, 793:9.

ALMA Partnership, Brogan, C. L., Pérez, L. M., Hunter, T. R., Dent, W. R. F., Hales, A. S., Hills, R. E., Corder, S., Fomalont, E. B., Vlahakis, C., Asaki, Y., Barkats, D., Hirota, A., Hodge, J. A., Impellizzeri, C. M. V., Kneissl, R., Liuzzo, E., Lucas, R., Marcelino, N., Matsushita, S., Nakanishi, K., Phillips, N., Richards, A. M. S., Toledo, I., Aladro, R., Broguiere, D., Cortes, J. R., Cortes, P. C., Espada, D., Galarza, F., Garcia-Appadoo, D., Guzman-Ramirez, L., Humphreys, E. M., Jung, T., Kameno, S., Laing, R. A., Leon, S., Marconi, G., Mignano, A., Nikolic, B., Nyman, L.-A., Radiszcz, M., Remijan, A., Rodón, J. A., Sawada, T., Takahashi, S., Tilanus, R. P. J., Vila Vilaro, B., Watson, L. C., Wiklind, T., Akiyama, E., Chapillon, E., de Gregorio-Monsalvo, I., Di Francesco, J., Gueth, F., Kawamura, A., Lee, C.-F., Nguyen Luong, Q., Mangum, J., Pietu, V., Sanhueza, P., Saigo, K., Takakuwa, S., Ubach, C., van Kempen, T., Wootten, A., Castro-Carrizo, A., Francke, H., Gallardo, J., Garcia, J., Gonzalez, S., Hill, T., Kaminski, T., Kurono, Y., Liu, H.-Y., Lopez, C., Morales, F., Plarre, K., Schieven, G., Testi, L., Videla, L., Villard, E., Andreani, P., Hibbard, J. E., and Tatematsu, K. (2015). The 2014 ALMA Long Baseline Campaign: First Results from High Angular Resolution Observations toward the HL Tau Region. ApJ, 808:L3.

Andrews, S. M., Wilner, D. J., Hughes, A. M., Qi, C., and Dullemond, C. P. (2010). Protoplanetary Disk Structures in Ophiuchus. II. Extension to Fainter Sources. ApJ, 723:1241–1254.

Andrews, S. M., Wilner, D. J., Zhu, Z., Birnstiel, T., Carpenter, J. M., Pérez, L. M., Bai, X.-N., Öberg, K. I., Hughes, A. M., Isella, A., and Ricci, L. (2016). Ringed Substructure and a Gap at 1 au in the Nearest Protoplanetary Disk. ApJ, 820:L40.

Aumatell, G. and Wurm, G. (2011). Breaking the ice: planetesimal formation at the snowline. MNRAS, 418:L1–L5.

Bai, X.-N. and Stone, J. M. (2010). Dynamics of Solids in the Midplane of Protoplanetary Disks: Implications for Planetesimal Formation. ApJ, 722:1437–1459.

Balbus, S. A. and Hawley, J. F. (1991). A powerful local shear instability in weakly magnetized disks. I - Linear analysis. II - Nonlinear evolution. ApJ, 376:214–233.

Baruteau, C. and Masset, F. (2008). Type I Planetary Migration in a Self-Gravitating Disk. ApJ, 678:483–497.

Bauer, I., Finocchi, F., Duschl, W. J., Gail, H.-P., and Schloeder, J. P. (1997). Simulation of chemical reactions and dust destruction in protoplanetary accretion disks. A&A, 317:273–289.

Baumgardt, H. and Kroupa, P. (2007). A comprehensive set of simulations studying the influence of gas expulsion on star cluster evolution. MNRAS, 380:1589–1598.

Bell, K. R., Cassen, P. M., Klahr, H. H., and Henning, T. (1997). The Structure and Appearance of Protostellar Accretion Disks: Limits on Disk Flaring. ApJ, 486:372–387.

Benisty, M., Juhasz, A., Boccaletti, A., Avenhaus, H., Milli, J., Thalmann, C., Dominik, C., Pinilla, P., Buenzli, E., Pohl, A., Beuzit, J.-L., Birnstiel, T., de Boer, J., Bonnefoy, M., Chauvin, G., Christiaens, V., Garufi, A., Grady, C., Henning, T., Huelamo, N., Isella, A., Langlois, M., Ménard, F., Mouillet, D., Olofsson, J., Pantin, E., Pinte, C., and Pueyo, L. (2015). Asymmetric features in the protoplanetary disk MWC 758. A&A, 578:L6.

Benisty, M., Stolker, T., Pohl, A., de Boer, J., Lesur, G., Dominik, C., Dullemond, C. P., Langlois, M., Min, M., Wagner, K., Henning, T., Juhasz, A., Pinilla, P., Facchini, S., Apai, D., van Boekel, R., Garufi, A., Ginski, C., Ménard, F., Pinte, C., Quanz, S. P., Zurlo, A., Boccaletti, A., Bonnefoy, M., Beuzit, J. L., Chauvin, G., Cudel, M., Desidera, S., Feldt, M., Fontanive, C., Gratton, R., Kasper, M., Lagrange, A.-M., LeCoroller, H., Mouillet, D., Mesa, D., Sissa, E., Vigan, A., Antichi, J., Buey, T., Fusco, T., Gisler, D., Llored, M., Magnard, Y., Moeller-Nilsson, O., Pragt, J., Roelfsema, R., Sauvage, J.-F., and Wildi, F. (2017). Shadows and spirals in the protoplanetary disk HD 100453. A&A, 597:A42.

Birnstiel, T., Dullemond, C. P., and Brauer, F. (2009). Dust retention in protoplanetary disks. A&A, 503:L5–L8.

Birnstiel, T., Dullemond, C. P., and Brauer, F. (2010). Gas- and dust evolution in protoplanetary disks. A&A, 513:A79.

Birnstiel, T., Klahr, H., and Ercolano, B. (2012). A simple model for the evolution of the dust population in protoplanetary disks. A&A, 539:A148.

Blum, J. and Münch, M. (1993). Experimental investigations on aggregate-aggregate collisions in the early solar nebula. Icarus, 106:151.

Blum, J. and Wurm, G. (2008). The Growth Mechanisms of Macroscopic Bodies in Protoplanetary Disks. ARA&A, 46:21–56.

Bohren, C. F. and Huffman, D. R. (1983). *Absorption and scattering of light by small particles*.

Boley, A. C. and Durisen, R. H. (2008). Gravitational Instabilities, Chondrule Formation, and the FU Orionis Phenomenon. ApJ, 685:1193–1209.

Brauer, F., Dullemond, C. P., and Henning, T. (2008). Coagulation, fragmentation and radial motion of solid particles in protoplanetary disks. A&A, 480:859–877.

Briceño, C., Luhman, K. L., Hartmann, L., Stauffer, J. R., and Kirkpatrick, J. D. (2002). The Initial Mass Function in the Taurus Star-forming Region. ApJ, 580:317–335.

Brown, P. N., Byrne, G. D., and Hindmarsh, A. C. (1989). VODE: A variable-coefficient ODE Solver. *SIAM Journal on Scientific Computing*, 10:1038–1051.

Brucker, M. J., Grundy, W. M., Stansberry, J. A., Spencer, J. R., Sheppard, S. S., Chiang, E. I., and Buie, M. W. (2009). High albedos of low inclination Classical Kuiper belt objects. Icarus, 201:284–294.

Bryden, G., Chen, X., Lin, D. N. C., Nelson, R. P., and Papaloizou, J. C. B. (1999). Tidally Induced Gap Formation in Protostellar Disks: Gap Clearing and Suppression of Protoplanetary Growth. ApJ, 514:344–367.

Cassan, A., Kubas, D., Beaulieu, J.-P., Dominik, M., Horne, K., Greenhill, J., Wambsganss, J., Menzies, J., Williams, A., Jørgensen, U. G., Udalski, A., Bennett, D. P., Albrow, M. D., Batista, V., Brillant, S., Caldwell, J. A. R., Cole, A., Coutures, C., Cook, K. H., Dieters, S., Prester, D. D., Donatowicz, J., Fouqué, P., Hill, K., Kains, N., Kane, S., Marquette, J.-B., Martin, R., Pollard, K. R., Sahu, K. C., Vinter, C., Warren, D., Watson, B., Zub, M., Sumi, T., Szymański, M. K., Kubiak, M., Poleski, R., Soszynski, I., Ulaczyk, K., Pietrzyński, G., and Wyrzykowski, Ł. (2012). One or more bound planets per Milky Way star from microlensing observations. Nature, 481:167–169.

Cherchneff, I., Barker, J. R., and Tielens, A. G. G. M. (1992). Polycyclic aromatic hydrocarbon formation in carbon-rich stellar envelopes. ApJ, 401:269–287.

Chiang, E. I. and Goldreich, P. (1997). Spectral Energy Distributions of T Tauri Stars with Passive Circumstellar Disks. ApJ, 490:368–376.

Ciesla, F. J. and Hood, L. L. (2002). The Nebular Shock Wave Model for Chondrule Formation: Shock Processing in a Particle-Gas Suspension. Icarus, 158:281–293.

Connelly, J. N., Bizzarro, M., Krot, A. N., Nordlund, Å., Wielandt, D., and Ivanova, M. A. (2012). The Absolute Chronology and Thermal Processing of Solids in the Solar Protoplanetary Disk. *Science*, 338:651.

Cuzzi, J. N. and Zahnle, K. J. (2004). Material Enhancement in Protoplanetary Nebulae by Particle Drift through Evaporation Fronts. ApJ, 614:490–496.

Debes, J. H., Poteet, C. A., Jang-Condell, H., Gaspar, A., Hines, D., Kastner, J. H., Pueyo, L., Rapson, V., Roberge, A., Schneider, G., and Weinberger, A. J. (2017). Chasing Shadows: Rotation of the Azimuthal Asymmetry in the TW Hya Disk. ApJ, 835:205.

Desch, S. J. (2007). Mass Distribution and Planet Formation in the Solar Nebula. ApJ, 671:878–893.

Desch, S. J. and Connolly, Jr., H. C. (2002). A model of the thermal processing of particles in solar nebula shocks: Application to the cooling rates of chondrules. *Meteoritics and Planetary Science*, 37:183–207.

Desch, S. J., Morris, M. A., Connolly, H. C., and Boss, A. P. (2012). The importance of experiments: Constraints on chondrule formation models. *Meteoritics and Planetary Science*, 47:1139–1156.

Dittrich, K., Klahr, H., and Johansen, A. (2013). Gravoturbulent Planetesimal Formation: The Positive Effect of Long-lived Zonal Flows. ApJ, 763:117.

Dominik, C. and Tielens, A. G. G. M. (1997). The Physics of Dust Coagulation and the Structure of Dust Aggregates in Space. ApJ, 480:647–673.

Dorschner, J., Begemann, B., Henning, T., Jaeger, C., and Mutschke, H. (1995). Steps toward interstellar silicate mineralogy. II. Study of Mg-Fe-silicate glasses of variable composition. A&A, 300:503.

Drążkowska, J. and Dullemond, C. P. (2014). Can dust coagulation trigger streaming instability? A&A, 572:A78.

Drążkowska, J., Windmark, F., and Dullemond, C. P. (2013). Planetesimal formation via sweep-up growth at the inner edge of dead zones. A&A, 556:A37.

Duffell, P. C. and MacFadyen, A. I. (2013). Gap Opening by Extremely Low-mass Planets in a Viscous Disk. ApJ, 769:41.

Dullemond, C. P. and Dominik, C. (2004). The effect of dust settling on the appearance of protoplanetary disks. A&A, 421:1075–1086.

Dullemond, C. P., Juhasz, A., Pohl, A., Sereshti, F., Shetty, R., Peters, T., Commercon, B., and Flock, M. (2016). RADMC-3D v0.40. http://radmc3d.ita.uni-heidelberg.de/.

Espinoza, N., Fortney, J., Miguel, Y., Thorngren, D., and Murray-Clay, R. (2016). Metal enrichment leads to low atmospheric C/O ratios in transiting giant exoplanets. *ArXiv e-prints*.

Fedkin, A. V., Grossman, L., Ciesla, F. J., and Simon, S. B. (2012). Mineralogical and isotopic constraints on chondrule formation from shock wave thermal histories. Geochim. Cosmochim. Acta, 87:81–116.

Follette, K. B., Grady, C. A., Swearingen, J. R., Sitko, M. L., Champney, E. H., van der Marel, N., Takami, M., Kuchner, M. J., Close, L. M., Muto, T., Mayama, S., McElwain, M. W., Fukagawa, M., Maaskant, K., Min, M., Russell, R. W., Kudo, T., Kusakabe, N., Hashimoto, J., Abe, L., Akiyama, E., Brandner, W., Brandt, T. D., Carson, J., Currie, T., Egner, S. E., Feldt, M., Goto, M., Guyon, O., Hayano, Y., Hayashi, M., Hayashi, S., Henning, T., Hodapp, K., Ishii, M., Iye, M., Janson, M., Kandori, R., Knapp, G. R., Kuzuhara, M., Kwon, J., Matsuo, T., Miyama, S., Morino, J.-I., Moro-Martin, A., Nishimura, T., Pyo, T.-S., Serabyn, E., Suenaga, T., Suto, H., Suzuki, R., Takahashi, Y., Takato, N., Terada, H., Thalmann, C., Tomono, D., Turner, E. L., Watanabe, M., Wisniewski, J. P., Yamada, T., Takami, H., Usuda, T., and Tamura, M. (2015). SEEDS Adaptive Optics Imaging of the Asymmetric Transition Disk Oph IRS 48 in Scattered Light. ApJ, 798:132.

Frank, J., King, A., and Raine, D. J. (2002). *Accretion Power in Astrophysics: Third Edition*.

Fukagawa, M., Tamura, M., Itoh, Y., Kudo, T., Imaeda, Y., Oasa, Y., Hayashi, S. S., and Hayashi, M. (2006). Near-Infrared Images of Protoplanetary Disk Surrounding HD 142527. ApJ, 636:L153–L156.

Gail, H.-P. (2001). Radial mixing in protoplanetary accretion disks. I. Stationary disc models with annealing and carbon combustion. A&A, 378:192–213.

Garaud, P., Meru, F., Galvagni, M., and Olczak, C. (2013). From Dust to Planetesimals: An Improved Model for Collisional Growth in Protoplanetary Disks. ApJ, 764:146.

Garufi, A., Quanz, S. P., Schmid, H. M., Mulders, G. D., Avenhaus, H., Boccaletti, A., Ginski, C., Langlois, M., Stolker, T., Augereau, J.-C., Benisty, M., Lopez, B., Dominik, C., Gratton, R., Henning, T., Janson, M., Ménard, F., Meyer, M. R., Pinte, C., Sissa, E., Vigan, A., Zurlo, A., Bazzon, A., Buenzli, E., Bonnefoy, M., Brandner, W., Chauvin, G., Cheetham, A., Cudel, M., Desidera, S., Feldt, M., Galicher, R., Kasper, M., Lagrange, A.-M., Lannier, J., Maire, A. L., Mesa, D., Mouillet, D., Peretti, S., Perrot, C., Salter, G., and Wildi, F. (2016). The SPHERE view of the planet-forming disk around HD 100546. A&A, 588:A8.

Goldreich, P. and Tremaine, S. (1979). The excitation of density waves at the Lindblad and corotation resonances by an external potential. ApJ, 233:857–871.

Gombosi, T. I., Nagy, A. F., and Cravens, T. E. (1986). Dust and neutral gas modeling of the inner atmospheres of comets. *Reviews of Geophysics*, 24:667–700.

Grady, C. A., Muto, T., Hashimoto, J., Fukagawa, M., Currie, T., Biller, B., Thalmann, C., Sitko, M. L., Russell, R., Wisniewski, J., Dong, R., Kwon, J., Sai, S., Hornbeck, J., Schneider, G., Hines, D., Moro Martín, A., Feldt, M., Henning, T., Pott, J.-U., Bonnefoy, M., Bouwman, J., Lacour, S., Mueller, A., Juhász, A., Crida, A., Chauvin, G., Andrews, S., Wilner, D., Kraus, A., Dahm, S., Robitaille, T., Jang-Condell, H., Abe, L., Akiyama, E., Brandner, W., Brandt, T., Carson, J., Egner, S., Follette, K. B., Goto, M., Guyon, O., Hayano, Y., Hayashi, M., Hayashi, S., Hodapp, K., Ishii, M.,

Iye, M., Janson, M., Kandori, R., Knapp, G., Kudo, T., Kusakabe, N., Kuzuhara, M., Mayama, S., McElwain, M., Matsuo, T., Miyama, S., Morino, J.-I., Nishimura, T., Pyo, T.-S., Serabyn, G., Suto, H., Suzuki, R., Takami, M., Takato, N., Terada, H., Tomono, D., Turner, E., Watanabe, M., Yamada, T., Takami, H., Usuda, T., and Tamura, M. (2013). Spiral Arms in the Asymmetrically Illuminated Disk of MWC 758 and Constraints on Giant Planets. ApJ, 762:48.

Gundlach, B. and Blum, J. (2015). The Stickiness of Micrometer-sized Water-ice Particles. ApJ, 798:34.

Güttler, C., Blum, J., Zsom, A., Ormel, C. W., and Dullemond, C. P. (2010). The outcome of protoplanetary dust growth: pebbles, boulders, or planetesimals?. I. Mapping the zoo of laboratory collision experiments. A&A, 513:A56.

Haisch, Jr., K. E., Lada, E. A., and Lada, C. J. (2001). Disk Frequencies and Lifetimes in Young Clusters. ApJ, 553:L153–L156.

Hayashi, C. (1981). Structure of the Solar Nebula, Growth and Decay of Magnetic Fields and Effects of Magnetic and Turbulent Viscosities on the Nebula. *Progress of Theoretical Physics Supplement*, 70:35–53.

Heim, L.-O., Blum, J., Preuss, M., and Butt, H.-J. (1999). Adhesion and Friction Forces between Spherical Micrometer-Sized Particles. *Physical Review Letters*, 83:3328–3331.

Hewins, R. H., Connolly, H. C., J., E., L. G., and Libourel, G. (2005). Experimental Constraints on Chondrule Formation. In Krot, A. N., Scott, E. R. D., and Reipurth, B., editors, *Chondrites and the Protoplanetary Disk*, volume 341 of *Astronomical Society of the Pacific Conference Series*, page 286.

Hogerheijde, M. R., Bekkers, D., Pinilla, P., Salinas, V. N., Kama, M., Andrews, S. M., Qi, C., and Wilner, D. J. (2016). Steepening of the 820 μm continuum surface brightness profile signals dust evolution in TW Hydrae's disk. A&A, 586:A99.

Hood, L. L. (1998). Thermal processing of chondrule and CAI precursors in planetesimal bow shocks. *Meteoritics and Planetary Science*, 33.

Hood, L. L. and Horanyi, M. (1991). Gas dynamic heating of chondrule precursor grains in the solar nebula. Icarus, 93:259–269.

Iida, A., Nakamoto, T., Susa, H., and Nakagawa, Y. (2001). A Shock Heating Model for Chondrule Formation in a Protoplanetary Disk. Icarus, 153:430–450.

Isella, A., Carpenter, J. M., and Sargent, A. I. (2009). Structure and Evolution of Pre-main-sequence Circumstellar Disks. ApJ, 701:260–282.

Isella, A., Guidi, G., Testi, L., Liu, S., Li, H., Li, S., Weaver, E., Boehler, Y., Carperter, J. M., De Gregorio-Monsalvo, I., Manara, C. F., Natta, A., Pérez, L. M., Ricci, L., Sargent, A., Tazzari, M., and Turner, N. (2016). Ringed Structures of the HD 163296 Protoplanetary Disk Revealed by ALMA. *Physical Review Letters*, 117(25):251101.

Johansen, A. and Klahr, H. (2005). Dust Diffusion in Protoplanetary Disks by Magnetorotational Turbulence. ApJ, 634:1353–1371.

Johansen, A. and Lacerda, P. (2010). Prograde rotation of protoplanets by accretion of pebbles in a gaseous environment. MNRAS, 404:475–485.

Johansen, A., Oishi, J. S., Mac Low, M.-M., Klahr, H., Henning, T., and Youdin, A. (2007). Rapid planetesimal formation in turbulent circumstellar disks. Nature, 448:1022–1025.

Johansen, A., Youdin, A., and Klahr, H. (2009). Zonal Flows and Long-lived Axisymmetric Pressure Bumps in Magnetorotational Turbulence. ApJ, 697:1269–1289.

Kataoka, A., Tanaka, H., Okuzumi, S., and Wada, K. (2013). Fluffy dust forms icy planetesimals by static compression. A&A, 557:L4.

Kley, W. and Nelson, R. P. (2012). Planet-Disk Interaction and Orbital Evolution. ARA&A, 50:211–249.

Kothe, S., Blum, J., Weidling, R., and Güttler, C. (2013). Free collisions in a microgravity many-particle experiment. III. The collision behavior of sub-millimeter-sized dust aggregates. Icarus, 225:75–85.

Kouchi, A., Yamamoto, T., Kozasa, T., Kuroda, T., and Greenberg, J. M. (1994). Conditions for condensation and preservation of amorphous ice and crystallinity of astrophysical ices. A&A, 290:1009–1018.

Kratter, K. and Lodato, G. (2016). Gravitational Instabilities in Circumstellar Disks. ARA&A, 54:271–311.

Kretke, K. A. and Lin, D. N. C. (2007). Grain Retention and Formation of Planetesimals near the Snow Line in MRI-driven Turbulent Protoplanetary Disks. ApJ, 664:L55–L58.

Kretke, K. A., Lin, D. N. C., and Turner, N. J. (2008). Planet formation around intermediate mass stars. In Sun, Y.-S., Ferraz-Mello, S., and Zhou, J.-L., editors, *IAU Symposium*, volume 249 of *IAU Symposium*, pages 293–300.

Kuchner, M. J. (2004). A Minimum-Mass Extrasolar Nebula. ApJ, 612:1147–1151.

Lada, C. J. (1987). Star formation - From OB associations to protostars. In Peimbert, M. and Jugaku, J., editors, *Star Forming Regions*, volume 115 of *IAU Symposium*, pages 1–17.

Lambrechts, M. and Johansen, A. (2012). Rapid growth of gas-giant cores by pebble accretion. A&A, 544:A32.

Leger, A., Jura, M., and Omont, A. (1985). Desorption from interstellar grains. A&A, 144:147–160.

Levison, H. F., Thommes, E., and Duncan, M. J. (2010). Modeling the Formation of Giant Planet Cores. I. Evaluating Key Processes. AJ, 139:1297–1314.

Lin, D. N. C. and Papaloizou, J. (1986). On the tidal interaction between protoplanets and the protoplanetary disk. III - Orbital migration of protoplanets. ApJ, 309:846–857.

Lynden-Bell, D. and Pringle, J. E. (1974). The evolution of viscous discs and the origin of the nebular variables. MNRAS, 168:603–637.

Mamajek, E. E. (2009). Initial Conditions of Planet Formation: Lifetimes of Primordial Disks. In Usuda, T., Tamura, M., and Ishii, M., editors, *American Institute of Physics Conference Series*, volume 1158 of *American Institute of Physics Conference Series*, pages 3–10.

Marino, S., Perez, S., and Casassus, S. (2015). Shadows Cast by a Warp in the HD 142527 Protoplanetary Disk. ApJ, 798:L44.

Mathis, J. S., Rumpl, W., and Nordsieck, K. H. (1977). The size distribution of interstellar grains. ApJ, 217:425–433.

Mayor, M. and Queloz, D. (1995). A Jupiter-mass companion to a solar-type star. Nature, 378:355–359.

McClure, M. K., Espaillat, C., Calvet, N., Bergin, E., D'Alessio, P., Watson, D. M., Manoj, P., Sargent, B., and Cleeves, L. I. (2015). Detections of Trans-Neptunian Ice in Protoplanetary Disks. ApJ, 799:162.

McMullin, J. P., Waters, B., Schiebel, D., Young, W., and Golap, K. (2007). CASA Architecture and Applications. In Shaw, R. A., Hill, F., and Bell, D. J., editors, *Astronomical Data Analysis Software and Systems XVI*, volume 376 of *Astronomical Society of the Pacific Conference Series*, page 127.

Mihalas, D. and Mihalas, B. W. (1984). *Foundations of radiation hydrodynamics*.

Montesinos, M., Perez, S., Casassus, S., Marino, S., Cuadra, J., and Christiaens, V. (2016). Spiral Waves Triggered by Shadows in Transition Disks. ApJ, 823:L8.

Morbidelli, A., Bottke, W. F., Nesvorný, D., and Levison, H. F. (2009). Asteroids were born big. Icarus, 204:558–573.

Morris, M. A., Boley, A. C., Desch, S. J., and Athanassiadou, T. (2012). Chondrule Formation in Bow Shocks around Eccentric Planetary Embryos. ApJ, 752:27.

Morris, M. A. and Desch, S. J. (2010). Thermal Histories of Chondrules in Solar Nebula Shocks. ApJ, 722:1474–1494.

Musiolik, G., Teiser, J., Jankowski, T., and Wurm, G. (2016a). Collisions of CO_2 Ice Grains in Planet Formation. ApJ, 818:16.

Musiolik, G., Teiser, J., Jankowski, T., and Wurm, G. (2016b). Ice Grain Collisions in Comparison: CO2, H2O, and Their Mixtures. ApJ, 827:63.

Muto, T., Grady, C. A., Hashimoto, J., Fukagawa, M., Hornbeck, J. B., Sitko, M., Russell, R., Werren, C., Curé, M., Currie, T., Ohashi, N., Okamoto, Y., Momose, M., Honda, M., Inutsuka, S., Takeuchi, T., Dong, R., Abe, L., Brandner, W., Brandt, T., Carson, J., Egner, S., Feldt, M., Fukue, T., Goto, M., Guyon, O., Hayano, Y., Hayashi, M., Hayashi, S., Henning, T., Hodapp, K. W., Ishii, M., Iye, M., Janson, M., Kandori, R., Knapp, G. R., Kudo, T., Kusakabe, N., Kuzuhara, M., Matsuo, T., Mayama, S., McElwain, M. W., Miyama, S., Morino, J.-I., Moro-Martin, A., Nishimura, T., Pyo, T.-S., Serabyn, E., Suto, H., Suzuki, R., Takami, M., Takato, N., Terada, H., Thalmann, C., Tomono, D., Turner, E. L., Watanabe, M., Wisniewski, J. P., Yamada, T., Takami, H., Usuda, T., and Tamura, M. (2012). Discovery of Small-scale Spiral Structures in the Disk of SAO 206462 (HD 135344B): Implications for the Physical State of the Disk from Spiral Density Wave Theory. ApJ, 748:L22.

Nakamoto, T. and Nakagawa, Y. (1994). Formation, early evolution, and gravitational stability of protoplanetary disks. ApJ, 421:640–650.

Natta, A., Testi, L., Neri, R., Shepherd, D. S., and Wilner, D. J. (2004). A search for evolved dust in Herbig Ae stars. A&A, 416:179–186.

Natta, A., Testi, L., and Randich, S. (2006). Accretion in the ρ-Ophiuchi pre-main sequence stars. A&A, 452:245–252.

Öberg, K. I., Murray-Clay, R., and Bergin, E. A. (2011). The Effects of Snowlines on C/O in Planetary Atmospheres. ApJ, 743:L16.

Okuzumi, S., Momose, M., Sirono, S.-i., Kobayashi, H., and Tanaka, H. (2016). Sintering-induced Dust Ring Formation in Protoplanetary Disks: Application to the HL Tau Disk. ApJ, 821:82.

Okuzumi, S., Tanaka, H., and Sakagami, M.-a. (2009). Numerical Modeling of the Coagulation and Porosity Evolution of Dust Aggregates. ApJ, 707:1247–1263.

Ormel, C. W. and Cuzzi, J. N. (2007). Closed-form expressions for particle relative velocities induced by turbulence. A&A, 466:413–420.

Ormel, C. W., Paszun, D., Dominik, C., and Tielens, A. G. G. M. (2009). Dust coagulation and fragmentation in molecular clouds. I. How collisions between dust aggregates alter the dust size distribution. A&A, 502:845–869.

Ormel, C. W., Spaans, M., and Tielens, A. G. G. M. (2007). Dust coagulation in protoplanetary disks: porosity matters. A&A, 461:215–232.

Paardekooper, S.-J. (2007). Dust accretion onto high-mass planets. A&A, 462:355–369.

Paardekooper, S.-J. and Mellema, G. (2006). Dust flow in gas disks in the presence of embedded planets. A&A, 453:1129–1140.

Panić, O. and Min, M. (2017). Effects of disc midplane evolution on CO snowline location. MNRAS.

Pavlyuchenkov, Y. and Dullemond, C. P. (2007). Dust crystallinity in protoplanetary disks: the effect of diffusion/viscosity ratio. A&A, 471:833–840.

Pérez, L. M., Carpenter, J. M., Andrews, S. M., Ricci, L., Isella, A., Linz, H., Sargent, A. I., Wilner, D. J., Henning, T., Deller, A. T., Chandler, C. J., Dullemond, C. P., Lazio, J., Menten, K. M., Corder, S. A., Storm, S., Testi, L., Tazzari, M., Kwon, W., Calvet, N., Greaves, J. S., Harris, R. J., and Mundy, L. G. (2016). Spiral density waves in a young protoplanetary disk. *Science*, 353:1519–1521.

Pfalzner, S. (2003). Spiral Arms in Accretion Disk Encounters. ApJ, 592:986–1001.

Pfalzner, S. and Kaczmarek, T. (2013). The expansion of massive young star clusters - observation meets theory. A&A, 559:A38.

Pfalzner, S., Steinhausen, M., and Menten, K. (2014). Short Dissipation Times of Protoplanetary Disks: An Artifact of Selection Effects? ApJ, 793:L34.

Pinilla, P., Birnstiel, T., Ricci, L., Dullemond, C. P., Uribe, A. L., Testi, L., and Natta, A. (2012). Trapping dust particles in the outer regions of protoplanetary disks. A&A, 538:A114.

Pinilla, P., Flock, M., Ovelar, M. d. J., and Birnstiel, T. (2016). Can dead zones create structures like a transition disk? A&A, 596:A81.

Piso, A.-M. A., Öberg, K. I., Birnstiel, T., and Murray-Clay, R. A. (2015). C/O and Snowline Locations in Protoplanetary Disks: The Effect of Radial Drift and Viscous Gas Accretion. ApJ, 815:109.

Pollack, J. B., Hubickyj, O., Bodenheimer, P., Lissauer, J. J., Podolak, M., and Greenzweig, Y. (1996). Formation of the Giant Planets by Concurrent Accretion of Solids and Gas. Icarus, 124:62–85.

Poppe, T., Blum, J., and Henning, T. (2000). Analogous Experiments on the Stickiness of Micron-sized Preplanetary Dust. ApJ, 533:454–471.

Qi, C., Öberg, K. I., Andrews, S. M., Wilner, D. J., Bergin, E. A., Hughes, A. M., Hogherheijde, M., and D'Alessio, P. (2015). Chemical Imaging of the CO Snow Line in the HD 163296 Disk. ApJ, 813:128.

Ros, K. and Johansen, A. (2013). Ice condensation as a planet formation mechanism. A&A, 552:A137.

Rosotti, G. P., Ercolano, B., Owen, J. E., and Armitage, P. J. (2013). The interplay between X-ray photoevaporation and planet formation. MNRAS, 430:1392–1401.

Schräpler, R., Blum, J., Seizinger, A., and Kley, W. (2012). The Physics of Protoplanetesimal Dust Agglomerates. VII. The Low-velocity Collision Behavior of Large Dust Agglomerates. ApJ, 758:35.

Schräpler, R. and Henning, T. (2004). Dust Diffusion, Sedimentation, and Gravitational Instabilities in Protoplanetary Disks. ApJ, 614:960–978.

Semenov, D., Henning, T., Helling, C., Ilgner, M., and Sedlmayr, E. (2003). Rosseland and Planck mean opacities for protoplanetary discs. A&A, 410:611–621.

Shakura, N. I. and Sunyaev, R. A. (1973). Black holes in binary systems. Observational appearance. A&A, 24:337–355.

Sirono, S.-i. (2011a). Planetesimal Formation Induced by Sintering. ApJ, 733:L41.

Sirono, S.-i. (2011b). The Sintering Region of Icy Dust Aggregates in a Protoplanetary Nebula. ApJ, 735:131.

Smoluchowski, M. V. (1916). Drei Vortrage uber Diffusion, Brownsche Bewegung und Koagulation von Kolloidteilchen. *Zeitschrift fur Physik*, 17:557–585.

Stammler, S. M., Birnstiel, T., Panić, O., Dullemond, C. P., and Dominik, C. (2017). Redistribution of CO at the Location of the CO Ice Line in evolving Gas and Dust Disks. *ArXiv e-prints*.

Stammler, S. M. and Dullemond, C. P. (2014). A critical analysis of shock models for chondrule formation. Icarus, 242:1–10.

Stevenson, D. J. and Lunine, J. I. (1988). Rapid formation of Jupiter by diffuse redistribution of water vapor in the solar nebula. Icarus, 75:146–155.

Stolker, T., Dominik, C., Avenhaus, H., Min, M., de Boer, J., Ginski, C., Schmid, H. M., Juhasz, A., Bazzon, A., Waters, L. B. F. M., Garufi, A., Augereau, J.-C., Benisty, M., Boccaletti, A., Henning, T., Langlois, M., Maire, A.-L., Ménard, F., Meyer, M. R., Pinte, C., Quanz, S. P., Thalmann, C., Beuzit, J.-L., Carbillet, M., Costille, A., Dohlen, K., Feldt, M., Gisler, D., Mouillet, D., Pavlov, A., Perret, D., Petit, C., Pragt, J., Rochat, S., Roelfsema, R., Salasnich, B., Soenke, C., and Wildi, F. (2016). Shadows cast on the transition disk of HD 135344B. Multiwavelength VLT/SPHERE polarimetric differential imaging. A&A, 595:A113.

Tegler, S. C. and Romanishin, W. (1998). Two distinct populations of Kuiper-belt objects. Nature, 392:49.

Tomida, K., Machida, M. N., Hosokawa, T., Sakurai, Y., and Lin, C. H. (2017). Grand-design Spiral Arms in a Young Forming Circumstellar Disk. ApJ, 835:L11.

Tsiganis, K., Gomes, R., Morbidelli, A., and Levison, H. F. (2005). Origin of the orbital architecture of the giant planets of the Solar System. Nature, 435:459–461.

Tsukagoshi, T., Nomura, H., Muto, T., Kawabe, R., Ishimoto, D., Kanagawa, K. D., Okuzumi, S., Ida, S., Walsh, C., and Millar, T. J. (2016). A Gap with a Deficit of Large Grains in the Protoplanetary Disk around TW Hya. ApJ, 829:L35.

van der Marel, N., Cazzoletti, P., Pinilla, P., and Garufi, A. (2016). Vortices and Spirals in the HD135344B Transition Disk. ApJ, 832:178.

Villeneuve, J., Chaussidon, M., and Libourel, G. (2009). Homogeneous Distribution of ^{26}Al in the Solar System from the Mg Isotopic Composition of Chondrules. *Science*, 325:985.

Wada, K., Tanaka, H., Suyama, T., Kimura, H., and Yamamoto, T. (2009). Collisional Growth Conditions for Dust Aggregates. ApJ, 702:1490–1501.

Wagner, K., Apai, D., Kasper, M., and Robberto, M. (2015). Discovery of a Two-armed Spiral Structure in the Gapped Disk around Herbig Ae Star HD 100453. ApJ, 813:L2.

Weidenschilling, S. J. (1977a). Aerodynamics of solid bodies in the solar nebula. MNRAS, 180:57–70.

Weidenschilling, S. J. (1977b). The distribution of mass in the planetary system and solar nebula. Ap&SS, 51:153–158.

Weinberger, A. J., Anglada-Escudé, G., and Boss, A. P. (2013). Distance and Kinematics of the TW Hydrae Association from Parallaxes. ApJ, 762:118.

Whipple, F. L. (1972). On certain aerodynamic processes for asteroids and comets. In Elvius, A., editor, *From Plasma to Planet*, page 211.

Windmark, F., Birnstiel, T., Güttler, C., Blum, J., Dullemond, C. P., and Henning, T. (2012a). Planetesimal formation by sweep-up: how the bouncing barrier can be beneficial to growth. A&A, 540:A73.

Windmark, F., Birnstiel, T., Ormel, C. W., and Dullemond, C. P. (2012b). Breaking through: The effects of a velocity distribution on barriers to dust growth. A&A, 544:L16.

Woitke, P. and Helling, C. (2003). Dust in brown dwarfs. II. The coupled problem of dust formation and sedimentation. A&A, 399:297–313.

Yamamoto, T., Nakagawa, N., and Fukui, Y. (1983). The chemical composition and thermal history of the ice of a cometary nucleus. A&A, 122:171–176.

Youdin, A. N. and Goodman, J. (2005). Streaming Instabilities in Protoplanetary Disks. ApJ, 620:459–469.

Youdin, A. N. and Lithwick, Y. (2007). Particle stirring in turbulent gas disks: Including orbital oscillations. Icarus, 192:588–604.

Youdin, A. N. and Shu, F. H. (2002). Planetesimal Formation by Gravitational Instability. ApJ, 580:494–505.

Yu, Y., Hewins, H. H., and Zanda, B. (1996). Sodium und Sulfur in Chondrules: Heating Time and Cooling Curves. In Hewins, R. H., Jones, R. H., and Scott, E. R. D., editors, *Chondrules and the Protoplanetary Disk*, pages 257–263.

Zhang, K., Blake, G. A., and Bergin, E. A. (2015). Evidence of Fast Pebble Growth Near Condensation Fronts in the HL Tau Protoplanetary Disk. ApJ, 806:L7.

Zhu, Z., Stone, J. M., and Rafikov, R. R. (2013). Low-mass Planets in Protoplanetary Disks with Net Vertical Magnetic Fields: The Planetary Wake and Gap Opening. ApJ, 768:143.

Zhu, Z., Stone, J. M., Rafikov, R. R., and Bai, X.-n. (2014). Particle Concentration at Planet-induced Gap Edges and Vortices. I. Inviscid Three-dimensional Hydro Disks. ApJ, 785:122.

Zsom, A. and Dullemond, C. P. (2008). A representative particle approach to coagulation and fragmentation of dust aggregates and fluid droplets. A&A, 489:931–941.

Zsom, A., Sándor, Z., and Dullemond, C. P. (2011). The first stages of planet formation in binary systems: how far can dust coagulation proceed? A&A, 527:A10.

Acknowledgments

First and foremost I would like to thank my advisor, Kees Dullemond, for giving me the opportunity for carrying out this thesis in his group, for the lively discussions, and for giving me valuable hints whenever they were needed.

I also would like to thank my second adviser, Jorge Cuadra, for accepting me in his group in Santiago de Chile, where I spent one year. It was a very nice experience, especially because it widened my astronomical horizon.

I want to thank Til Birnstiel for his close collaboration, for explaining every detail of dust coagulation and its software implementation to me, for showing me numerical tricks I've never heard of before, and especially for the guided city tour through Boston and Cambridge in the deepest winter together with his wive.

Furthermore, I want to thank Nicolas Cuello and Matías Montesinos for the fruitful collaboration where we combined several astronomical software packages into one versatile project, that will result in numerous publications. It was (and still is) fun to work with you! And I also want to thank you especially for organizing several *asados*, where you introduced me to the delicious Chilean "peanuts".

I want to thank my parents, who supported me through the years and made it possible for me to study physics without having to think of finances.

A special thanks goes out to María Jiménez, who translated the abstract of this thesis into Spanish, to Eric Pellegrini, and to Daniel "Hong" Harsono; the greatest pub quiz team this Earth has ever seen!

I also would like to thank Teresa Müller for several phsychological therapy sessions!

I want to thank the Heidelberg coffee team Joanna Drążkowska, László Szűcs (I found all the characters! Yay!), Jon Ramsey, Mei Sasaki, Volker Gaibler, and Christian Baczynski, as well as the Santiago coffee team Don Gergely Hajdu, Francisco Aros, Rodrigo Carvajal, and Diego Calderón, who all helped me to escape the institute in the afternoons!

And last but not least, I want to thank all the people that crossed my path in the past years, especially, Thomas Beisitzer, Adriana Pohl, Akimasa Kataoka, Jennifer Schober, Tobias Schmidt, Helen Morrison, and Carsten Littek!

micdrop